UiT The Arctic University of Norway

Department of Technology and Safety

MarSpray LiDAR (MSL) for the comprehensive measurement of Sea Spray for Improving the Prediction of Marine Icing in Cold Conditions

Sushmit Dhar

Master's thesis in Technology and Safety in the High North - TEK-3901 - June 2021

Preface

This Master's thesis is submitted as a fulfilment of my master's degree in Technology and Safety in the High North at UiT – The Arctic University of Norway, Tromsø. The work in this thesis was carried out at the Department of Technology and Safety in the spring semester of 2021. It is the original and independent work of the author except where acknowledged explicitly in the text. Part of the thesis was conducted through pre-projects and published in a journal and presented at a conference. This Master's thesis contains 16400 words, 48 Figures and 2 tables.

Acknowledgements

"If I have seen further, it is by standing upon the shoulders of giants"- Sir Isaac Newton, which is the very emotion I had on completion of my thesis. Indeed, my supervisors are giants who led me to perceive more than I could and continually guided and supported me towards this attainment.

I would like to express my appreciation and deepest gratitude to my principal supervisor Associate Professor, Kåre Edvardsen. And thank him for always keeping his door open for me, supervising me with his vast knowledge and for being so passionate and enthusiastic in every step throughout this course. His expertise and extensive experience aided to foresee challenges, which subsequently helped to finish the thesis on time.

My reverence and warmest regards to Associate Professor, Hassan Abbas Khawaja, firstly I would like to thank him for believing in a stranger who kept knocking his office door and giving him an opportunity and being patient while assisting and reassuring him for climbing every step. I would like to appreciate his prompt responses and availability during this period to clarify my concepts, inspiring and supervising journal publications, provide guidance and scientific exchange of ideas, even while he was on the other side of the planet. I also, recognize his initiative and drive to teach an excellent subject like "Multiphysics Simulation", which changed my approach to this master program.

And definitely my gratefulness to Professor Javad Barabady, who has been a constant source of knowledge, profound support and inspiration not just during my thesis but also throughout the whole master program.

I am incredibly grateful to Daniel Henry Hansen and Ståle Antonsen, who have given sincere efforts and helped me in crucial steps in developing the equipment.

Words are very few to express my honor for my affectionate parents, who always had confidence in me and was determined to provide me with the best education they could since my childhood. Also, I am very grateful to have shared office with Gøran Kristiansen, during which we helped each other remain motivated and be resilient during this pandemic situation.

Sushmit Dhar

Abstract

Marine icing phenomenon depends on multiple variables like vessel characteristics and uncertain factors like environmental parameters. Developing an accurate model for its forecasting, evaluation, and estimation is very challenging. Commonly, the most severe ice accretion is caused by sea spray. The past attempts to measure impinging sea spray flux were carried out on specific parts of the spray cloud, and most of the empirical spray-flux expressions presented only work in specific conditions. This necessitates further real-time and accurate field measurements of the entire impinging spray flux carried out in multiple scenarios in order to develop more practical correlations. The high temporal and spatial resolution measurement and scanning ability of the LiDAR technique have proven to be useful in the agricultural domain for studying pesticide spray drift. The first part of my thesis reviews the past studies carried out using the LiDAR technique to measure the evolution of the pesticide spray cloud, asserting the potential of using a shipborne LiDAR to analyze sea spray in the study of marine icing phenomenon. The LiDAR system is capable of visualizing the evolution of the sea spray drift with a high spatial and temporal resolution, which can enable comprehensive real-time measurement of spray flux for the entire sea spray cloud.

In order to recognize this potential, in the next part of the thesis, a novel LiDAR prototype named MarSpray LiDAR (which will be referred to as MSL henceforth) is designed, built, and tested. The MSL is a mono-static multi-axial 905nm wavelength LiDAR equipment specifically designed for short-range spray analysis and measurement. It generates laser pulses of short width (FWHM) of 3 to 4ns, with a spatial resolution able to highlight local variation concentrations on the order of 45 to 60cm inside the spray with a high temporal resolution of 1ms. With certain future modifications of the MSL, the primary application for this remote sensing equipment can be made suitable for shipborne use to profile and retrieve marine spray properties capable of gathering real-time data and has the potential to bridge the gap that the past techniques failed to measure. These measurement data can be applied for developing a model based on comprehensive data for improving marine icing prediction in cold conditions.

Abbreviations

ADC	Analog to digital converter
APD	Avalanche photodiode
BRDF	Bidirectional reflectance distribution function
DAQ	Data Acquisition System
DIAL	Differential Absorption LiDAR
FOV	Field of view
FWHM	Full width half maximum
GaN FET	Gallium Nitride field-effect transistor
IMU	Inertial measurement unit
InGaAs	Indium gallium arsenide
LASER	Light Amplification by Stimulated Emission of Radiation
LiDAR	Light detection and ranging
LWC	Liquid water content
MSL	MarSpray LiDAR (Marine Spray LiDAR)
PMT	Photomultiplier Tube
SNR	Signal to Noise Ratio
SRT	Surface reference target
TOF	Time of Flight

Nomenclature

$\sum F_{ine}$	Inelastic component of the backscattered signal
$\alpha_A(r)$	Absorption coefficient
$\alpha(r)$	Range-dependent extinction coefficient function
$\beta(r)$	Range-dependent backscatter coefficient function
$\beta'(r)$	Attenuated backscatter
$\beta_T(r)$	Total elastic scattering coefficient
η	System efficiency of the elastic LiDAR
τ	Duration of the laser Pulse
τ_L	Emitted pulse duration
τ_N	Time constant of the detecting electronics
τ_w	Reaction time of the of laser pulse with the scatterer
A_o	Receiver aperture area
B_{ice}	Centre of Buoyancy (ice accretion)
B_o	Centre of Buoyancy (No ice accretion)
$B\varphi$	Centre of Buoyancy (after heel)
E_{det}	Energy gathered by the LiDAR photodetector
E_o	Transmitted laser pulsed energy
E_{prm}	Energy arriving on the telescope's primary lens or mirror
F_{bsc}	Received backscattered signal
F_{e_mul}	Elastic multiple scattered radiant flux
F_{e_sin}	Elastic single scattered radiant flux
F_{in}	Incoming radiant flux
F_{out}	Outgoing radiant flux
G_o	Centre of Gravity (No ice accretion)
GZ	Righting Lever
K	Ship's Keel
K_s	Elastic LiDAR system constant
M_{ice}	Metacenter (ice accretion)
M_o	Metacenter (No ice accretion)
$M\varphi$	Actual Metacenter when heel
$N\varphi$	False Metacenter
O(r)	Range-dependent overlap function
ϕ	Angle of heel
P_o	Transmitted laser pulsed power
T(H)	Transmittance of a layer of thickness H
U(r)	Attenuated backscattering function
Q_c	Convective or sensible heat flux from the air
Q_e	Evaporative or latent heat flux from the air
Q_f	Latent heat released during freezing
Q_d	Heating or cooling from impinging spray
Q_r	Heating or cooling from radiation

List of Publications

Journal Publication

Dhar, S., & Khawaja, H. A. (2021). Recognizing potential of LiDAR for comprehensive measurement of sea spray flux for improving the prediction of marine icing in cold conditions—A review. Ocean Engineering, 223, 108668. https://doi.org/10.1016/j.oceaneng.2021.108668

Conference Presentation

Dhar, S., Edvardsen, K., & Khawaja, H. (2020, October 12). Estimation of Sea Spray Flux for Improving the Prediction of Marine Icing in Cold Conditions using LiDAR. MULTIPHYSICS 2020. The International Society of Multiphysics, Virtual. https://app.cristin.no/results/show.jsf?id=1860329

Video Presentation Link:
https://drive.google.com/drive/folders/1HPldiuPleLijM2lsIPl4wFftzKG8qaGM

Contents

List of Tables

List of Figures

1 Introduction

1.1 Background and Motivation

Earlier industries have not shown much interest in the colder regions of our planet due to their focus on exploiting resources in easily accessible warmer regions. However, with the increase in competition in warmer regions, and the promising presence of natural resources, shorter transport distances and tourism opportunities, interest has grown to exploit these opportunities in marine cold climate regions. Shipping plays an integral part to utilize these opportunities as they are the preferred means for transportation, carrying out surveying operations, and also used as base stations. The growth of interest is evident from the significant surge in maritime traffic in the last few years. The total distance sailed by ships in the Arctic Polar Code area grew by 75% in 2019 compared to 2013 and predicted to increase substantially in the coming years (PAME, 2020).

Nevertheless, colder regions bring their challenges due to its remoteness and harsh weather. Icing is regarded as the most significant risk associated with colder regions; multiple vessels became disabled or sank after ice accretion leading to loss of life, damaging environment and property (Aksyutin, 1979; DeAngelis, 1974; Guest and Luke, 2005; Hay, 1956; Lundqvist and Udin, 1977; NTSB, 2018; Ryerson, 2013; Shekhtman, 1968; Shellard, 1974). Even after many years of research, advancement in analytical and numerical models, marine icing still possesses a serious operational hazard for ships operating in cold climate regions (Cammaert, 2013). Hence it is crucial prior to entering these regions to winterize a vessel effectively, which incorporates structural designs and techniques by adequate anti or de-icing, insulation and drainage system to decrease the adverse effects of icing and exposure to cold temperature (DNVGL, 2019). Past analysis of icing observations on ships depending on the geographical location indicated typically sea spray alone contributed 50–97%, spray along with atmospheric icing 1.4 - 41% and atmospheric icing alone 1 - 4% towards accumulation of marine icing over the vessels (Aksyutin, 1979; Brown and Roebber, 1985; Kato, 2012; Makkonen, 1984; Panov, 1976; Shekhtman, 1968; Shellard, 1974; Zakrzewski, 1987). Sea spray ice accretion possess a substantial hazard to a vessel's seaworthiness as navigation, communication, safety, and other essential or critical equipment may become impaired, deck operation severely impacted and evacuation routes obstructed (Makkonen, 1984; Ryerson, 2013). The most imminent danger

associated due to ice accretion for a vessel is the loss of stability which may ultimately lead to capsizing (Guest and Luke, 2005).

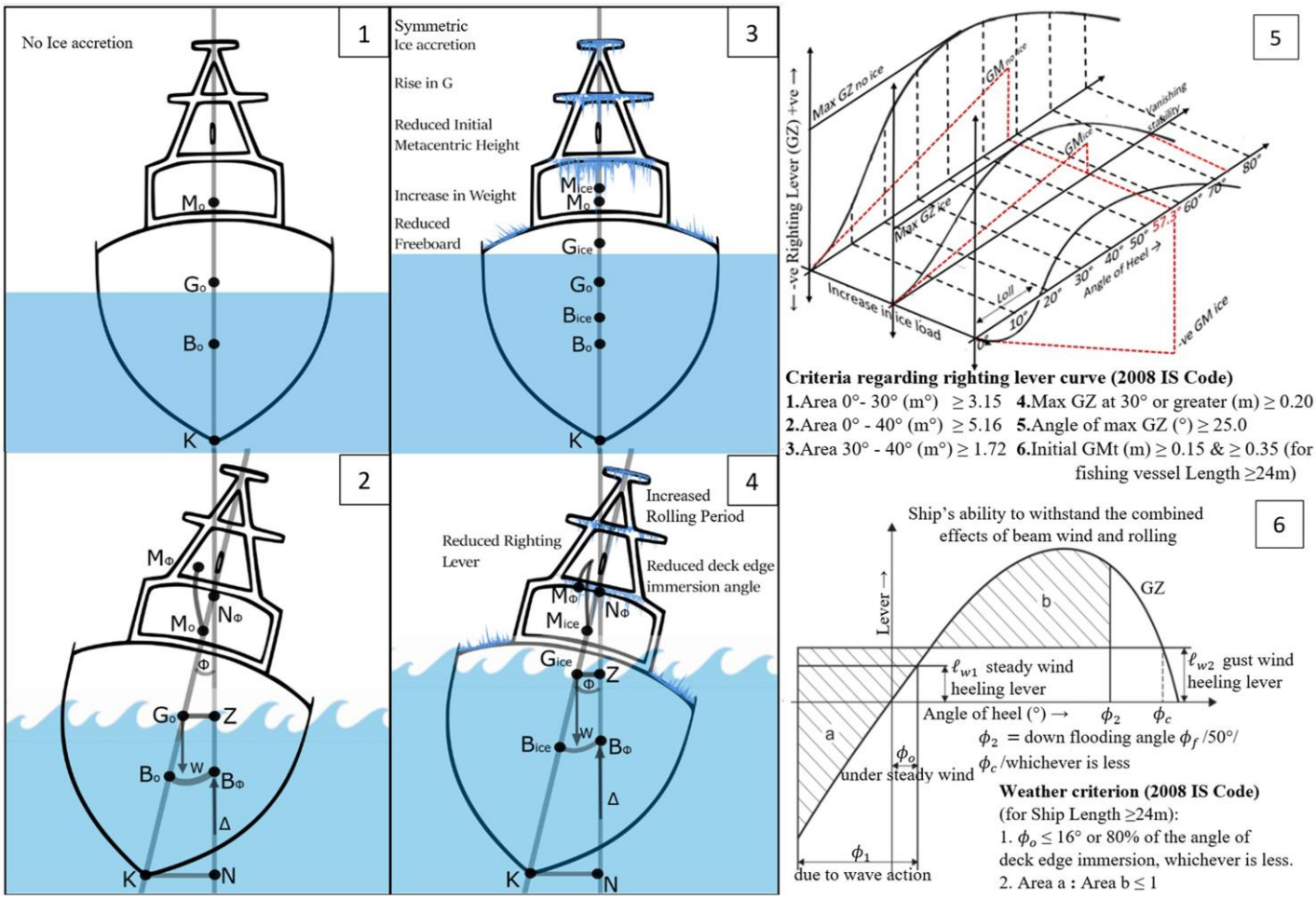

Fig. 1. Vessel with no ice accretion in calm weather (1) Vessel able to upright instantly when heeled (2) Vessel with reduced stability due to ice accretion (3) Vessel's righting ability reduced when heeled (4) Righting Lever curve of a vessel getting unstable with the gradual increase in ice load (5) 2008 IS Code- Severe wind and rolling criterion (6)

Abbreviations: G_o- Centre of Gravity (No ice accretion), M_o- Metacenter (No ice accretion), B_o- Centre of Buoyancy (No ice accretion), K - Keel, ϕ - Angle of heel, Bφ- Centre of Buoyancy (after heel), Nφ- False Metacenter, Mφ - Actual Metacenter when heel, GZ - Righting Lever, B_{ice}- Centre of Buoyancy (ice accretion), M_{ice}- Metacenter (ice accretion). (Picture from paper 1)

The loss of stability is primarily threatening for smaller ships like fishing vessels (Orimolade et al., 2017), and almost 41% of ships entering the Arctic Polar Code area are fishing vessels (PAME, 2020). Fishing vessels relatively have a lower freeboard and have a higher pitch angle

and frequency; hence spray generation is more frequent and likely to cover the whole ship. The superstructure surface area is also large compared to its displacement, making them more exposed to sea spray. In the presence of low temperature, the spray freezes across the vessel and a comparatively lesser weight of accreted ice can destabilize and capsize the fishing vessel (Guest and Luke, 2005). When the vessel is propelling against the wind and waves, maximum ice accretion is on the forepart consequently trimming the vessel by head further intensifying incoming spray and green seas. Symmetric ice accretion (transverse) on the deck (Fig. 1), accommodation tops, and other higher parts shift the center of gravity(G) upward and forward (Trim by head) along the center line which reduces the metacentric height (GMt). This affects the dynamic performance by weakening righting lever (GZ) the ship's ability to upright when heeled by external forces, which is readily evident from the increase in the natural rolling period (also increase in heave and pitch period in a lesser extent) (Wold, 2014). Also, the Deck Edge Immersion angle is reduced due to reduced freeboard (extra weight of the ice), causing water ingression at a smaller angle of heel than initial. The vanishing angle of stability is reduced, which is an indicator of the overall range of stability (Chung, 1995). Due to ice accretion, the wind drag and sail area of the vessel increases, leading to an increase in the wind-induced heeling moment. Gradually with the increase in ice load, the metacentric height keeps decreasing to negative and eventually unable to upright leading to its capsizing. Depending on the relative direction of wind and waves, an asymmetrical sea spray ice accretion can cause the center of gravity to shift upward and away from the center line causing the vessel to list, further increasing its tendency to capsize (Chung, 1995). The International Code on Intact Stability (2008 IS Code) (IMO, 2020) and the Polar Code (IMO, 2016) includes allowance for ice accretion (“30 kg/ on exposed weather decks and gangways and 7.5 kg/ for the projected lateral area of each side of the ship above the water plane”), which should be incorporated in the stability calculation for ships at risk of icing, ensuring its adequate stability.

1.2 Problem Domain and Purpose

The initial research carried out in my thesis (Section 2.1) revealed the inadequacy in the present analytical and numerical icing models for predicting and estimating marine icing, showing the need for accurate real-time measurement of impinging sea spray, as the past researchers were only able to measure parts of a spray cloud and approximations were made based on the localized measured data. There is also a lack of empirical observations; consequently, the

analytical and numerical formulations are based only on a few actual field observations and not comprehensive data. The past sea spray measurement techniques and data collection procedures have proven helpful but failed to provide a factual complete time-resolved distribution data set for building an accurate icing model. Therefore, there is a need for a different setup or a measuring technique that can comprehensively measure the entire spray cloud in the marine environment.

Our research aimed to find and apply an efficient measurement technique that can bridge this gap and provide comprehensive data that can lead to the development of a reliable icing model. The LiDAR (Light detection and ranging) technique has proven to be useful in the agricultural domain for studying pesticide spray drift because of its measurement ability with high temporal and spatial resolution and scanning ability. This showed the potential of using this technique in the field of marine icing for studying sea spray.

1.3 Objective of Research Study

My research is structured in two parts:

1. Reviewing past spray measurements, identifying gaps, and suggesting LiDAR as a solution

Detailing the complexity of the sea spray icing phenomenon and highlighting the importance of real-time sea spray data for a comprehensive marine icing model. Further reviewing the past efforts by researchers to gather sea spray measurements data and pointing the crucial aspects they had failed to provide. Then, presenting the studies where the LiDAR technology is utilized to measure 2D/3D particles fluxes in the agricultural domain for spray drift measurements and affirming its potential to fill the gap that past shipborne measurements failed. Ultimately, proposing the LiDAR as a potential technology solution for the comprehensive measurement of sea spray flux for improving the prediction of marine icing in cold conditions.

2. Designing and building MarSpray LiDAR (MSL) and initial analysis

To carry out subsequent research to design and develop a shipborne LiDAR, the "MarSpray LiDAR (MSL)" intended for measuring and retrieve marine spray properties. Carry out initial measurements using the "MarSpray LiDAR" as a proof of concept showing its potential to gather real-time sea spray measurement data with high temporal and spatial resolution.

1.4 Thesis Structure

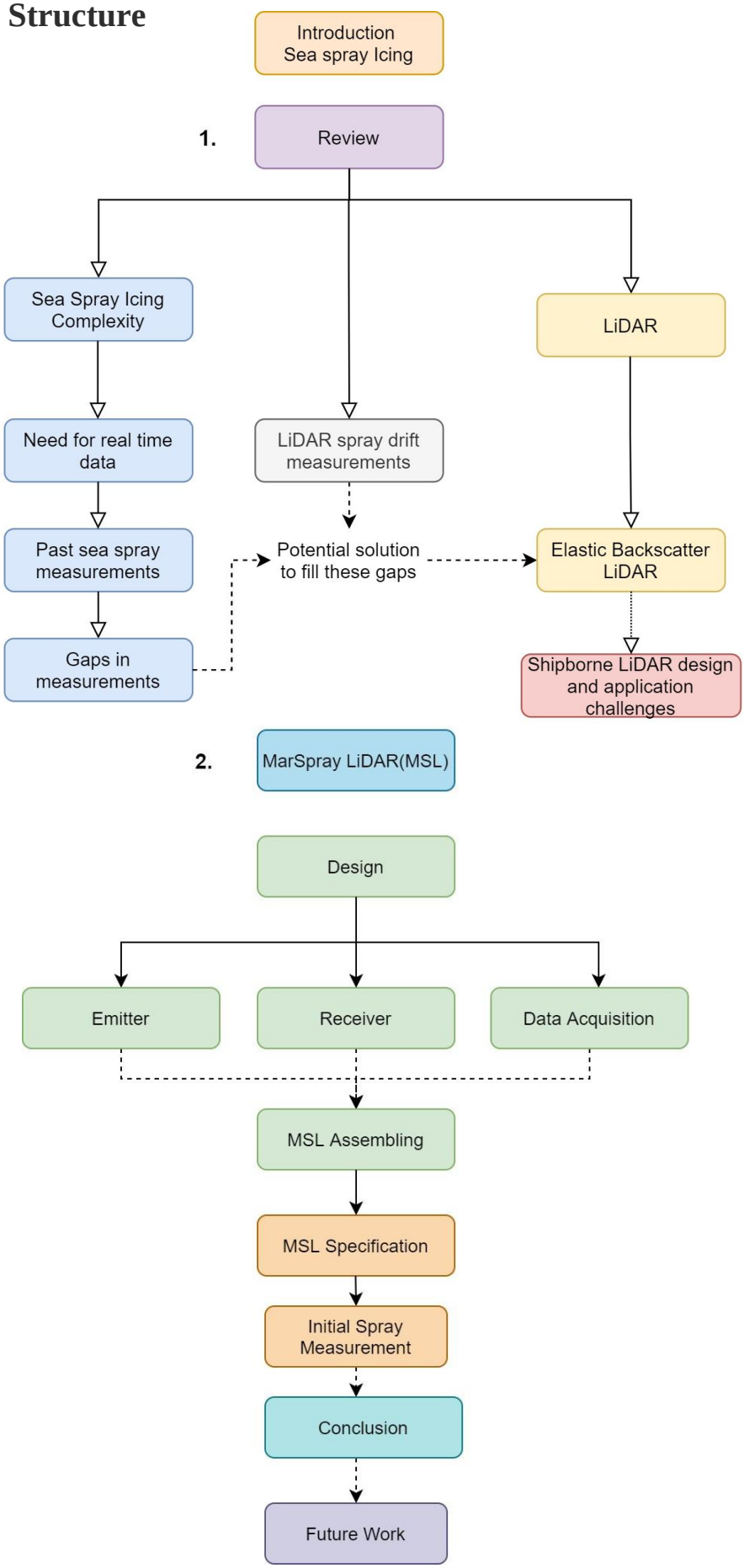

2 Literature Review

2.1 Sea spray Icing

Typically, sea spray ice accretion can be divided into three parts:

1. Sea spray cloud generation

The high energy impact of wave and ship results in the formation of water sheet along its hull, as the water sheet upsurges above the water level, air enters and the sheet break into drops, and gradually forms a cloud of droplets (Dehghani et al., 2016a). These generated droplets reach variable heights and velocities depending on the kinetic energy of the collision and diameters ranging from 10 μm to 3 mm close to the bow (Bodaghkhani et al., 2016; Rashid et al., 2016; Ryerson, 2013; Zakrzewski, 1986). The wave generated spray is a significant source of water flux which is the main contributor for marine ice accretion and often formed close to the vessel's bow depending on relative motion and likely have a short and periodical frequency (Hansen, 2012). Sea spray may also be generated by strong wind shearing droplets off wave crest and by bubbles bursting in breaking waves creating atomized droplets ranging ≤1 μm to ≥25 μm (Fuentes et al., 2010). Wind-generated droplets usually have a relatively much lesser but continuous contribution to the icing phenomena (Dehghani-Sanij et al., 2015).

2. Sea spray cloud drift and impinging upon the ship's structure

The sea spray cloud generated is then carried by the airflow across the vessel until finally impacting components or structures on the vessel. The droplets in the cloud of different initial velocities, sizes and shapes are influenced differently by wind and gravitational force, and their paths and trajectories are specified through drag force, body forces and added mass force acting on it (Dehghani et al., 2016a; Kulyakhtin and Tsarau, 2014; Makkonen, 2000). Most of the small droplets are immediately affected by the wind, and their velocities nearly become similar to that of the wind, but the large droplets being affected more by the gravitational force shortly drops on the deck or back to the sea. The larger and smaller droplets are not able to reach the

highest elevation of the spray, while the trajectory of the medium-sized droplets makes it there (Dehghani et al., 2016b). The characteristics of the spray droplets may change anytime along their path, they may reduce in size due to evaporation or aerodynamic breakup or increase in size when combining with another droplet (Lozowski et al., 2000). LWC (Liquid water content) which is the total mass of the water droplets in a unit volume of dry air, is an important parameter of incoming spray flux along with velocity and distribution of the droplets for icing calculation (Dehghani-Sanij et al., 2017a).

The heat transfer, vaporization and temperature change during the drift of the droplets are determined by the characteristics of the droplet like velocity and size (Dehghani-Sanij et al., 2017a, 2017b; Kulyakhtin and Tsarau, 2014; Sultana et al., 2018). The droplets undergo convective, evaporative and radiative heat transfer, cooling the droplets within the airflow during the drift and eventually supercooled. When the supercooled droplets impact and splash on the substrate, ice is created followed by running off brine water due to gravity and tensile stresses from the air and forms a layer or film, and at the same time losing heat via conduction, convection, and radiation (Kulyakhtin and Tsarau, 2014; Ryerson, 2013). The state of freezing droplets is reliant on properties like its size, salt content and also the thermal behavior of the substrate (Saha et al., 2016).

3. Wet growth of ice from the brine water film

The majority of the brine water film drains off from the ice surface entrapping a small amount leading to the growth of ice or Wet growth (Makkonen, 1987). The rate at which the brine film freezes and the consequent wet growth, is dependent on the incoming water flux transported at different areas on the vessel, and the rates at which latent and sensible heat extracted from these areas (Ryerson, 1995). The sea salt precipitates with growth in ice thickness forming pure ice and pockets of brine (Rashid et al., 2016). The primary heat fluxes at the air-water interface contributing to the freezing of sea spray impinging at the accreted ice surface are - convective or sensible heat flux from the air(Qc), evaporative or latent heat flux from the air(Qe), heating or cooling from impinging spray(Qd) and heating or cooling from radiation(Qr) (Kulyakhtin and Tsarau, 2014; Samuelsen et al., 2017).

Latent heat released during freezing $Q_f = Q_c + Q_e + Q_d + Q_r$ equation 1

2.1.1 Need for real-time data

We had discussed how the spray cloud generated from wave and wind spray is the primary cause of icing on the vessel. Dehghani et al., 2016b describes the process of spray cloud generation, and its movement into several sub-stages including wave impact, water sheet breakup, droplet breakup, spray cloud generation, its acceleration and deceleration and spray cloud fall and finally impingement. However, the physical behaviors of these stages are still inadequately understood. The characteristics of spray clouds such as its duration and movement in the airflow determining incoming water flux are essential aspects to the modeling of the marine icing phenomenon (Kulyakhtin and Tsarau, 2014). The accurate prediction of marine icing and the quantity of ice accretion on the vessel structure is challenging mainly because of the variable quantity of incoming flux at different parts of the vessel which is affected by multiple parameters (Fig. 2) at the same time. Past studies (Dehghani-Sanij et al., 2015; Horjen, 2015, 2013; Kulyakhtin and Tsarau, 2014; Lozowski et al., 2000; Shipilova et al., 2012) did not consider the distribution and variation of droplet size and velocity in a spray cloud for their icing models (Dehghani et al., 2016b). The empirical models and nomograms for predicting icing severity (Comiskey et al., 1984; Itagaki, 1977; Kachurin et al., 1974; Makkonen, 1984; Mertins, 1968; Overland et al., 1986; Overland, 1990; Stallabrass, 1980; Sawada, 1962; Wise and Comiskey, 1980) were mostly built on data obtained from small to medium sized vessels, and based on input parameters of atmospheric conditions, which makes their applications confined to particular regions (Sultana et al., 2018). Also, by investigating analytical models, it was affirmed that further research and precise measurements are needed for determining the thermo-physical properties and heat transfer phenomena (Sultana et al., 2018). The efficiency of the predicted icing rates even from the present advanced models of sea-spray icing even with increased accuracy of the numerical prediction models, depends on the correctness to which the complex and uncertain quantities like spray flux, turbulent heat transfer, and the freezing temperature are predicted (Samuelsen and Graversen,2019).

Table 1 LWC empirical correlations based on different conditions of spray cloud generation(Rashid et al., 2016).

Reference	**LWC correlation**	**Correlation variables**
Borisenkov et al.(1975); Samuelsen et al.(2015); Zakrzewski(1987)	$w = w_o H_s V_r^2 e^{-0.55h}$	w is LWC of spray cloud (kg/m^3)
Borisenkov et al.(1975); Roebber & Mitten (1987)	$w = w_o' H_s^{2.5} e^{-0.55h}$	w' is averaged LWC of spray cloud (kg/m^3)
Forest et al.(2005)	$w = 1.35 H_s^2 2e^{-0.53z'}$	H_s is significant wave height (m)
Stallabrass (1980)	$w' = 1.7\times10^{-4} H_s$	z is spray cloud elevation above mean sea level (m)
Kachurin et al. (1974)	$w' = 10^{-3} H_s$	h is elevation above the vessel deck (m)
Horjen & Vefsnmo (1984)	$w = 0.1 H_s e^{(Hs-2z)}$	H_{rms} root mean square wave height (m)
Brown & Roebber (1985); Forest et al. (2005)	$w = 4.6e^{-(2z/Hrms)2}$	z' is spray cloud elevation above wave wash zone (m) v_r is ship speed relative to incoming wave (m/s) $w_o = 6.36\times10^{-5}$ (empirical constant) $w_o' = 1.3715\times10^{-3}$ (empirical constant)

The significant difficulties in modelling spray cloud generation, propagation and finally impingement are:

1. The wave, wind and environmental parameters are highly dynamic, irregular, interdependent and may have varied scenarios in the cold regions.

2. The spray flux, its liquid content, the spray duration, and frequency depend on the ship design, its speed over water and heading with respect to the wind and waves and its dynamic

behavior. Ships of different geometry, dimension and loading condition interact differently with sea conditions.

3. There is a lack of understanding in the behavior of the droplet during its propagation within the turbulent flow around different types of ship's structure and the near-field biases caused by airflow alterations over the vessel. This ultimately decides the distribution and quantity of incoming water flux at different locations on the vessel, hence questions the reliability and versatility for predicting marine icing from the CFD models, which is also restricted by uncertainties like spray generation method. Moreover, all these models are lacking validation against field observations (Mintu et al., 2016).

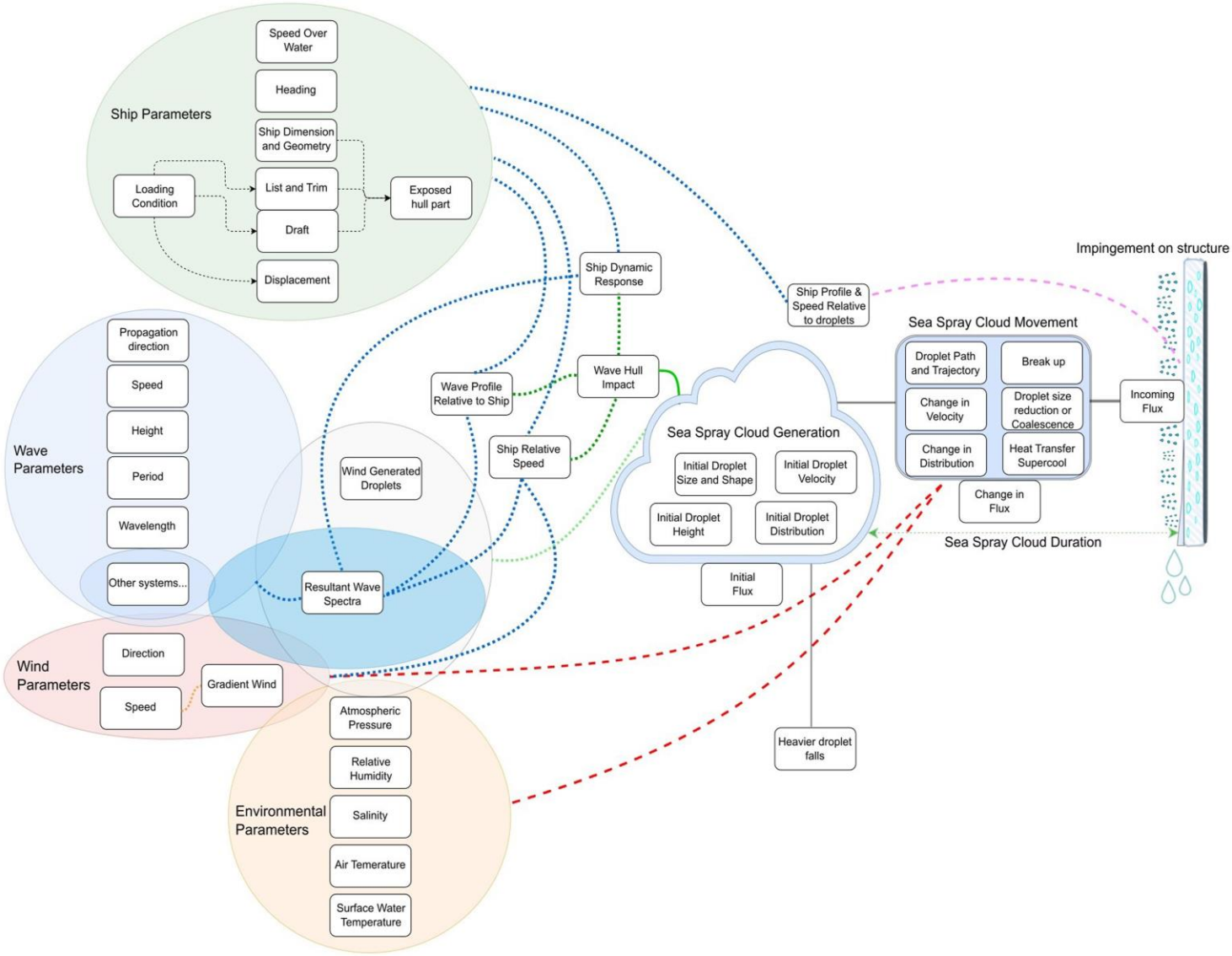

Fig. 2. Showing the complexity and interdependencies in the process of sea spray cloud formation, propagation, and impingement. (Picture from paper 1)

This necessitates direct measurements to gather real-time data of the concentration or spatial distribution of the entire impinging spray to remove errors from each step, in order to develop more practical and functional equations. The formulae used to calculate LWC in a spray cloud, only presents an estimation (Dehghani-Sanij et al., 2017a). The different empirical correlations (Table 1.) are obtained from observation for a distinct set of conditions and do not take into account different vessel parameters; so, they may provide incorrect results if generalized (Rashid et al., 2016; WMO, 1994; Bodaghkhani et al., 2016). Dehghani et al. (2016b) reviewing past sea spray icing models, mention that the lack of recording the distribution of size and velocity in a spray cloud led the researchers to use mono-size and mono-velocity models. There is a lack of empirical observations; consequently, the analytical and numerical formulations are based only on a few actual field observations and not comprehensive data (Dehghani-Sanij et al., 2017a). Hence, there is a need for more accurate field measurement, considering more parameters and scenarios.

2.1.2 Past sea spray field measurements

Some researchers carried out measurements in the past, attempting to measure real-time incoming sea spray on vessels to formulate or validate incoming spray flux or liquid water content correlation and model its distribution to estimate sea spray icing accurately. Tabata et al. (1963) reported field measurements on a few Japanese ships, during which both ice accretion rate and the sea spray intensity were measured (Zakrzewski, 1986). Specially designed icing gauges consisting of a rod suspended in a weight gauge were placed over the ship to measure the icing rate and entrap the sea spray (Lundqvist and Udin, 1977). Later, Tabata (1969) measured the spray amount and distribution on deck aboard a 350-metric ton patrol vessel, with his instrument consisting of water absorption sheet (toilet tissue) in circular cylinder distributed across the forecastle, which was replaced every 5–6 min interval. Then measured the added mass from spray events, fluxes fluctuated from 0.06 to 0.98 kg/m2/h depending upon the cylinder's location on the bow area, and relative wind speed and wave direction (Ryerson, 1995). Brown and Roebber (1985) used the above data sets to present a relation, of the change of time-averaged spray flux as a function of the ship's speed and heading (Zakrzewski, 1986). Ono (1964) measured ice growth rates and the sea spray intensity on patrol boats, from the accreted amount of spray on an icing rod and collecting the excess runoff brine in a calibrated

jar (Ozeki et al., 2016). Itagaki (1984) used this data as a function of air temperature and wind speed to estimate the ice accumulation rate on stationary structures. Sharapov (1971) study provided a data set from a medium fishing vessel (MFV) recording the spraying zone extent for wind speed from 5 to 11 Beaufort. Later, Zakrzewski et al. (1988) used this data for validating the model performance for his correlation for calculating the highest extent spray droplets from wave hull interaction, which was based on field icing data from Kuzniecov et al. (1971). Gashin's study mentioned in Borisenkov & Panov (1972) provided the first direct measurement data for bow-generated spray characteristics, from the analysis conducted on a MFV of 35 m long Soviet fishing trawler. In his data, the spray droplet diameters ranged between 1000 μm and 3500 μm with a mean of 2400 μm, but his measurement methods, environmental and sea conditions during his field trial and variations of his result with different vessel size are not known (Ryerson, 1995). Kachurin et al. (1974) formulated the first LWC correlation as a function of wave height only based on measurement from a MFV, but stated no information about the measurement technique. Borisenkov et al. (1975) published data of spray cloud field measurement made on a MFV in the Sea of Japan, reported ship and environmental parameters though information about droplet size and velocity distribution were not stated. The data was also used for producing empirical LWC formulation and succeedingly used by Zakrzewski (1986) and Brown and Roebber (1985) for extending the formulation, and later showed by Samuelsen et al. (2015) the variation in the empirical constant value differs from the previous study. Method of directly measuring spray flux was carried out in the 1980s on an artificial island (Tarsiut Island) to develop the RIGICE model, the spray data collected from measuring the water level at hourly intervals in 45-gallon drums (Muzik and Kirby, 1992). As a part of the study program “Offshore icing” (Horjen et al., 1986; Jørgensen et al., 1986) measurement of spray flux was carried out on supply vessels, stand-by boats and offshore structures for calibrating the Norwegian marine icing model ICEMOD (Horjen, 1990), the data is also utilized by the later developed icing models MARICE and NuMIS. Spray measurements were carried out with absorption panels consisting of absorbent paper (paper diapers) and bent pipes collecting the impinging spray into a graduated container (Teigen et al., 2019), but no information related to spray droplets were provided (Bodaghkhani et al., 2016).

Ryerson (1995) was the first to carry out the real-time measurement of sea spray on a larger ship (CGC Midgett 115 m length). His experimental setup consisted of vertical and horizontal oriented funnel-shaped spray collectors, ultrasonic range-finding ice detectors, video recording systems and stroboscopic droplet camera. Characteristics of the spray cloud generation

frequency, duration, height, and distribution size were recorded. Also, parameters such as sea and environmental conditions, ship position, speed, and heading, were logged for every hour. The spray flux was measured at six different locations, but the result presented was only for one location. The reported incoming droplet size varied from 14 to 7700 μm, and median of 234 μm, the mean droplet concentration about 4×10^5 droplets/m3, the average cloud droplet concentration of 1.05×10^7 droplets/m3 and average spray event duration 2.37 s was recorded (Dehghani et al., 2016b). He also attempted to form the LWC correlation, but the comparison among his measurements and past LWC correlations were not satisfying. Though his result provided a crucial data set, however, it was based on specimens from the spray cloud and not accounting for the entire distribution data set of the entire spray cloud, and also, the model did not include data on the droplet velocity (Bodaghkhani et al., 2016; Dehghani et al., 2016a). Jones and Andreas (2013) collected sea spray at Mt. Desert rock lighthouse catwalk at 20 m above sea level, to inspect spray generated over the ocean instead from wave and shore impact and was observed under microscopic slides. This project's long-term goal is to estimate the sea spray concentration across the open ocean and sea spray icing on offshore constructions.

Ozeki and Sagawa (2013) modified a snow particle counter into seawater particle counter (SPC), it consisted super-luminescent diode light as a parallel ray measuring light attenuation by particles passing through the sensing area (25 mm wide, 3 mm high, and 0.5 mm deep). The SPC was able to measure the droplet size distribution impinging the sensing area every second and was placed on the upper deck of an ice breaker, and the measuring range was set from 100 to 1000 μm in diameter. By using the result, the flux distribution and the transport rate could be approximated as a function of particle size. Johansen et al. (2015) proposed a study of using a high-speed camera for imaging sea spray and using image analysis (Hough Transform) for measuring the Sea Spray Flux. However, the study could not be deployed for field test because other than the setup being too expensive, most critically it required very sensitive lightning setup, which is very difficult to control in the harsh marine climate. Ozeki et al. (2016) modified a marine rain gauge to measure seawater spray in large ships and found a correlation in measurement with their previously developed seawater particle counter (SPC). Measurement of seawater spray was performed on the compass deck and the bow deck of an icebreaker.

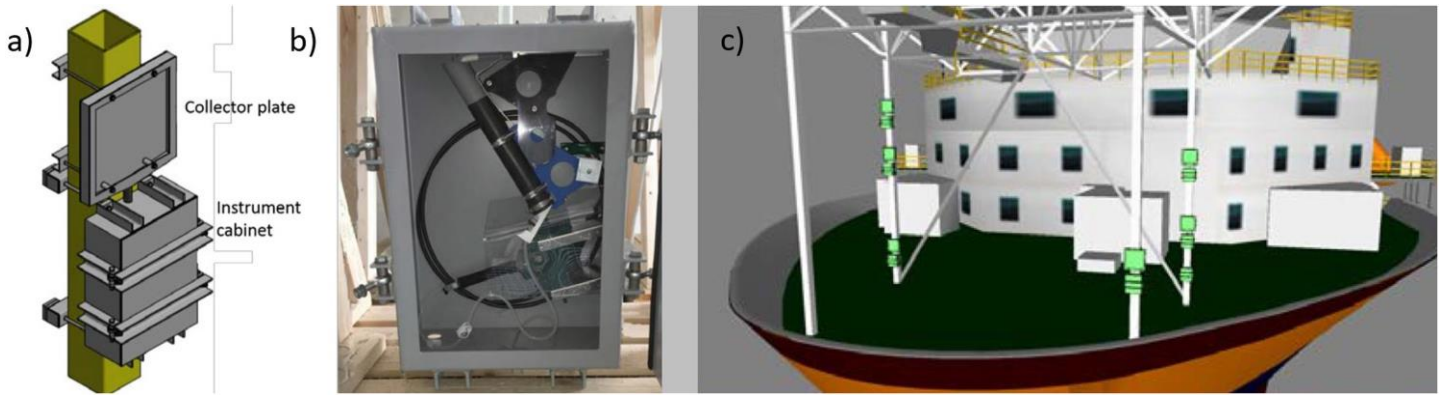

Fig. 3. (a) Fluxmeter Design (b) Instrument cabinet with the tipping bucket (c) Mounting positions of the six fluxmeters in the bow of the Norne FPSO (Teigen et al., 2019).

Teigen et al. (2019) describes the real-time autonomous measurement system designed by modifying a tipping bucket to collect sea spray to measure and record continuous flux on offshore facilities as part of the joint industry project RigSpray. The system (Fig. 3.) consists of flux meters comprising a collector plate (dimensions 0.5 m × 0.5 m) funneling the impinging spray to a tipping bucket via a small hose. The tipping bucket's water level is continuously measured with a wireless gauge pressure, and the water empties automatically after reaching a certain level. The system also includes a video recording system and can transmit the data wirelessly and has been in operation on the ship shaped FPSO unit “Norne” in the Norwegian Sea. The project provides spray measurements data along with the corresponding vessel motion and environmental dataset, which is important for calibrating spray models on large ship-shaped offshore structures (The RigSpray icing model, Bøckmann et al., 2019).

The measurement techniques and data collection and analysing procedures have improved over time and have proven to be helpful because of its simplicity and robustness in the harsh climates. However, the past studies were only able to measure samples of spray flux from some specific parts of a spray cloud and approximations were made on the basis of the localised measured data. So, for other conditions, the droplet size and concentration need to be assessed for the entire spray cloud from the approximated proposed distribution. Also, the prevailing micrometeorological conditions substantially affect the results during the field trials varyingly at different locations on the ship. Hence, they fail to provide a factual comprehensive time-resolved distribution data set for the entire spray cloud. Information the past studies could not provide about the entire impinging spray cloud such as its complete droplets distribution, velocity, and concentration which is inherent for the formulation of accurate correlation of spray flux, vertical distribution, and the spray cloud's maximum height. Therefore, it is

necessary to adopt different setups or measuring techniques which can carry out real-time monitoring in spatial and temporal resolution to measure incoming sea spray flux for the complete spray cloud with higher efficiency and accuracy.

LiDAR (Light detection and ranging, also known as laser radar) is an optical sensing technique that has been used extensively in atmospheric studies, and has the potential to break through the shortcomings mentioned above, as it is possible to use this technology for carrying out real-time active measurement of entire spray cloud with high temporal and spatial resolution

2.2 Spray drift studies using LiDAR

Due to the high temporal and spatial resolution and latterly scanning ability, LiDAR systems had been fairly utilized as a method for monitoring pesticide spray drift and particulate matters in the agricultural application. Some of the promising studies used for monitoring spray drift are mentioned which shows its potential to be used in the field of marine icing for analyzing sea spray cloud.

The first research carried out by the U.S. Forest Service, Stanford Research Institute group in 1966 – 1967, investigating the use of LiDAR to monitor the dispersal of insecticide spray in the forests of Idaho. Air motions were observed by tracking spray and smoke clouds and also displayed how turbulent, and other diffusive processes can be analyzed (Collis, 1968). Atmospheric Environment Service (AES) of Canada constructed an elastic backscatter LiDAR system (ARAL) capable of fast attainment to analyze spray geometry and deposition of pesticides from an aerial application by scanning the cross-section of the spray (Hoff et al., 1989). Later ARAL was used by Mickle (1994,1996) to analyze the dynamics of the pesticide spray when aerially released. LiDAR technology also had been used and proven to be an ideal tool to validate theoretical spray-movement models and was able to expose the discrepancies in the models (Mickle, 1999; Stoughton et al., 1997; Tsai, 2007). Another elastic backscatter LiDAR was used to monitor aerially applied biological pesticide spray to support the hypothesis that a widespread dispersal of a small pesticide quantity is unavoidable, even if the operation is adequately handled (Miller and Stoughton, 2000). Miller et al. (2003) used LiDAR ground spray measurements to create 3D images of the spray drift cloud above an orange farm. Hiscox et al. (2006) introduced a methodology to estimate the spray cloud absolute concentration obtained from the LiDAR return signal. From the spray application rate and the initial droplet size distribution, theoretical models of evaporation and deposition were used to simulate droplet

quantity's temporal evolution, which remains in the air from aerial spray application. They detected a satisfying correlation in the concentrations estimated from the derived model and the LiDAR return. Institute National d'Optique (INO), Canada specially developed an eye-safe close range (<100 m) LiDAR for the purpose of monitoring pesticide spray drift (Allard et al., 2007; Cantin et al., 2007). Prior this most studies used LiDAR systems whose design was architected for far range atmospheric studies.

The INO LiDAR prototype was tested to validate its performance in the applications of pesticide and dust cloud monitoring. The digitized waveform (Fig. 4.) of the backscattered signals demonstrated that the equipment was able to monitor low signal levels from the water spray drifting cloud (tested with water instead of real pesticide) as well as high signal levels from solid targets (like dust). The result also showed the ability of LiDAR to present important measurement data regarding the relative concentration of airborne aerosols of diverse nature, also at a shorter range (Allard et al., 2007). Khot et al. (2011) describes the methodology used to report the application of calibrated LiDAR to quantify spray distribution across space and time. The results exhibited a linear relationship ($R^2 \approx 0.77$) between the LiDAR backscatter signal of the spray plume and passive spray collection on samplers. Miller et al. (2012) applied a LiDAR to analyze spray drift from near-ground aerosol fogs in several stability conditions concluding that spray coverage is more extensive under strong wind. A commercial ultraviolet LiDAR system (ALS 300, Leosphere, Orsay, France) was used to monitor spray drift (Fig. 5.) for comparing with the measurements obtained from the passive collectors which is conventionally used for measuring pesticide spray drift. The result of the analysis showed a strong linear correlation ($R^2 \approx 0.90$) proving the LiDAR to be a better alternative for monitoring pesticide spray drift with lesser time and resources (Gregorio et al., 2014).

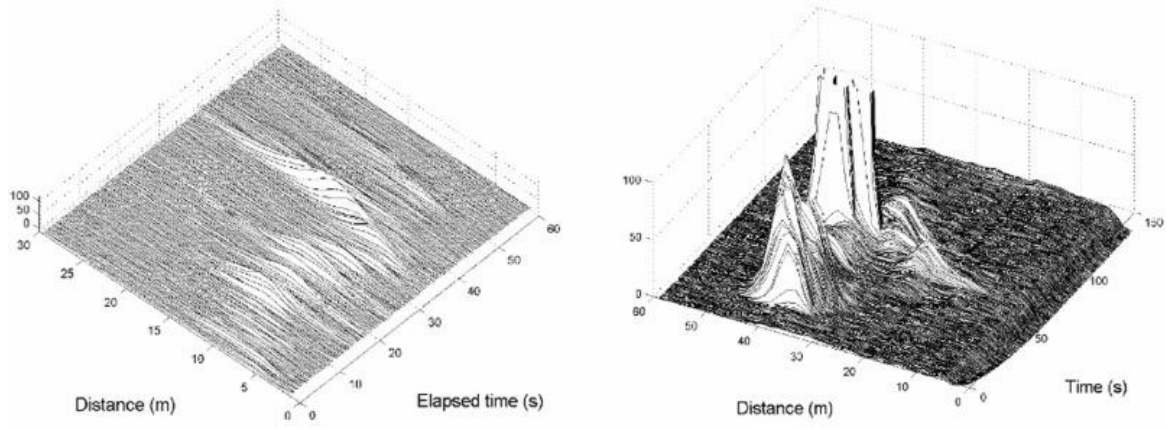

Fig. 4. Showing the time and distance evolution of the backscattered signals from the spray clouds of water droplets (left) and from the dust clouds (right) (Allard et al., 2007).

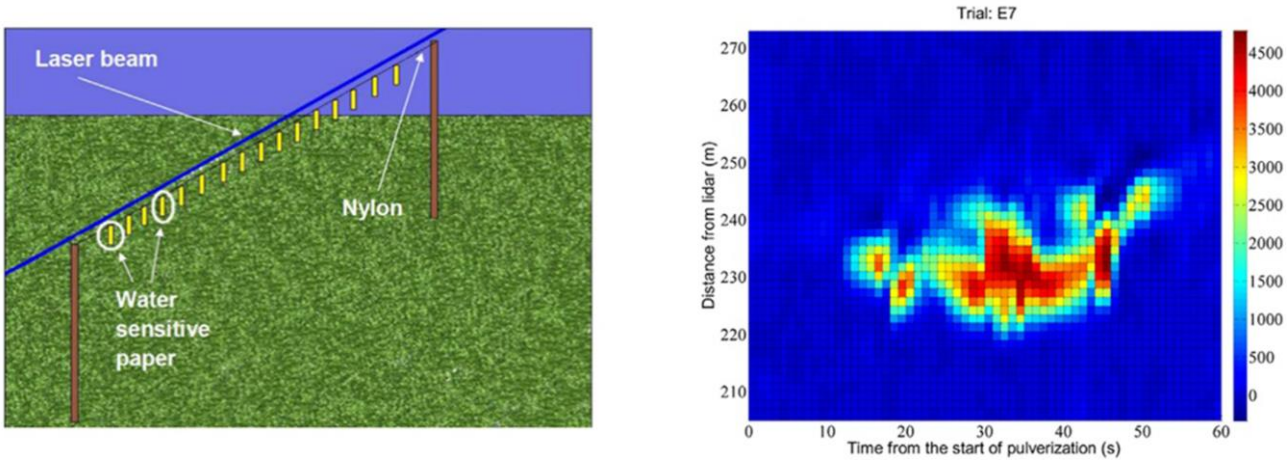

Fig. 5. Showing experimental setup (left) and Range-corrected background-subtracted LiDAR signal (arbitrary units) with a range resolution of 1.5 m and temporal resolution of 1s (right) (Gregorio et al., 2014).

An eye-safe LiDAR system was explicitly designed for the purpose of spray drift monitoring (Gregorio et al., 2015), with a scanning ability via pan and tilt unit up to 25°/s and 12°/s in azimuth and elevation (Gregorio et al., 2016b). The instrument has a laser emitter (Er-glass laser) of 1534 nm wavelength, emitting pulses of 3 mJ energy and 6ns duration. A telescope with 80 mm aperture captures the backscattered light, and it is directed on the photodetector surface of an avalanche photodiode (APD) module which converts the received light to electrical signal (Gregorio et al., 2016b).

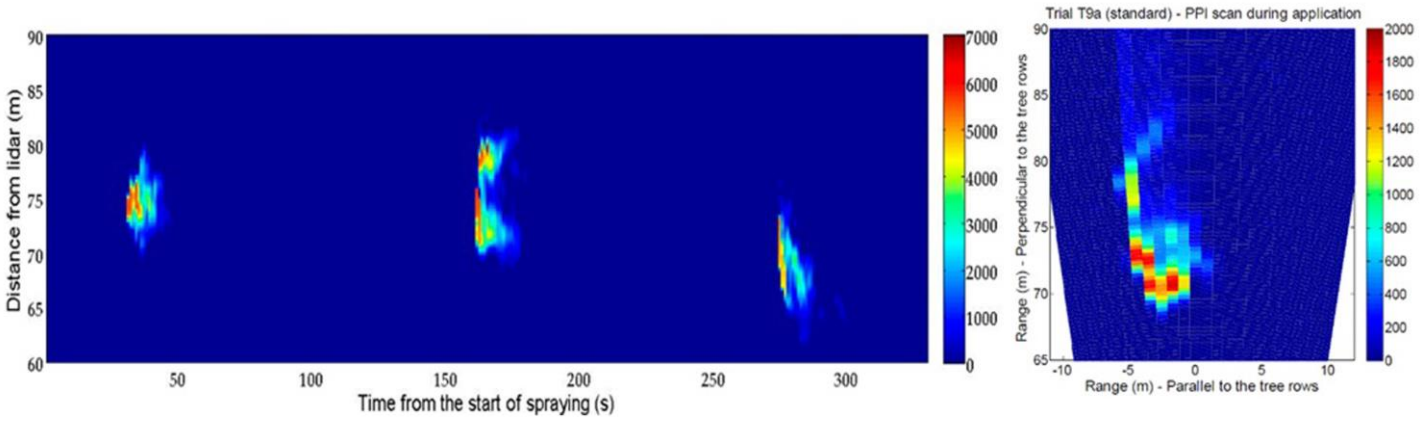

Fig. 6. spray flux over the canopy with temporal (1 s) and spatial (2.4 m) resolution (left) and 2D scans of the spray flux over the canopy, both in azimuth and elevation (right) (Gregorio et al., 2016a).

The temporal and spatial resolution and scanning capability of the LiDAR equipment were tested to observe real time behavior of the drift cloud (Fig. 6, Fig. 7.) under different spray

conditions and the author claimed the LiDAR technique to be an appropriate method to carry out drift measurement with much lesser time, cost and labor compared to using passive collectors (Gregorio et al., 2016a, 2016b).

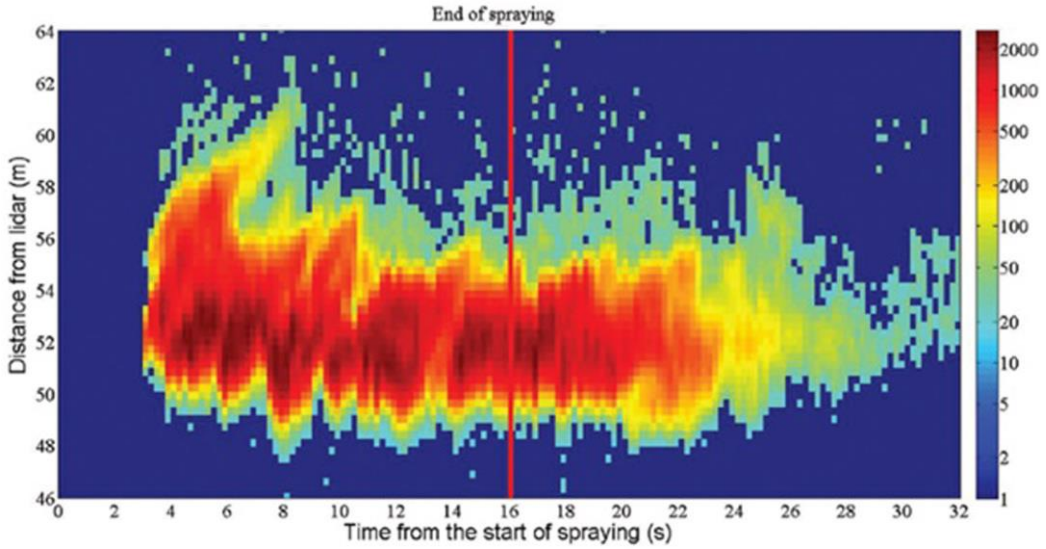

Fig. 7. Range time intensity plot of spray drift with high temporal (200 ms) resolution (Gregorio et al., 2016b).

The past spray studies carried out in the agricultural domain provide evidence for the LiDAR's temporal and spatial resolution capabilities to monitor the entire spray cloud's real-time behavior, which the past sea spray studies failed to provide. Moreover, the LiDAR system enables evaluation of the spray drift speed, its concentration, geometry and evolution with time and ultimately providing a broader view. These results are encouraging to propose this technique, which can be valuable in the field of marine icing due to the similarities of pesticide spray with sea spray for studying the complex sea spray behavior under different circumstances.

2.3 LiDAR

LiDAR (Light detection and ranging also known as laser radar) is a long-existing active range-resolving optical measurement technique commonly used for remote sensing and real-time analyzing of aerosols and clouds in atmospheric studies and presently has broad application throughout almost every field (Gregorio López, 2012; Hulburt, 1937; McManamon, 2019). The LiDAR operates in a principle where laser pulses are transmitted through a medium and a receiver sensor detects the fraction of light backscattered by the particles in that medium (Measures, 1992). Scattering occurs when light interacts(Fig. 8.) with particles in a medium or scatterer, i.e. it is partially deflected deviating from its incident direction with certain distribution probability, and various properties can be analyzed(Table 2) about the matter in the medium from this process. The intensity by which the incident light is scattered by a particle generally depends on its wavelength, its angle with the scatterer and the characteristics of the scatterer within the scattering volume such as its geometric shape and size, refractive index and the particulate number density(Kovalev and Eichinger, 2004).

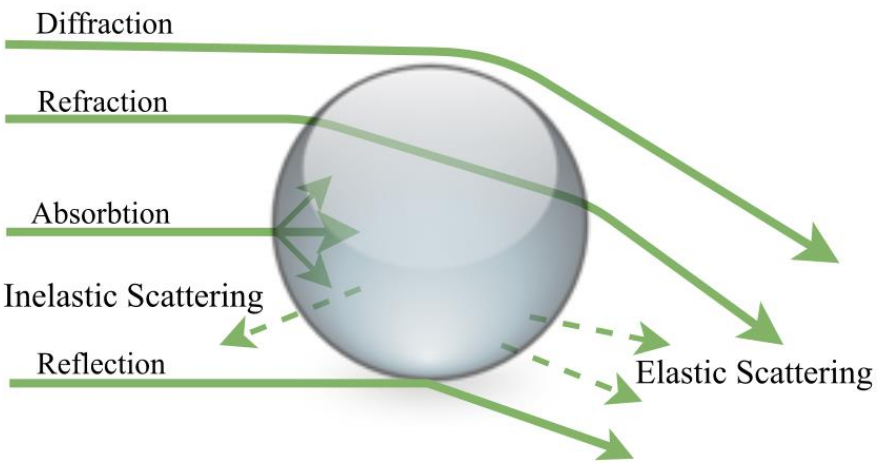

Fig. 8. Modes of interaction of light with a particle during transmission in the medium

LiDAR is a popular choice in atmospheric studies as it can provide information about it with high temporal and distance resolution; due to the substantial interaction between the emitted electromagnetic radiation at optical wavelengths and aerosols or molecular components in the atmosphere from which relevant characteristics are estimated (Measures, 1992).

Table 2. LiDAR equipment their corresponding interaction and observables (Fujii and Fukuchi, 2005)

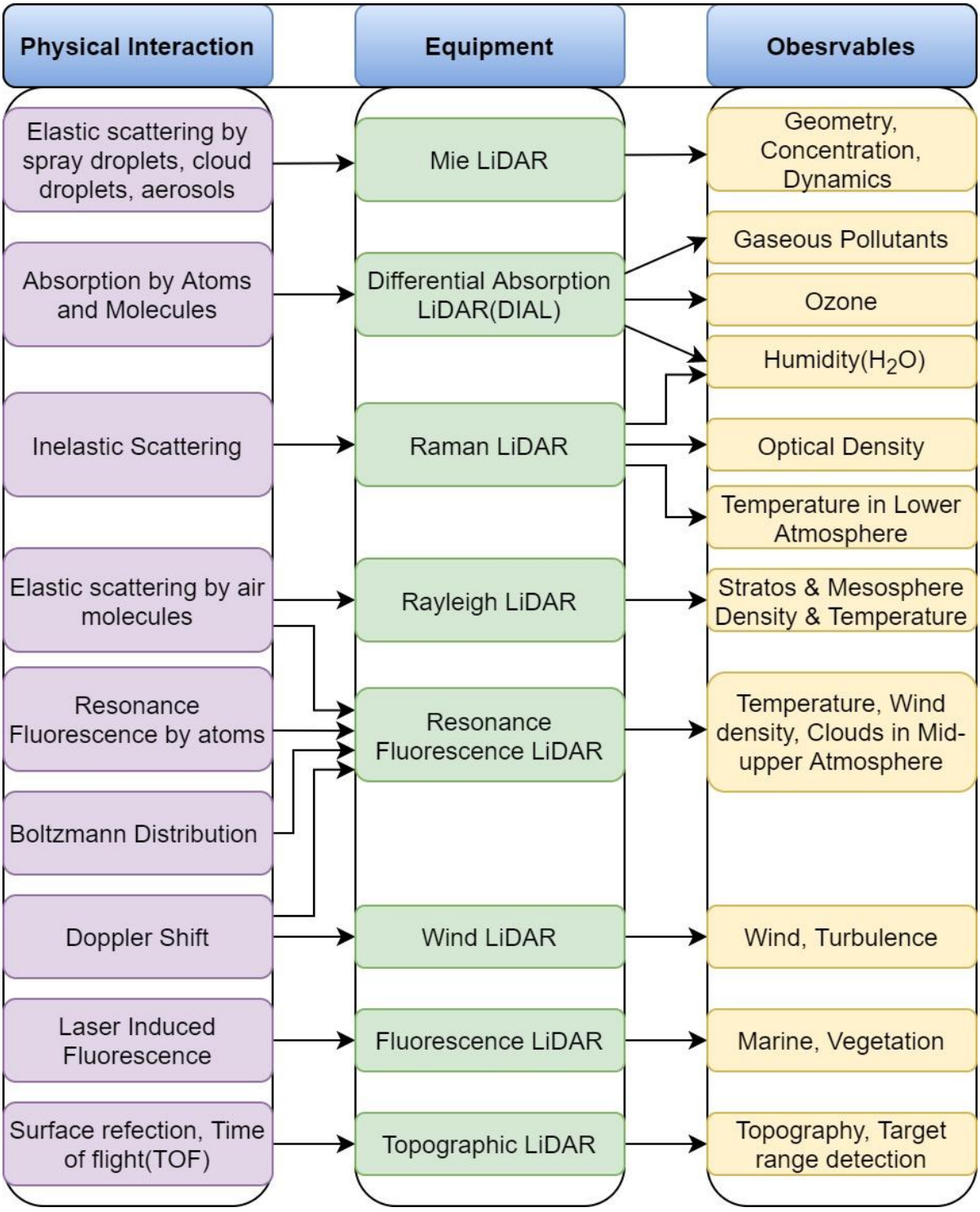

The elastic backscatter LiDAR technique is most commonly used and will be utilized for our application. Other LiDAR techniques such as Raman LiDAR (inelastic), Differential Absorption LiDAR (DIAL) and doppler LiDAR are also used in atmospheric studies.

2.3.1 Elastic Backscatter LiDAR

With the elastic scattering process, the scattered light's wavelength is the same as that of the incident light in the medium and energy of the photons doesn't change in the scattering process (Davis and Schweiger, 2002). Elastic interaction of light with matter relevant for the LiDAR application is generally characterized by the processes Rayleigh, Mie and White scattering, depending on the scatterer's size (Steinbrecht, 1994). **Rayleigh scattering** (molecular/gas scattering) occurs when the scatterer size is very small in relation to the wavelength of the incident light (Hey, 2015). **Mie scattering** (aerosol/particle scattering) usually describes the interaction of light with scatterers whose sizes are comparable to or somewhat more than the wavelength of the incident light (Mie, 1908). In fig.9, scattering phase functions are estimated by a Mie-based method for an incident light of wavelength 1μm for spherical scatterers of refractive index 1.5 and compared with increasing radius (Hey, 2015). When the scatterer radius is 0.1μm, 10x lesser than the incident light wavelength, the forward and backward scattering patterns are similar. If the radius is further reduced to 0.01μm, the forward and backwards scattering patterns become almost symmetric approaching the Rayleigh scattering.

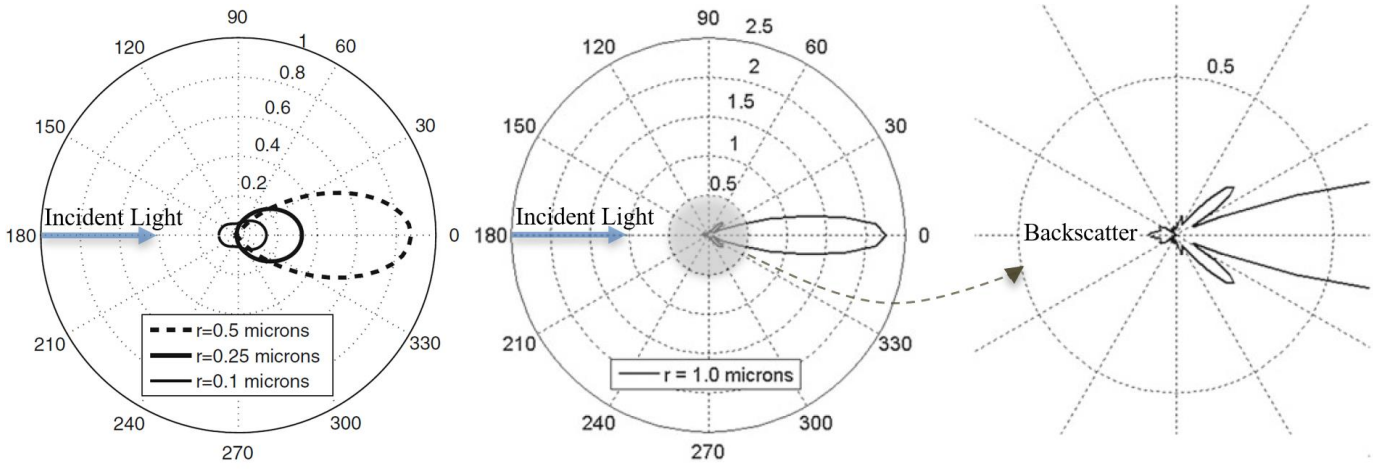

Fig. 9. Scattering intensity of 1000nm wavelength light as a function of angle with increasing scatterer radius of refractive index 1.5(Hey, 2015)

With the increase in scatterer radius in comparison to the incident wavelength, the pattern shifts further becoming pointed in the forward direction with lesser backscatter. **White scattering** takes place when the scattering particles are much larger compared to the incident wavelength. The cross-sections become independent of the wavelength, and geometric optics can be used to describe it, hence also called geometric scattering.

In the elastic backscatter technique, the LiDAR equipment transmits a series of laser pulses, and after interaction in the medium, a small fraction of light is scattered back in the direction opposite to that of the incident radiation. The received signal consists of a sequence of scattered back pulses collected by a telescope, which focuses on a photodetector that measures the amount of backscattered light in the same wavelength received over a range which is determined by the system's optomechanical design. The backscattered light received at the photodetector is converted to electrical signals, this analog signal is digitized by ADC (analog to digital converter) and then processed by a computer to get the desired measurement. From the understanding of atmospheric dynamics with principles of light scattering of particles, the received signal can evaluate profiles of the volume backscatter coefficient, the volume extinction coefficient, the total extinction integral, and the depolarization ratio by interpreting the LiDAR equation to obtain information about the particles' physical state. The time-resolved signal can also measure the distance of the scatterer. Elastic backscatter lidars technique has been used as a valuable tool for mapping, monitoring, transport and dilution study of particulate matters, aerosols, pesticide spray, etc. (Fujii and Fukuchi, 2005; Gregorio López, 2012; McManamon, 2019).

2.3.2 The LiDAR Equation

For a mono-static LiDAR (discussed in section 2.3.3) used in our application, the received backscattered signal on the photon detector: the total radiant flux (F_{bsc}), is expressed as

$$F_{bsc} = F_{e\_sin} + F_{e\_mul} + \sum F_{ine} \qquad \text{equation 2}$$

Where, F_{e_sin} is the elastic single backscattered (photon interacts with only one scatterer prior to detection) radiant flux, F_{e_mul} is the elastic multiple scattered (photon interacts with more than one scatterer prior to detection) radiant flux and $\sum F_{ine}$ is the inelastic component of the backscattered signal i.e.. the total of the reemitted radiant fluxes at wavelengths shifted from that of the emitted light's wavelength. The individual scattering components is that part of the scattered light, which is emitted at a direction of 180° (Hey, 2015; Kovalev and Eichinger, 2004). The inelastic component ($\sum F_{ine}$) value is relatively smaller compared to the contribution of the elastically scattered light ($F_{e\_sin} + F_{e\_mul}$) and can be removed from the received signal by

optical filters (some LiDARs such as Raman LiDAR extract useful information from $\sum F_{ine}$). Also, for a relatively clear transmission and non-turbid medium, the amount of singly scattered light (F_{e_sin}) is significantly dominant than the multiply scattered component (F_{e_mul}). Another significant limitation for measuring the received backscatter signal is the presence of noise added by the solar background. For our purpose, the most useful information is F_{e_sin}, but unfortunately, there are no fully efficient ways to get rid of either the solar background noise or the F_{e_mul} contribution. There are certain methods to suppress these effects to a moderate extent, such as reducing the FOV of the telescope, applying narrow-spectral-band filters, the use of transmitted wavelength away from the most intense parts of the solar spectrum and enhancing the laser power (Kovalev and Eichinger, 2004).

Transmission and Extinction

The transmission and extinction of light propagating through a medium are vital considerations for deriving the LiDAR equation. Kovalev and Eichinger, 2004 describes it in the following approach:

$$T(H) = \frac{F_{out}}{F_{in}} \qquad \text{equation 3}$$

Where T(H) for a particular wavelength is the transmittance of a layer of thickness H and represented as the ratio of the outgoing radiant flux F_{out} to the incoming radiant flux F_{in}. Its value ranges between 0 where the light while propagation through a medium gets fully attenuated, and 1 where the light doesn't undergo any scattering or absorption. In a real case scenario, propagation through a non-homogenous medium where the transmission is range-variable, α(r) the range-dependent extinction coefficient function is considered, which is the product of number concentration and extinction cross section $\sigma_{j,ext}$ for each type of scatterer j. The extinction happens due to scattering and absorption in the medium (Hey, 2015).

For elastic scattering,

$$\alpha(r) = \sum_j N_j(r)\sigma_{j,ext} = \beta_T(r) + \alpha_A(r) \quad [m^{-1}] \qquad \text{equation 4}$$

Where, $\alpha_A(r)$ is the the absorption coefficient and $\beta_T(r)$ is the total elastic scattering coefficient.

The change in radiant flux dF over a differential element is expressed as a function of α(r).

$dF(r) = -\alpha(r)F(r)dr$ equation 5

from this the Beer-Lambert-Bouger law, relating F_{out} to F_{in} radiant flux, can be determined such that:

$$F_{out} = F_{in}\, e^{-\int_0^H \alpha(r)dr}$$ equation6

Substituting equation 5 with equation 3,

$$T(H) = e^{-\int_0^H \alpha(r)dr}$$ equation 7

$\int_0^H \alpha(r)dr$ is the integrated extinction along the propagation path and hence used to denote the optical depth τ_α.

Elastic Lidar Constant

Wandinger, 2005 expressed the parameters which affect the measurement of backscattered light as a system constant K_s, which depends on the transmitted laser pulsed power P_o or energy E_o. The duration of the laser pulse τ (full width at half maximum), $c \approx 3\times10^8$ m/s ≈ 30 cm/ns is the Einstein constant, where the factor $\frac{c\tau}{2}$ decides the range resolution. The receiver aperture area A_o determines the solid angle of the backscatter cross-section that is subtended from a given range, and η is the total efficiency of the instrument's optical pathway multiplied by the detection efficiency.

$$K_s = P_o\frac{c\tau}{2} A_o\, \eta = E_o\frac{c}{2} A_o\, \eta \quad [Wm^3sr]$$ equation 8

Usually, η can only be evaluated to varying accuracy levels depending upon the system's complexity and knowledge of each component's efficiency ; hence, it is generally helpful to find a method to cancel out the dependency on precise information of the system constant(Hey, 2015).

Elastic LiDAR single-scattering equation

The elastic LiDAR equation under the single-scattering approximation considers that the incident pulse is scattered just once, and multiple-scattering effects are omitted. Where molecular returns are insignificant in contrast to aerosol returns, the range-dependent

backscatter β(r) and extinction α(r) coefficients can be expressed as a function of the aerosol and water droplet returns. β(r) describes how much light is scattered at 180° direction, determining the backscatter signal, expressed as $\beta(r) = \sum_j N_j(r) \frac{d\sigma_{j,sca}(\pi)}{d\Omega}$ [$m^{-1}sr^{-1}$]

Where, N_j is the concentration of scattering particles j in the volume of the laser pulse path, and $\frac{d\sigma_{j,sca}(\pi)}{d\Omega}$ is the particles' differential scattering cross section for the 180° direction.

The LiDAR single-scattering equation derived from the radiative transfer equation when a distinct laser wavelength is used, providing the backscattered power P(r) detected from range r:

$$P(r) = \frac{K_S\, O(r)\, U(r)}{r^2} \quad [W] \qquad \text{equation 9}$$

Where, K_S is the system constant, O(r) is the range-dependent overlap function (discussed in section 2.3.3), and U(r) is the attenuated backscattering function expressed as:

$$U(r) = \beta(r)\ e^{-2\int_0^r \alpha(r')dr'} \qquad \text{equation 10}$$

Integrated for back and forth extinction of the pulse as it travels from the equipment to the scattering volume at range (r) and returns.

In equation 9, the quadratic factor in the denominator is because of the decrease in solid angle subtended by the lidar receiver and is inversely proportional to the square of the distance from the scattering particle to the detector(Wandinger, 2005).

LiDAR Ratio

From equation 9 and 10, two unknown parameters, the range-dependent extinction coefficient α(r) and the range-dependent backscatter coefficient β(r) need to be determined from only one lidar measurement. The inversion of this underdetermination of the lidar problem requires an intrinsic relationship between the backscattering and extinction cross-sections to retrieve these two parameters (Ceolato et al., 2020). As the correlation between the α(r) and β(r) varies depending on the content of the measurement volume on the size, shape, or composition of scattering particles at each range (Gaudfrin et al., 2020). The LiDAR ratio(LR) is expressed

considering these differences, as the ratio between the range-dependent extinction-to-backscattering ratio (Kovalev and Eichinger, 2004).

$LR = \alpha(r) / \beta(r)$ equation 11

For most elastic LiDAR measurements, the LiDAR ratio is a fundamental unknown, and the accuracy of assumption made concerning the lidar ratio infers the quality of elastic LiDAR inversion (Hey, 2015).

Elastic Lidar Inversion

The inversion technique is applied to evaluate the physical meaning and ascertain the scatterer's optical properties from the received LiDAR signal. Several techniques for the inversion of elastic lidar signals have been implemented. Citing the significant methods used:
Collis (1966) described the first lidar inversion method, the slope method for homogeneous atmospheres from lidar returns. A close boundary solution first implemented by Barrett and Ben-Dov (1967), uses an assumed or determined value of the extinction coefficient at the beginning of the analysis range and inverts the signal in the forward direction (Hey, 2015). Klett (1981) offered a stable one-component formulation adapted to lidar applications. Later, Fernald(1984) and Klett (1985) extended it to a two-component formulation, separating molecular and aerosol contributions (Gaudfrin et al., 2020). Weinman (1988) introduced the optical depth solution, which uses the total optical depth or the related transmittance over the entire LiDAR analysis range as the boundary value while finding the particulate extinction (Adam, 2006). Gaudfrin et al.(2020) introduced a new method for LiDAR inversion in a condition such as near range horizontal measurements where a volumetric layer (molecular Rayleigh scatterers) of the high troposphere is not feasible (we intend to use this method for our future work and is discussed in the appendix section). Also, there are several alternatives, adaptations and combinations of these techniques, and they utilise a different set of assumptions to perform the inversion (Kovalev and Eichinger, 2004).

Attenuated Backscatter

As the inverted profile depends significantly on the inversion method, it is not usually used for comparing analyses from different instruments. The attenuated backscatter $\beta'(r)$ is the range-

corrected, overlap-corrected, calibrated signal, and this profile is most commonly applied for instrument comparison (Hey, 2015). It can be expressed as the product of backscatter and transmission:

$\beta'(r) = \beta(r) T_{tot}^2(r)$ equation 12

Where T_{tot} is the total transmission through all scatterers in the medium.

It can be further extended as the range corrected power $P(r)r^2$ divided by the system constant K_s and the overlap function $O(r)$.

$$\beta'(r) = \frac{P(r)r^2}{K_s O(r)} = \frac{P(r)r^2}{P_o \frac{c\tau}{2} O(r)\, A_o} \quad [m^{-1}sr^{-1}] \quad \text{equation 13}$$

2.3.3 The LiDAR Configuration and Overlap Function

An elastic backscatter lidar is usually designed into two types of configuration: the transmitter and the receiver's relative location. **1) Bi-static configuration** - The transmitter and the receiver are separated by a considerable distance, and a continuous wave laser may be used as a transmitter. **2) Mono-static configuration** - The transmitter and the receiver are both at the same location. Most of the modern LiDARs use a mono-static configuration with a pulsed laser transmitter, which renders better range resolution and more stable beam collimation. For mono-static LiDARs, commonly two different laser beam and receiver axes geometrical setups are used: **(1) Mono-Static Biaxial** - where the laser beam is transmitted outside the receiver's FOV, and the two axes are parallel, or almost-parallel (fig. 10.) **(2) Mono-Static Coaxial** - where the laser beam is transmitted inside the receiver's FOV, with the axes of the transmitted laser and telescope FOV coincides (fig. 11.)(Fujii and Fukuchi, 2005).

The **LiDAR overlap** can be described from an instrumental aspect, as the equipment's backscatter signal acquisition efficiency affecting with the distance of the scattering volume from it. Due to this incomplete overlap region or LiDAR blind zone, the backscatter signal from the near range isn't fully acquired by the receiving sensor, which heavily impacts (and prevents) measurements near the instrument. The minimum distance the receiver can acquire backscattered signal depends on the pulse laser's geometrical setup towards the receiver and their FOV. Geometrical compression (GC) is a consequence of diminished detector response to

the received signal due to a lack of perfect coincidence of the emitted signal in the telescope's whole field of view (Stelmaszczyk et al., 2005).

Stelmaszczyk et al. (2005) described the overlap function or the geometrical compression factor O(r) as the ratio of the energy gathered by the photodetector E_{det} to the energy arriving on the telescope's primary lens or mirror E_{prm}.

$$O(r) = E_{det}(r) / E_{prm}(r) \qquad \text{equation 14}$$

He further extended for defining telescope's effective area A_{eff} as:

$$A_{eff}(r) = O(r)\, A_O \qquad \text{equation 15}$$

Where, A_O is telescope's primary lens (objective) or mirror area.

O(r) values range from 0 to 1, where 0 corresponds to a situation when no overlap occurs between the laser beam and the telescope's FOV, where the laser is focused outside the detector's sensitive area. The value gradually increases with distance from the receiver, and at a point at which the backscattered signal is wholly registered, the value becomes 1. The closest distance when the beam remains entirely within the telescope's FOV is referred to as the full-overlap distance. Onwards this point, the laser beam stays within the FOV of the telescope, and each point on the telescope primary lens or mirror has a similar backscatter signal collecting ability. This is true only if the FOV of the telescope diverges faster than the divergence of the laser beam, and the laser is not tilted such that it exits the telescope FOV after some range.

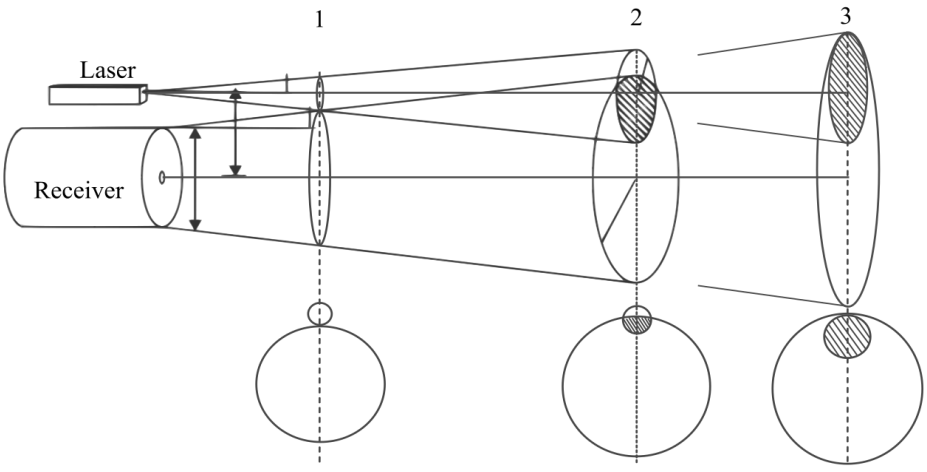

Fig. 10. Mono-static biaxial LiDAR configuration depicting the overlap area with increase in distance

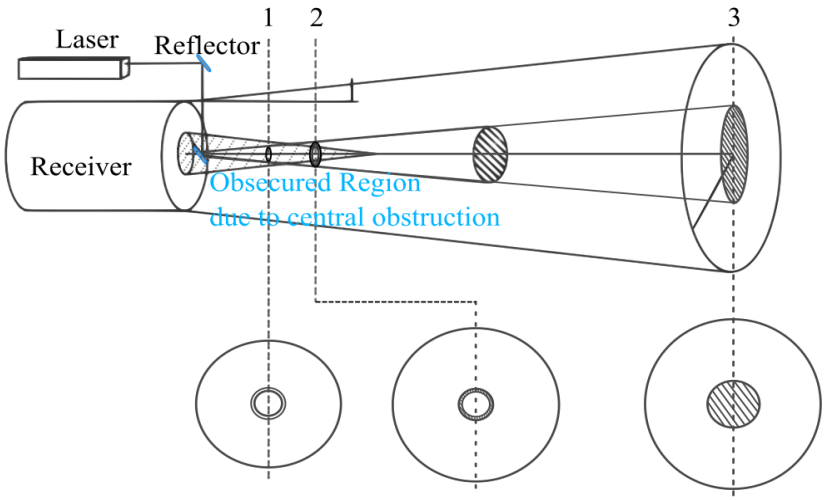

Fig. 11. Mono-static co-axial LiDAR configuration depicting the overlap area with increase in distance

In fig.10 & fig.11, **Point 1** corresponds to the range at which there is no overlap between the laser beam and the telescope's FOV. At this range, the overlap function or the geometrical compression factor O(r) value is 0. This region between the equipment and Point 1 is also known as blind zone, as the receiver in this region cannot receive any backscatter signal.

At **point 2**, The value of O(r) ranges between 0 and 1, where a part of the beam doesn't fully coincide with the FOV of the telescope. The region between Point 1 and Point 2 is known as the transition zone or incomplete-overlap zone, as the receiver receives partial backscatter signal. Onwards **point 3**, the value of O(r) becomes 1, where the beam stays within the FOV of the telescope. The region Point 3 onwards is known as full-overlap zone as the receiver registers all the backscattered signal.

It is apparently possible to make the transmitted beam, and the receiver FOV axis coincides in a coaxial configuration and make the fractional overlap area identically 1 with common optics (Hey, 2015). The main limitation of this configuration is that the detector saturation occurs when the laser is pulsed, the undesired signal that gets detected from internal reflections at the transmitter optics. Also, the portion of the images for short-range is obscured by the receiver's secondary optics (central obstruction) and thus degrading the measurements at close range (Hassebo, 2012). Hence a coaxial design wasn't considered for our purpose for the MSL.

2.4 Challenges for designing a shipborne LiDAR for sea spray measurement

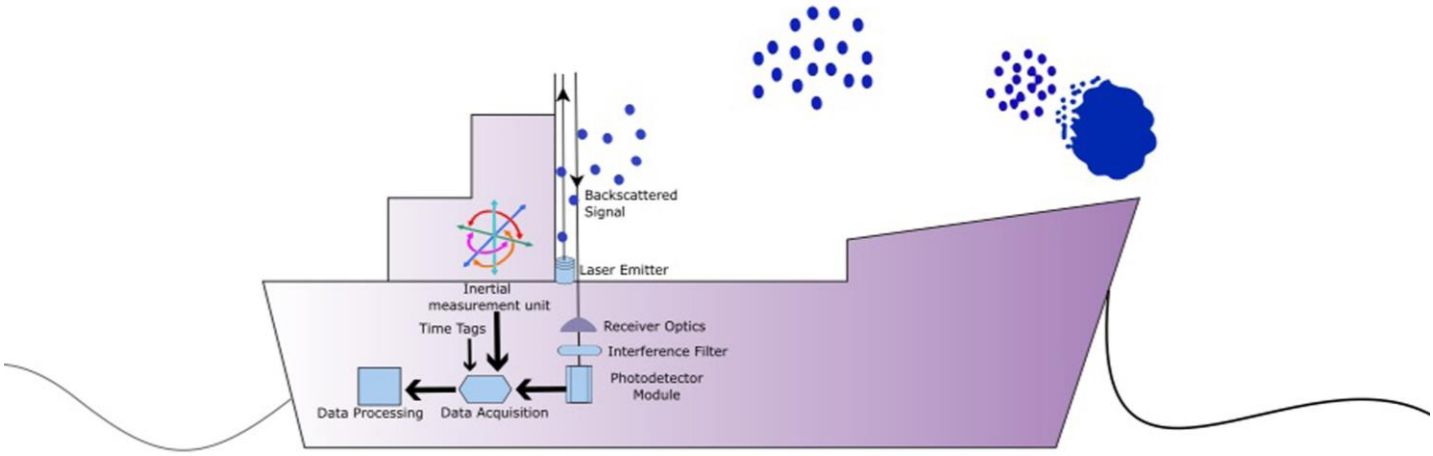

Fig. 12. Conceptual LiDAR set up for analyzing sea spray. (Picture from paper 1)

Application of a LiDAR system suitable for shipborne use for the analysis of sea spray will encounter certain technical challenges that need to be incorporated during the selection of the equipment or during its design phase. The ability for near-range measurement with a high spatial and temporal resolution is essential; besides the equipment being compact, have low power consumption, eye-safe and able to withstand the harsh marine environment is also important.

1. Near-range measurement using LiDAR

Conventional LiDAR systems were mainly designed for analyzing and measuring the atmosphere. Hence, they transmitted high-power pulsed laser (Ruby, YAG, and YLF lasers were used until the mid-90s) and had large aperture receiver telescopes in order to carry out far range measurements (Gregorio López, 2012). The systems were complicated, heavy, had high power consumption, requiring highly skilled operators and were costly (Ansmann et al., 1997; Fiocco and Smullin, 1963; Sassen, 1975). Technological improvements in the last years concerning efficient low-energy and high-PRF lasers and affordable photodetectors in the eye-safe region, let to rise in its application in near range observations such as aerosol-flow imaging, monitoring industrial emission, gas leak detection, etc. (Edner et al., 1995; Fukuchi and Shiina, 2012; Miya et al., 2009; Song et al., 2020). Micro Pulse Lidars (MPL) (Spinhirne, 1993, 1994) and modern commercial ceilometers (Madonna et al., 2014; Muenkel et al., 2004; Song et al., 2017) paved the way for economical, compact and convenient LiDAR systems. Development

in laser technology with Laser diodes (LD) and Diode-Pumped Solid-state (DPSS) further made LiDAR systems more compact and have found a widespread application (Kong et al., 2018; S. Lolli et al., 2011). A LiDAR deployed on a ship for sea spray measurement should have the capability for short-range measurement with a minimum incomplete overlap region, along with being compact with lesser power consumption and have to be reliable in the marine environment. With state-of-the-art advancements, Light Emitting Diode (LED)-based light source has become popular for short-range measurements. Shiina and Koyama (2010a) from Chiba University, Japan developed a compact, lightweight mini LiDAR with a Light Emitting Diode (LED)-based light source for near-range measurements (around ~0 - 100 m), since then it had been utilized in widespread short-range application from the MARS rover to atmospheric studies among others (Koyama and Shiina, 2011; Ong et al., 2018; Shiina, 2010b, 2013, 2019a, 2019b, 2020; Shiina et al, 2015, 2016). The LED lamp module has a larger divergence, and does not require a heat sink or a fan and claims to be cheaper, provide a wide range of wavelength choice, less power consumption, is resilient against static electricity and has extended duration of use with consistent intensity (Shiina, 2019a), hence it has a potential for onboard use for analyzing sea spray.

2. Motion compensation

A LiDAR mounted on a ship for sea spray analysis is going to experience six-degree translation and rotational motion induced by the floating vessel due to action of wind and waves, which will introduce distortions in the LiDAR measurement. This motion needs to be compensated for getting an efficient assessment from the measured data. Generally, two ways for compensating this motion are 1. the mechanical method by placing on top of a motion stabilizing platform (gimbal) which require additional hardware or 2. software-based motion correction algorithm which mitigates the distortion incorporating the motion input from a IMU (inertial measuring unit) (Achtert et al., 2015; Tiana Alsina et al., 2015). Integrating an inertial measurement unit with the LiDAR can enable continuous autonomous long-term high-resolution shipborne measurements in different sea states.

3. Electrical safety

A ship is considered potentially a hazardous environment due to the presence of fuel, oxygen and ignition source, which may lead to fire and explosion. Therefore, while designing any electrical system for onboard use, it is a crucial factor which needs to be considered as it may provide a source of ignition. Either the equipment is required to have an intrinsic design or deployed away from the proximity of any hazard in accordance with SOLAS Ch II-1, Part D (IMO, 2014). The equipment needs to satisfy IECex directives that are accepted globally, or ATEX is accepted in EU, prior to being installed in a potentially explosive atmosphere such as on ships or offshore installations.

4. Weather protection

LiDAR equipment needs to provide high-quality measurement in order to fulfil the purpose of analyzing sea spray accurately. The harsh marine climate can possess a significant challenge for such a study, especially if deployed for a longer time. Apart from waterproofing the LiDAR housing and corrosion protection, the system should have the arrangement to keep the optical module clean or installed in a location where the module is not obscured by saline water, dust or ice. Commercial LiDARs are generally designed to handle harsh climates of low temperature and devised inside a dustproof and waterproof casing. The ALS 300, Leosphere (2009), which was used for pesticide spray study (Gregorio et al., 2014), the optical head has a waterproof and dustproof rating of IP 65 and operating temperature range of −15 °C to +35°C. The control unit can either be shielded in a casing or stored in a protected location such as inside the ship's bridge.

3 Methodology

3.1 MarSpray LiDAR (MSL) Components

An elastic backscatter LiDAR fundamentally consists of an emitter - transmitting pulsed laser signal, a receiver – collecting and detecting backscattered signal and data acquisition – registering the received data and subsequent signal processing from which relevant characteristics are estimated about the scatterer (in our case, spray droplets). The components of the MSL were explicitly chosen concerning its purpose and making the design suitable for analyzing marine sea spray at a close range.

3.1.1 MSL Emitter Unit

The LiDAR emitter section typically consists of the laser source (laser diode in our application) attached to its driver for generating pulsed output and its collimating mechanism for focusing the laser.

1. Laser

The laser which are usually used for atmospheric LiDARs :

(i) solid state lasers (fundamental wavelength) Nd:YAG 1064nm

(ii) solid state lasers (harmonics), 2^{nd} harmonics Nd:YAG 532nm, 3^{rd} harmonics 355nm

(iii) frequency-doubled fiber lasers, 532nm

(iv) diode lasers 905nm

(v) fibre lasers, Er-doped, 1.55µm

Each wavelength mentioned above has its advantages and disadvantages; evaluating those and the technical viabilities, we found **905nm** most reasonable for our purpose of marine spray measurement application. There are, however, certain wavelengths that are likely more favorable, especially when considering atmospheric transmittance and solar spectral irradiances, such as the 532 nm and 1064 nm lasers popularly employed in far range atmospheric LiDARs. Lidars at this wavelength rely on Nd: YAG solid-state laser technology

because of their efficiency from the energy and directional stability perspective, but viewing our cost limitation, using these lasers make the equipment prohibitively costly. Another good option is the 1,550 nm, especially when considering eye safety and lower background light noise. However, the water absorption coefficient at this wavelength is much higher; hence to see any optical SNR advantage, laser technology such as fiber or solid-state lasers would be required, again making the equipment cost not viable.

The **905nm** wavelength was chosen for the MSL essentially for its moderate atmospheric transmission of around 0.6 and comparatively low solar radiation level(fig.13.) at this wavelength. Hence the extinction coefficient and the background noise will be moderately lower during field trials.

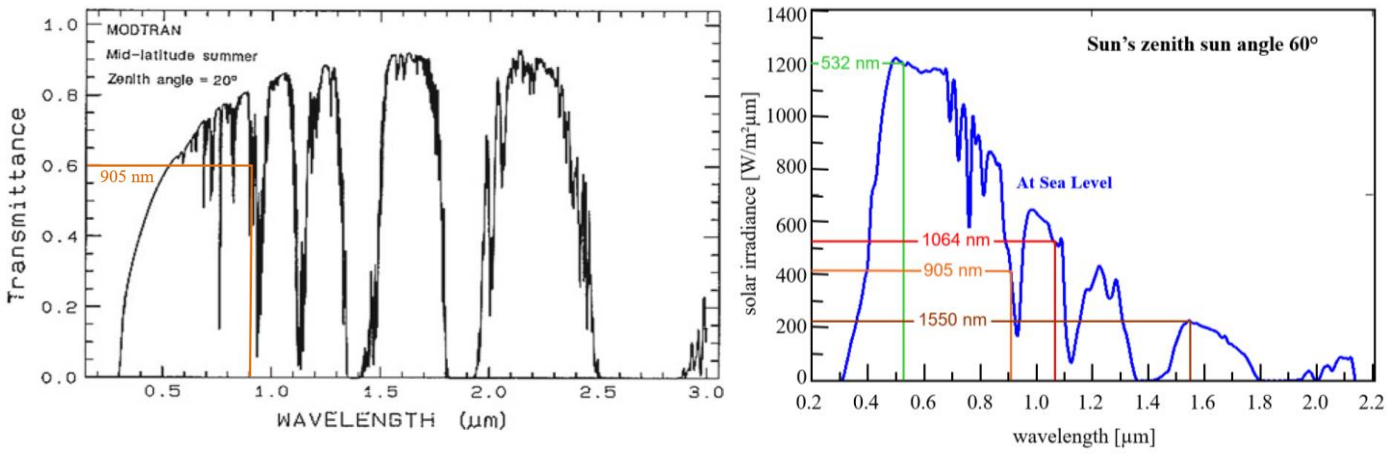

Fig. 13. Left: Atmospheric transmittance as a function of wavelength for a zenith path from sea level to space(Rencz and Ryerson, 1999); Right: and Solar spectral irradiance at sea level(Wolfe et al., 1978)

Also, considering the cost constraints placed on the prototype, at **905nm** there is a wide availability of various kinds of affordable laser diodes of suitable output power compatible with our laser driver, availability of suitable interference filters and reasonably high cathode radiant sensitivity and quantum efficiency of our receiver photodetector (Hamamatsu PMT R5108). Additionally, for later improvement, highly efficient silicon APD detectors are available, sensitive at 905nm.

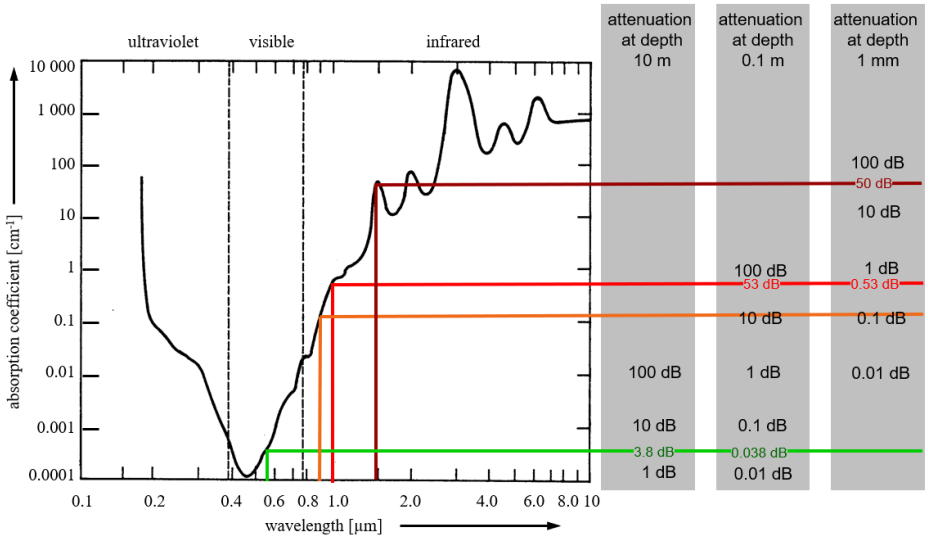

Fig. 14. Water absorption coefficient of clear sea water and attenuation with depth at different wavelengths (Ewing, 1965)

Even though the water absorption coefficient and hence the attenuation in water is much higher at 905 nm (fig.14) than some lower wavelength lasers, the output power can be adjusted to compensate and make the equipment relatively appropriate for short-range sea spray measurements.

After evaluating various 905 nm laser diode, the OSRAM “SPL UL90AT08” laser diode was chosen for the MSL, mainly because of its high-power output. The SPL UL90AT08 laser diode is made of InGaAs (Indium gallium arsenide) semiconductor material, converting an injected electrical power into an output of coherent in-phase light ~905 nm wavelength.

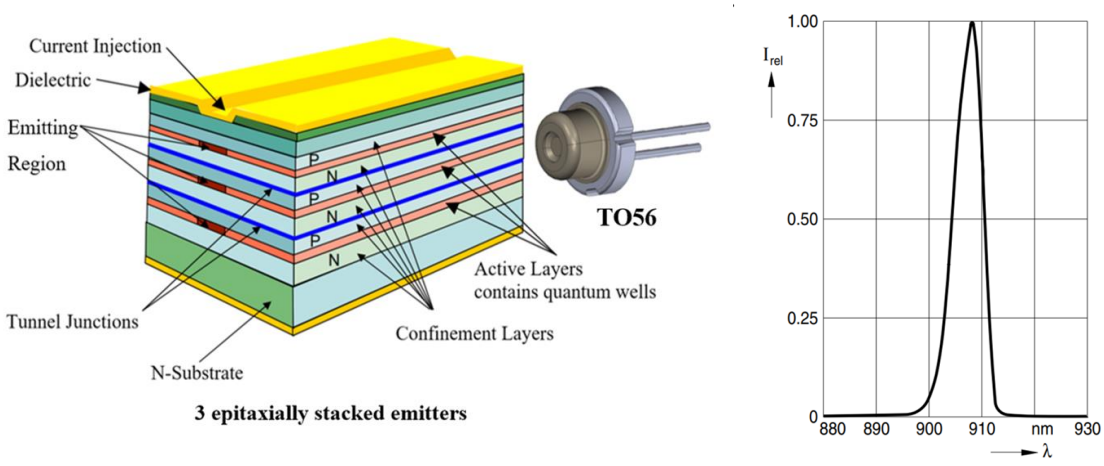

Fig. 15. OSRAM “SPL UL90AT08” laser diode structure(left) and Relative Spectral Emission (right) (OSRAM, 2019)

Laser specifications at 25° C

Peak Output Power	125 W
Centre wavelength	905 nm ± 10 nm
Spectrum full width half maximum	7 nm
Maximum pulse duration (FWHM)	100 ns
Divergence (FWHM) parallel to junction plane	10 ℃
Divergence (FWHM) perpendicular to junction plane	25 ℃
Laser aperture (FWHM) parallel to junction plane	220 μm
Laser aperture (FWHM) perpendicular to junction plane	10 μm
Maximum Duty cycle	0.1 %

2. Laser Pulse Driver

A pulsed laser diode driver is utilized to operate a current-operated semiconductor such as the laser diode. It is a voltage-controlled constant-current source meant to produce a repeatable set of current pulses at a set output level over a period determined by the operator. For our operation, we chose the TIDA-01573(Texas Instrument, 2018) for driving the SPL UL90AT08 laser diode, mainly because of its capability of delivering high current (~60A) and very short (~1ns) current pulses and switching frequency ranging up to 1 MHz. Moreover, the driver being compact and small-size, appropriate for monostatic design and economical as no feedback loop is used.

The laser driver TIDA-01573 basically consists of the GaN FET (EPC2019 FET) which is a fast electronic switch that pulses a DC voltage to the switch node, where the laser diode sees the full input voltage(V_{BUS}) minus the forward voltage drop of the laser. The GaN FET is driven by the low side gate driver LMG 1020, and the drain of this GaN FET is connected to the laser diode load for our LiDAR applications. The board receives logic-level trigger input from the function generator(the signal can be further buffered or shortened by the pulse shortener between 1 and 2ns on the board) that regulates the width and repetition rate of the pulse output from the laser diode.

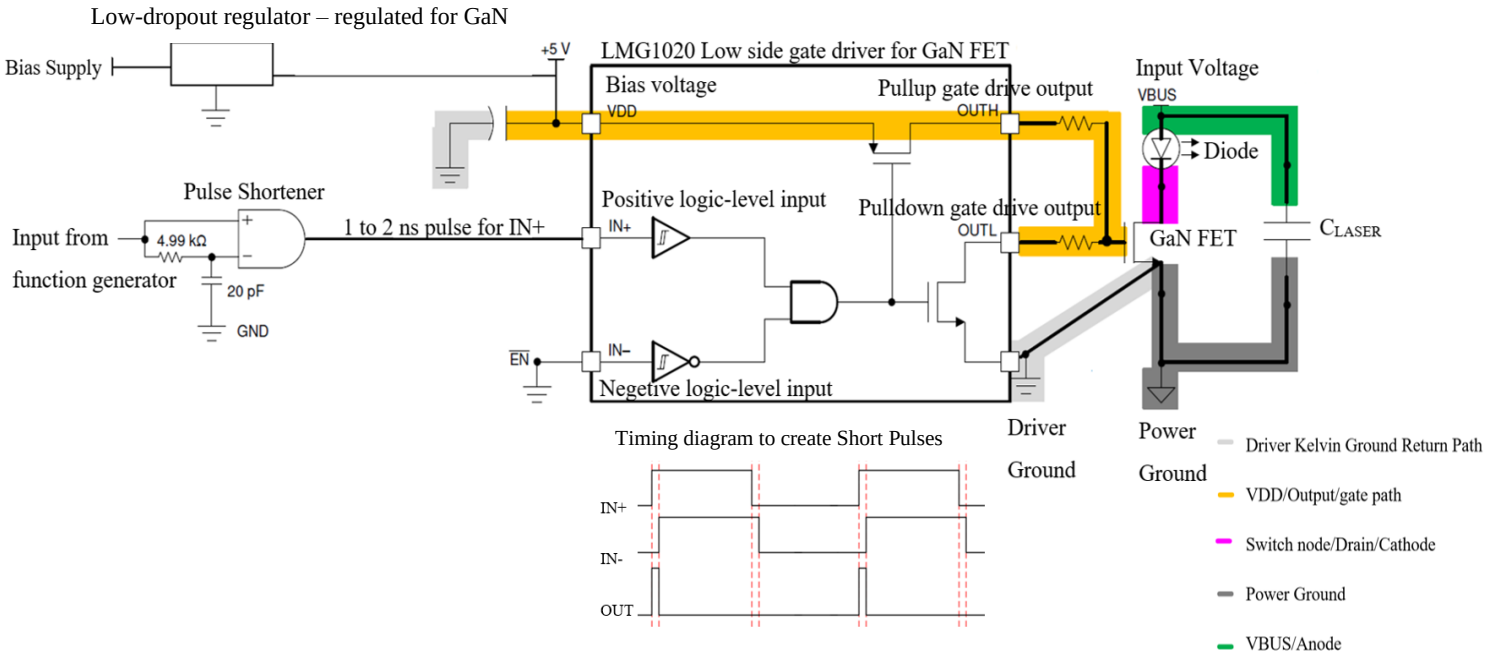

Fig. 16. TIDA-01573 laser driver depicting essential gate loops (Texas Instrument, 2018)

Generating desired short, clean laser pulse output from the diode driven by this driver was probably the most challenging part faced while developing the MSL. When pulsing a laser at high repetition rates, the obstacle is pulse degradation due to overshoot, and ringing(fig.17.) occurs due to improper impedance matching, which is apparently a drawback of this kind of drivers.

Fig. 17. Initial pulses generated showing heavy ringing

As current sources intrinsically possess high output impedance, contrary the laser diodes have very low impedance. When the impedance levels of the load to the impedance of the transmission line are not equaled, in that case, Lenz's law of electromagnetism comes into play, which states that "the direction of current induced in a conductor by a changing magnetic field due to Faraday's law of induction will be such that it will create a magnetic field that opposes the change that produced it"(Lenz, 1834).

$$V = -L \, {di}/{dt} \qquad \text{equation 16}$$

Where V is the voltage, L is the inductance, and ${di}/{dt}$ is the rate of change in current over a definite period. Equation 16 shows that the energy stored in the inductor's' magnetic fields during the pulse needs to dissipate when the pulse stops. This generates a voltage, which in turn produces a new current, which in turn causes a new magnetic field on the transmission pathway, and the loop continues. This inductance loop causes the ringing on the pulse waveform and degrading the pulse.

To overcome this, we removed any possible metal connections adding resistance and inductance between the diode and the laser board, which is contributing to this effect. The diode leads (anode and cathode) were made as small as possible and soldered directly on the board, and the common lead was removed.

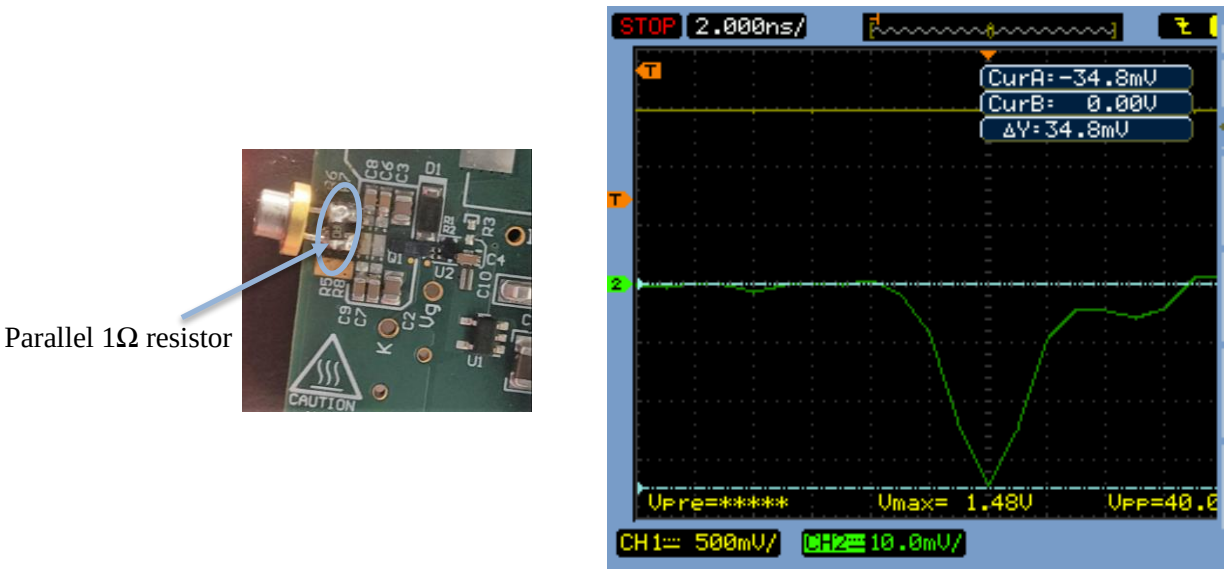

Fig. 18. Laser diode with a parallel 1Ω resistor soldered generating moderately clean output pulse

Then, to match the impedance from the driver to the laser, soldered a 1-ohm resistor in parallel(fig.18.) to reduce the parasitic inductance. The value had to be equivalent to the difference between the output resistance of the driver and the laser diode dynamic impedance. Assessing the dynamic impedance of the laser diode was the most time consuming and challenging part. After multiple trial and error, examining the output by soldering different resistor values before finally getting the desired pulse(fig.18.).

3. Laser Collimation

The “SPL UL90AT08” laser diode used has an oblong-shaped emitter. The emitted beam has a wide divergence (10° ØII slow axis × 25° Ø⊥ fast axis) featuring low wavefront quality and high astigmatism, which needs to be collimated to improve the beam quality.

The purpose of collimation:

1. Diminish the divergence of a beam as much as possible
2. Reduce astigmatism
3. To better wavefront quality
4. To control ellipticity of the beam
5. Maintain good focusability

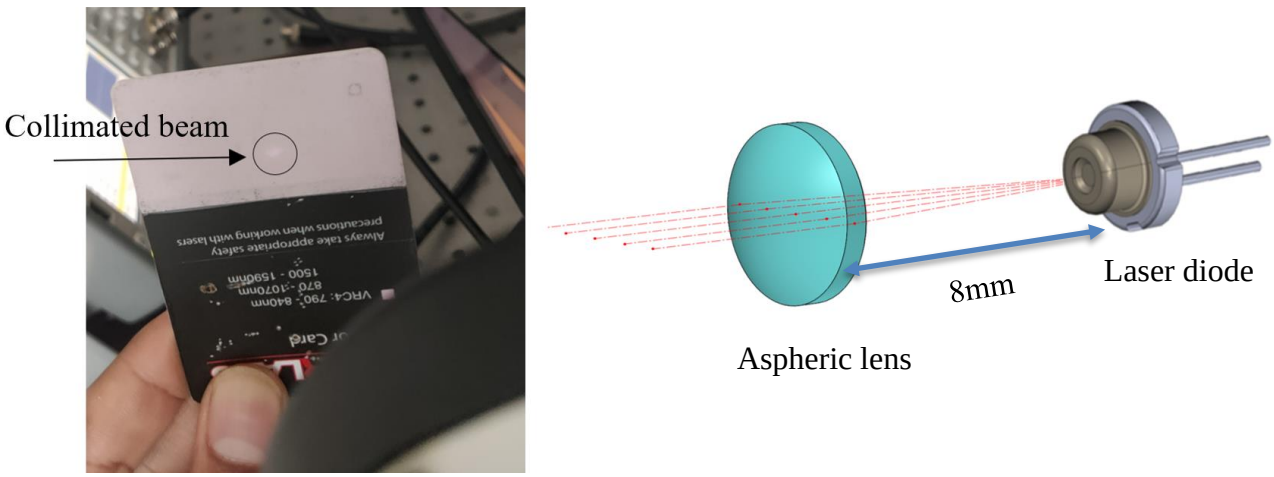

Fig. 19. Single aspheric lens of used for collimating the laser beam

A single aspheric lens (7mm diameter and 8mm focal length) was used to focus the beam by placing the lens a focal length distance away from the laser diode. A drawback of working with the 905 nm wavelength laser is it is not visible to the naked eye. So, we used an IR detection card (fig.19.) to check the collimation quality.

Due to cost restriction, we used the single aspheric lens to collimate the laser beam. But using a single lens makes the beam elliptical, and the aspheric lens induces aberration and diffractions, eventually degrading the beam structure. The laser beam quality can be further improved by updating this component using a two-lens system.

3.1.2 MSL Receiver Unit

The receiver unit consists of the telescope, which collects and focuses the backscattered signal to the photodetector (photomultiplier tube), the photodetector senses this and converts it to an electrical signal, and a bandpass filter in front of the detector, letting only the wavelength interest reach the sensor.

1. Telescope

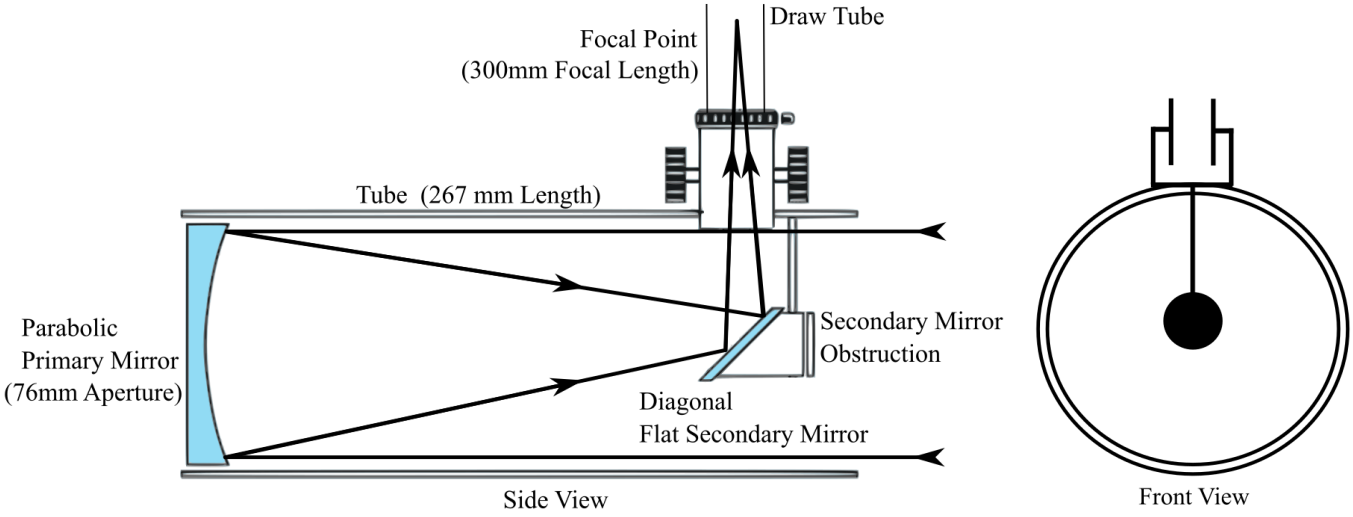

Fig. 20. f/3.95 Newtonian Reflector MSL Telescope

Telescope Specifications

Optical Design	Newtonian Reflector
Aperture	76mm
Focal Length	300mm
Focal Ratio	f/3.95
Secondary Mirror Obstruction	28mm
Secondary Mirror Obstruction by Diameter	37%
Secondary Mirror Obstruction by Area	14%
Mirror Coatings	Aluminum with SiO_2

A reflector type telescope was chosen for the MSL, as it reduces the equipment size and weight considerably. A short f ratio of 3.95 (focal length of the telescope divided by its aperture) was chosen, as it maintains a rich field of view (FOV) for the equipment, enabling to keep the incomplete overlap region to the smallest distance by keeping the emitted laser contained within FOV. It also keeps the obscured or shadowed region due to the secondary mirror to a minimum, aiding our intention to reduce the nearest useable measurement range. However, as the instrument's optical SNR is inversely proportional to the field-of-view (FOV) (Hey, 2015), hence the aperture size deciding the field of view has to maintain an adequate ratio between the overlap region with the emitted pulse and the unwanted background noise, which is collected from outside our region of interest, else the SNR value diminishes.

Furthermore, the Newtonian telescope was selected because it has a minimum number of optics (only primary and secondary mirror), resulting in the least amount of signal loss during transmission from any additional optics and maintaining minimum aberration, hence enhances the signal-collecting efficiency. The telescope also does not have any filter, collecting all the received signal, not only making it cost-effective further makes the system flexible for carrying out other measurements of interest using different wavelength laser pulses.

2. Photomultiplier Tube (PMT)

The photomultiplier tube (PMT) is a photosensitive detector that converts a light pulse into an electrical signal of measurable magnitude. The HAMAMATSU R5108 PMT was chosen for the MSL to detect the backscattered signal for its reliable high signal to noise ratio and relatively large active area.

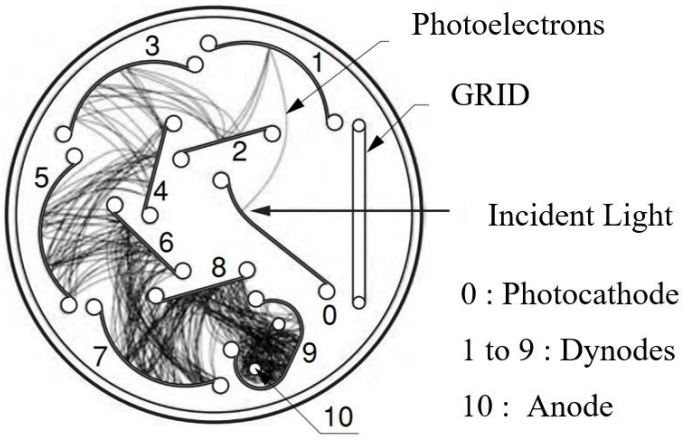

Fig. 21. Structural elements of a circular cage PMT depicting the 9 stage electron amplification effect (Hamamatsu, 2007)

The device comprises a vacuum tube with an input widow, a photocathode, and focusing electrodes, an electron multiplier, and an anode. The received backscattered signal enters through the input window of the tube. This intern stimulates the photocathode's electrons so that the photoelectrons are emitted into the vacuum (external photoelectric effect). Photoelectrons are accelerated and directed by the focusing electrode toward the first dynode, where they are multiplied utilizing secondary emission. The secondary emission is reproduced at each of the succeeding dynodes and cascading the amplification of electrons. The anode finally accumulates the multiplied secondary electrons discharged from the last dynodes (Hamamatsu, 2007).

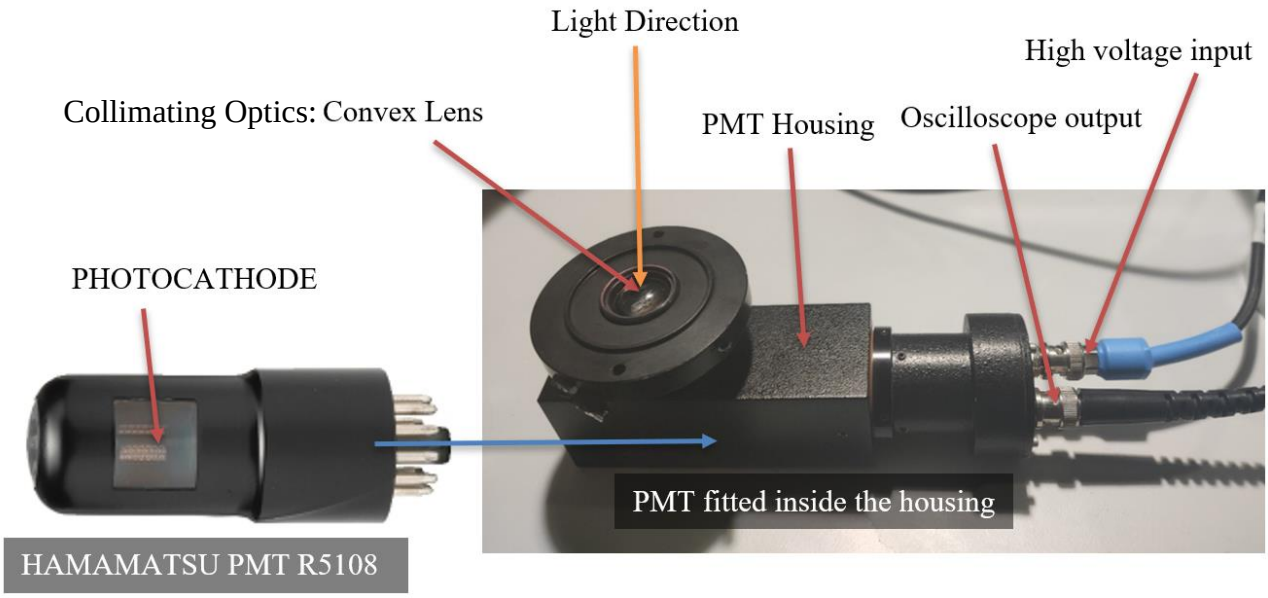

HAMAMATSU PMT R5108 Specifications

Design	Photocathode, side-on Type
Spectral Response	400 to 1200 nm
Photocathode Material	Ag-O-Cs
Photocathode Minimum Area (H × W)	16mm × 18mm
Dynode structure	Circular cage, 9 stages
Operating and storage ambient temperature	-30°C to + 50°C
Supply voltage between Anode and Cathode	1500 V

Supply voltage between Anode and Last Dynode	250 V
Anode Pulse Rise Time	1.1 ns
Electron Transit Time	17 ns

3. Optical Bandpass Filter

An optical bandpass filter is placed in front of the PMT optics to restrict the amount of undesired radiation, notably reducing noise by only allowing the light of the wavelength of interest to pass. More importantly, it prevents the intense background light from damaging the detector PMT sensor, enabling the use of the MSL in an illuminated environment, such as in the presence of sunlight.

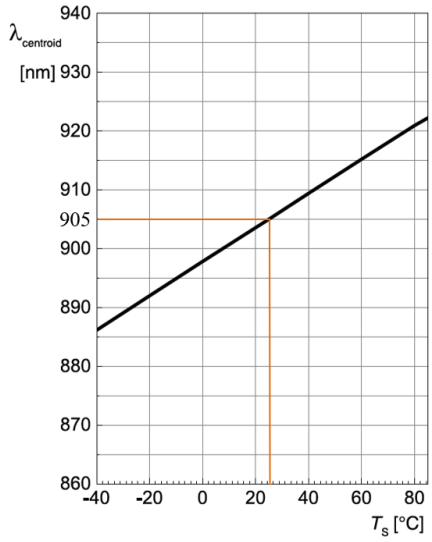

$\lambda_{centroid}$ = f(Ts);

Forward current = 40 A

Pulse width = 100 ns

Duty cycle = 0.01 %

Fig. 22. SPL UL90AT08 laser diode centroid wavelength variation with temperature (OSRAM, 2019)

Prior to choosing the bandpass filter specifications for the MSL, consideration has been made for the drift in the centre wavelength with temperature change (fig.22.) of the emitting laser and also the bandpass filter (typical thermal shift of the centre wavelength for the filter is 0.015 to 0.025 nm/°C) . This drift occurs mainly due to the minute thermal expansion or contraction of the layers of the semiconductor laser diode and the layers in the bandpass filter structure. Though a resistive heating arrangement can be installed aiming to maintain an optimum temperature of about 23 - 25°C, there will still be inconstancy during field measurements, especially in a marine environment. Therefore, a wide bandpass filter is appropriate for our

application. However, at the same time, it has to be reasonable else the increase in background noise will significantly reduce the SNR.

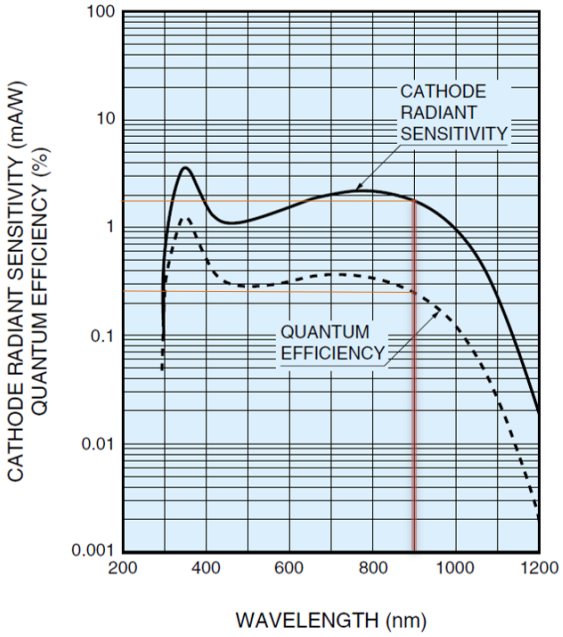

Fig. 23. Typical spectral response of PMT R5108(Hamamatsu, 2003)

Besides, the spectral range of our PMT detector, which is ~ 400 to1200 nm, (fig.23.) has also been recognised. The background noise is suppressed as much as practicable, and the detector is not damaged in the presence of uncontrolled illumination during field measurements.

After considering the above discussed parameters, the FL905-25 Optical Bandpass Filter was chosen for the MSL.

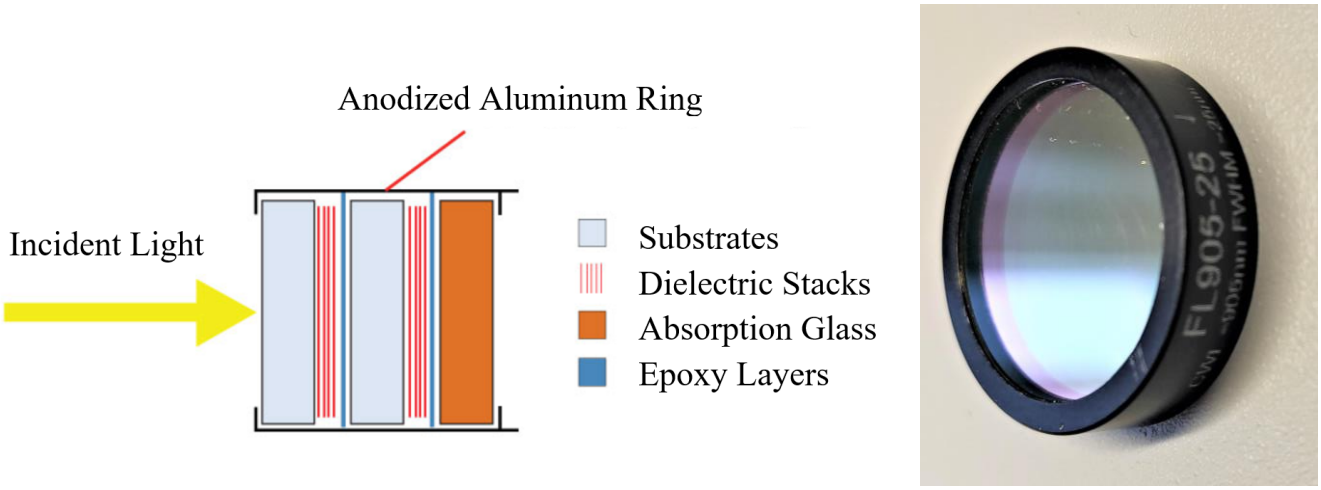

Fig. 24. Layered structure of the FL905-25 Optical Bandpass Filter(Thorlabs, 2012)

FL905-25 Optical Bandpass Filter Specifications at 23 °C

Filter center wavelength at normal incidence	905 ± 5 nm
Filter FWHM	25 ± 5 nm
Blocking Range	200 - 1280 nm
Minimum Transmission at Center Wavelength	70%
Typical Thermal Shift	0.015 to 0.025 nm/°C
Operating Temperature	-50°C to + 80°C

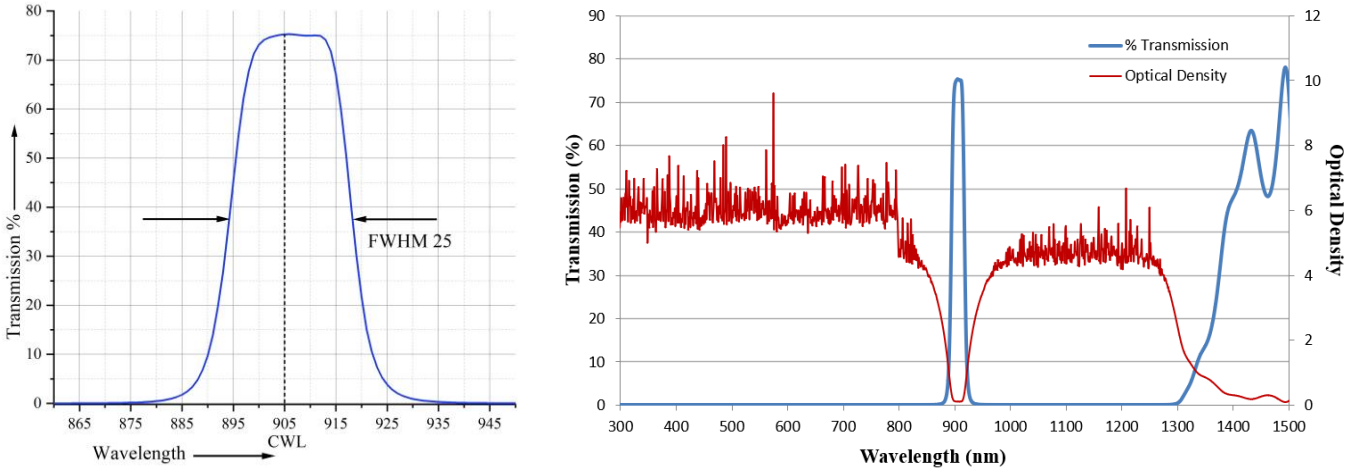

Fig. 25. Transmission and optical density Vs wavelength of the FL905-25 Optical Bandpass Filter(Data from Thorlabs)

The relatively wide FWHM of 25 nm(fig.25.) can reasonably compensate for the wavelength shift of the laser. Also, the blocking range of the filter is about 200 to 1300 nm(fig.25.), which adequately protects the PMT from damage due to uncontrolled illumination as its response range (~400 to 1200 nm) lies within it.

3.1.3 Output and Data Acquisition

Prior to assembling the different components to build the MSL, initial tests (fig.26.) were conducted to check their performances inside a black box, blocking stray background lights from entering the setup as much as possible.

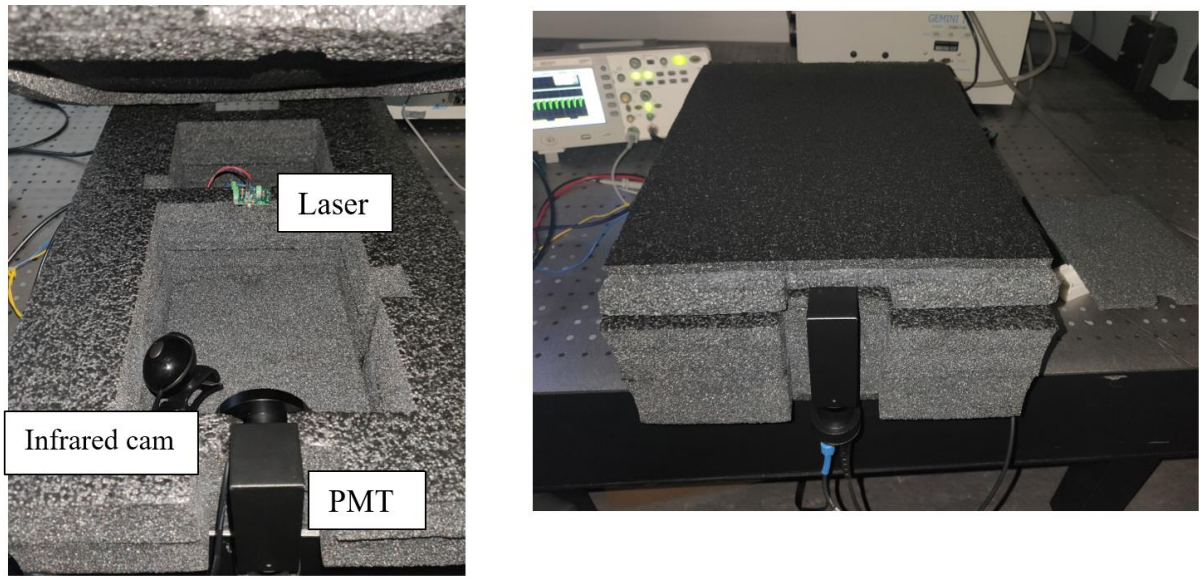

Fig. 26. Initial setup for checking component performance

During most part of our experiment, a 200 Mhz bandwidth 2 GSa/s sampling rate oscilloscope (DSO1022A) was available to us, and we used it to read and store the output from the PMT for further analysis. At times we had access to a higher 500 Mhz bandwidth 5 GSa/s sampling rate oscilloscope (MSOX4054A). But with both the oscilloscopes, we had a limitation to store the data for further interpretation. Even with the MSOX4054A, which had a segmented memory option, let us store data of a maximum of 1000 segments with 640 points per segment, which means at a 1kHz laser pulsing frequency, we can only acquire data of 1 second(1000 milliseconds). This barrier prevented us from analyzing longer range and period of data and carrying out a further inversion technique to retrieve optical properties from spray measurements. A better data acquisition and storage arrangement is required for continuing further with this project.

3.2 MarSpray LiDAR (MSL) Opto-mechanical Architecture

A conventional atmospheric LiDAR is mainly designed for carrying out far range measurements and hence transmit high power laser and have a large telescope aperture. For carrying out sea spray analysis on ships, the ability for near-range measurement with a high spatial and temporal resolution is essential.

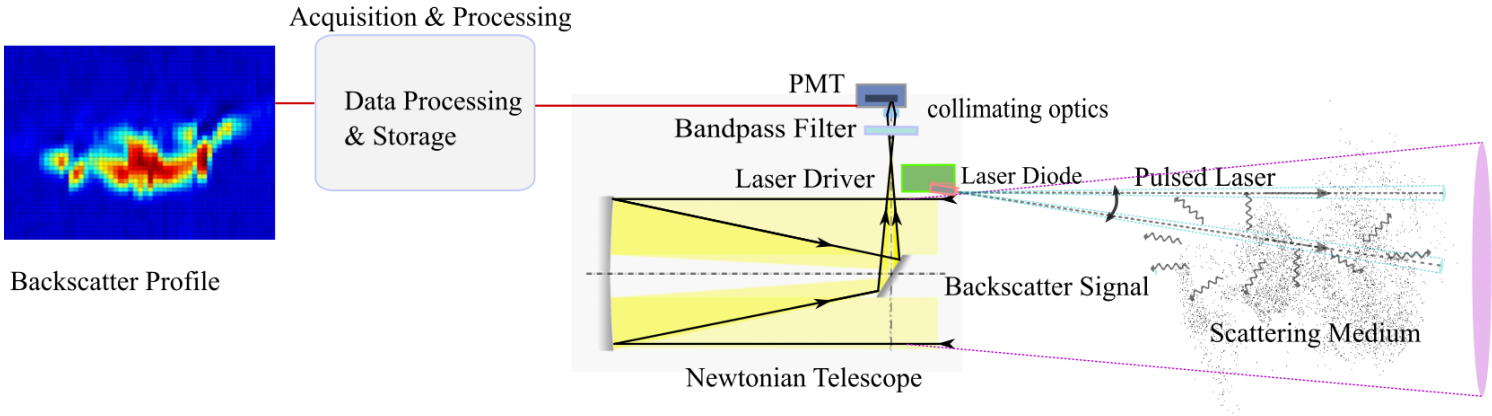

Fig. 27. Illustration of the MarSpray LiDAR (MSL) Layout

A significant obstacle causing measurement uncertainty for conducting near-range analyses with elastic backscatter LiDAR is due to the incomplete overlap (discussed in section 2.3.3) between the transmitted pulsed laser and the LiDAR receiver. **Mono-static multi-axial configuration** design was decided for the MSL, which was inspired by viewing the performance of the Colibri micro-lidar (Ceolato et al., 2020), which is a bi-static multi-axial elastic backscatter LiDAR designed for quantitative profiling of aerosols at a short range. The multi-axial design seemed appropriate for maintaining a minimum incomplete overlap zone, and the mono-static design makes the equipment mobile and compact, suitable for carrying out sea spray measurements in medium-sized to bigger vessels.

3.2.1 MSL mono-static multi-axial configuration

A mono-static configuration states that the emitter and the receiver are in one location, and multi-axial means can adjust the respective position between the beam and the telescope's axes. The different components of the LiDAR discussed above were assembled and fitted using various 3D printed parts to build this configuration. We used Autodesk Inventor® for designing

and "Pro2 Dual Extruder" 3D Printer for printing the different parts according to our requirement with high precision.

Fig. 28. Printing segments for assembling the components for the MSL

i) Bandpass Filter fitting

The bandpass filter was fitted in front of the convex lens placed on the PMT housing, protecting the photocathode from overexposure and permitting only the wavelength of interest (~905nm) from getting detected.

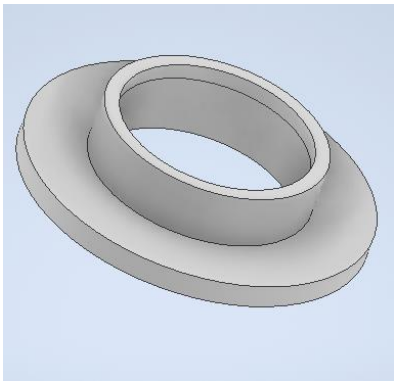

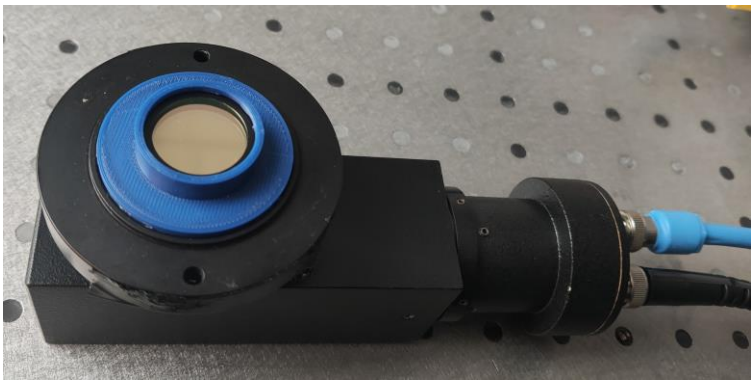

Fig. 29. Bandwidth filter fitted on the PMT housing

ii) Photomultiplier Tube (PMT) fitting

A segment was designed to fit the PMT receiver near the telescope's focus as much as possible so that most of the received signal is concentrated to the PMT's detection window. The dimensions of the printed segment had to match around the telescope's body precisely so that its drawtube ends near the window of the PMT, such that only signal from the region of interest enter and no stray lights from gaps.

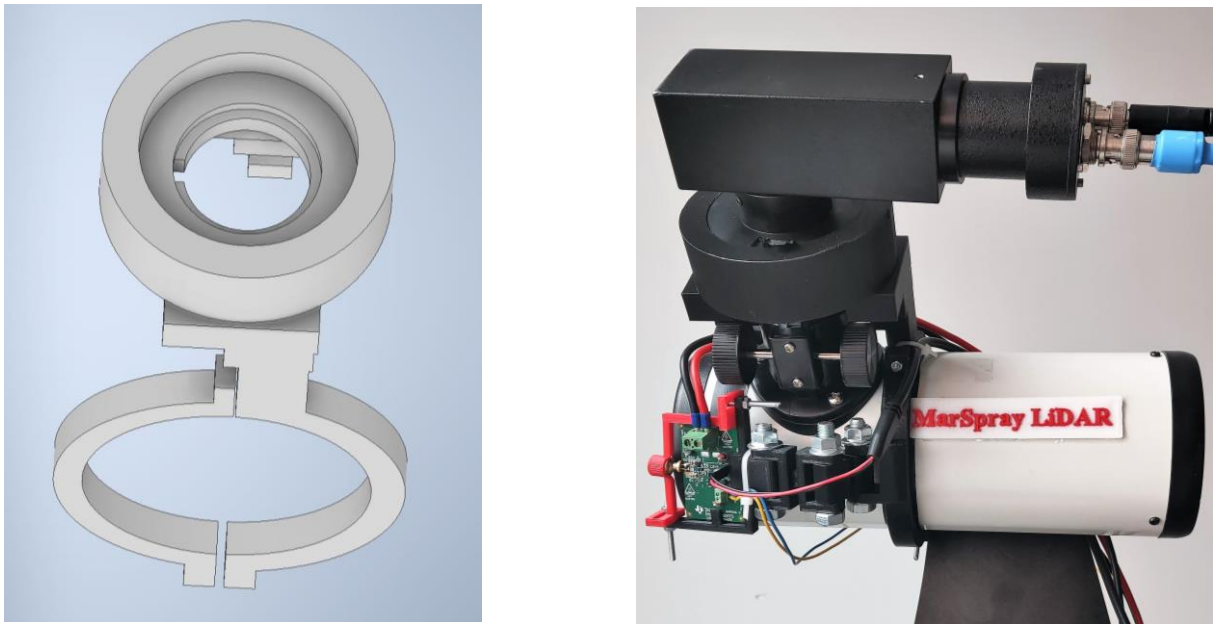

Fig. 30. PMT fitted at the termination of the eyepiece barrel close to the telecope focal length

MSL Field of view (FOV)

The field-of-view (FOV) of the LiDAR equipment is expressed as the angle covered by its receiver, or the sensor is effective. It can be analytically derived from the effective aperture of the receiver, which can be retrieved from the telescope and the sensor specifications provided. However, for the MSL, we had to modify the receiver optics, especially the convex lens (sensor collimation lens) arrangement combined with an optical bandpass filter fitted in front of the PMT to collect the photons received and focus on the photocathode, which intern varies the angular response of the sensor. Hence, we applied an experimental approach to confirm the effective FOV of the sensor, which also accounts for its detection efficiency.

Calculation

Fig. 31. Experimental setup to confirm the sensor FOV for the MSL

The receiver telescope was placed at a distance of 195 cm in front of a perpendicular screen (fig.31.). A laser of wavelength within the photomultiplier tube (PMT) response spectrum was focused on the screen and slowly moved within the PMT detection region. As soon as the PMT detected the signal, a visible change occurred in the received voltage in the oscilloscope reading, and the point was marked on the screen. Following this, we continued to move the laser image on the screen. Gradually after a certain distance, the detector stopped responding, and the voltage reading returned to the initial on the oscilloscope when the laser moved out of its detection range, marking another point on the screen. Repeated this process, adjusting the laser path on the screen to make sure we are accounting for the detection region's diameter and not a chord.

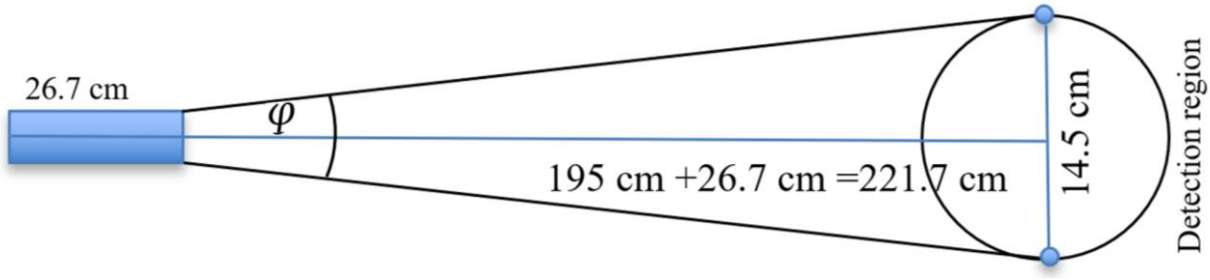

The field of view (FOV) of the MSL (φ) :

$2 \times tan^{-1}\left(\frac{14.5/2}{221.7}\right) = 3.75° = 65.45\text{mrad}$

The field of view is quite large, favoring short-range measurement but at the same time will contribute towards gathering noise reducing the SNR; this can be reduced using an iris arrangement according to our application while field deployment of the MSL.

iii) Collimation lens fitting

The laser collimating lens was fitted in front of the laser diode such that it is a focal length away. Provisions were made in the designed segment to make fine adjustments possible, so that the laser beam can be appropriately focused.

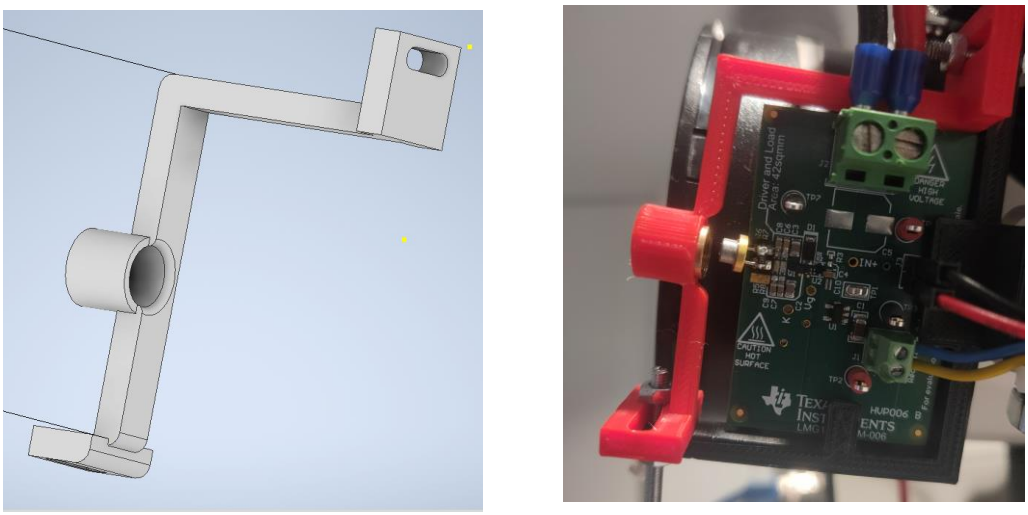

Fig. 32. Collimating lens fitted in front of the diode

The infrared detection card was fair for checking the beam quality at a short but couldn't confirm the quality at a more extended range. To tackle this issue, we used a webcam and transformed it to detect infrared light by removing its IR filter (fig.33.). This helped us to visualize the collimation quality at further distances and also for calculating the laser beam divergence after collimation.

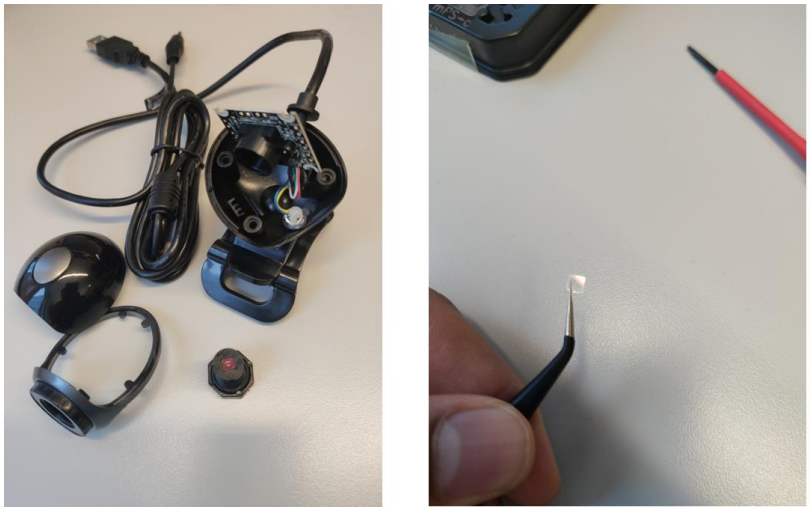

Fig. 33. Transforming the webcam to an IR camera and using to visualize the collimation

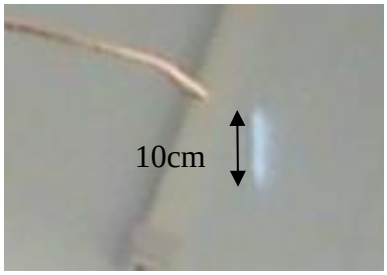

The laser beam at a distance of 375cm (pictured with the infrared cam)

Beam divergence(δ):

$$2 \times tan^{-1}\left(\frac{10/2}{375}\right) = 1.5° = 26.18 \text{ mrad}$$

The beam divergence (δ) after collimation perpendicular to pn-junction (fast axis) was found approximately 1.5° which is lesser than the FOV (3.75°) of the receiver unit.

iv) Laser fitting

For achieving the mono-static configuration, the laser emitter needs to be in the same place as the receiver, and for multi-axial, the axis of the laser beam about the axis of the telescope requires provision for adjustments. To attain this, the 3D printed segment was designed to house the laser driver (as the laser diode was soldered directly on the driver) and the 3-piece attachment allowing for adjusting its axis. The attachment was made as rigid as possible, but a slight change in this axis changes the overlap function of the MSL; hence calibration is recommended every time before use.

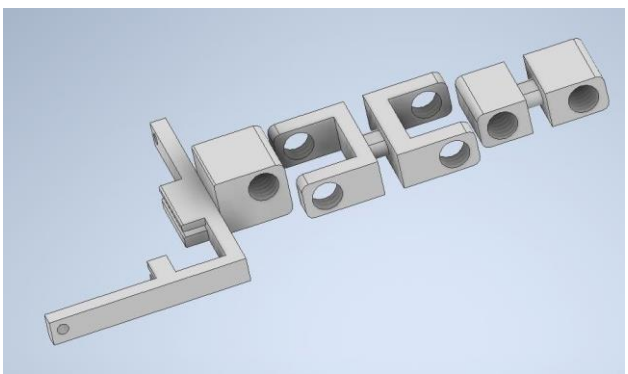

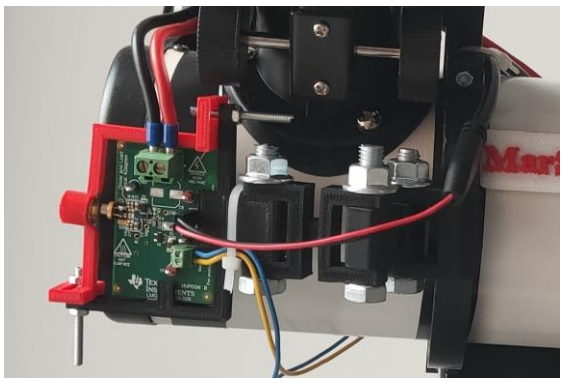

Fig. 34. Collimating lens fitted in front of the diode

*Prior to field deployment of the MSL, a protective box with resistive heating is suggested to be fitted, covering the laser diode and the driver to prevent center wavelength shift of the laser with the temperature change and to shield the electronics.

v) Assembling and mounting

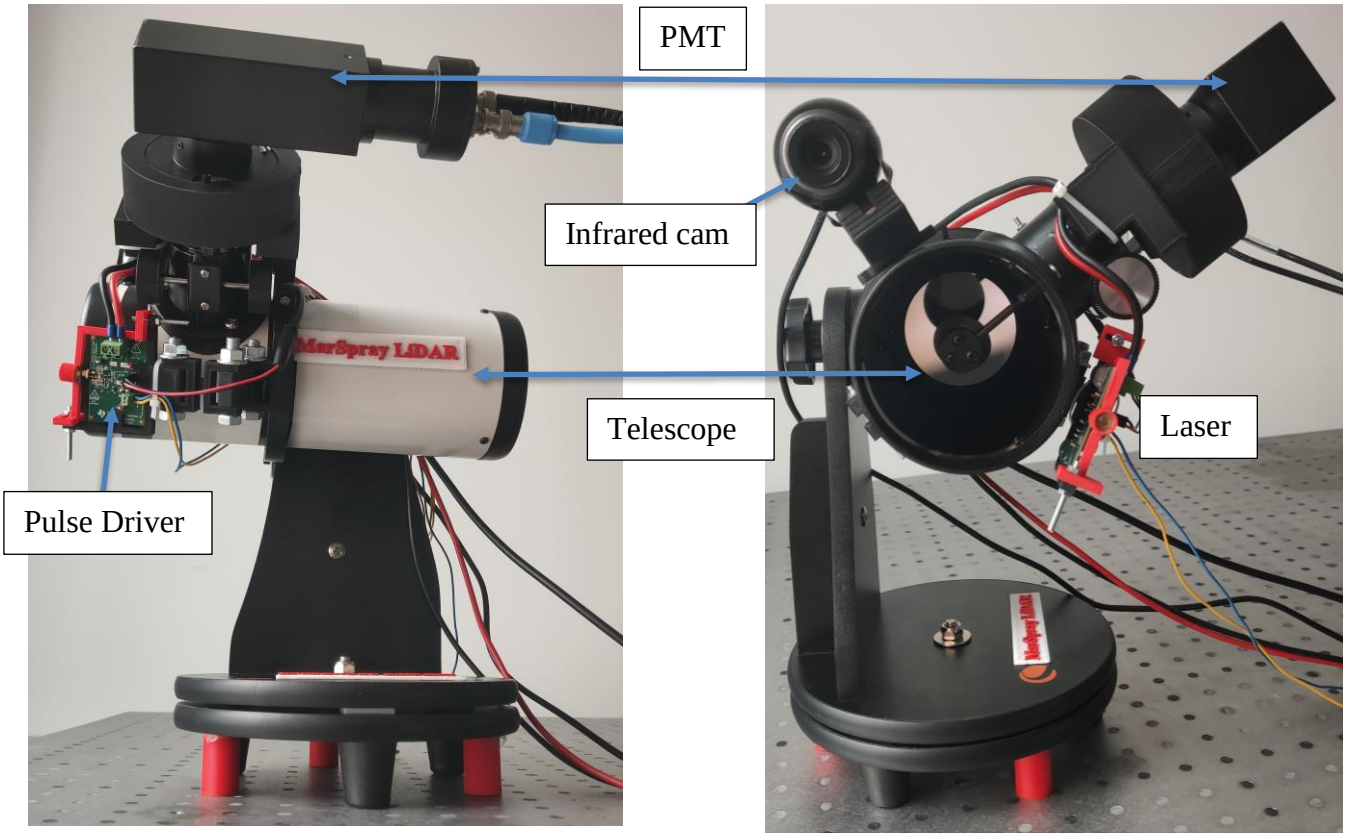

Fig. 35. The MarSpray LiDAR(MSL) final configuration

After printing the various segments, we fitted and assembled the different components to achieve the MSL's final monostatic multi-axial design (fig.35.). Also, the previously transformed infrared cam was fitted on the MSL, swivelling with the direction of the emitted laser, which helped us during measurements to visualise if the laser is focused correctly in our region of interest.

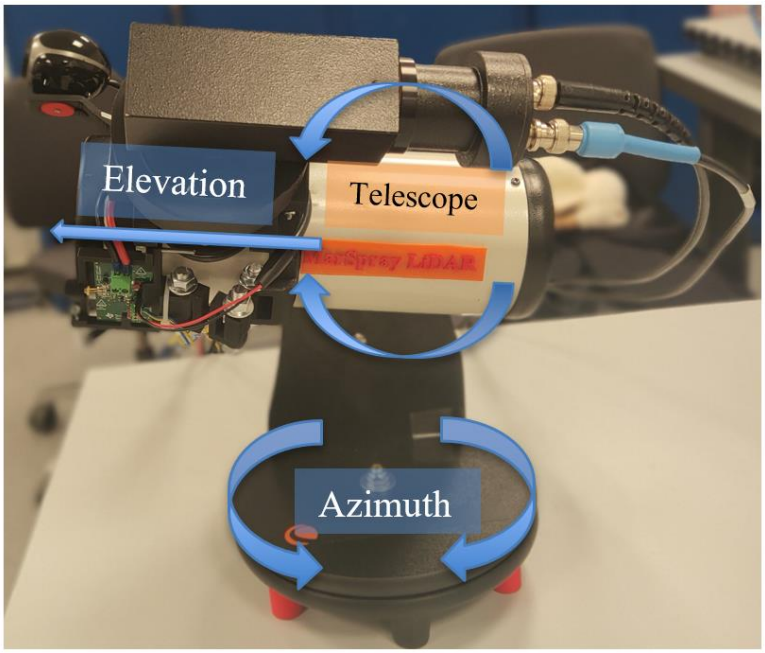

Fig. 36. MSL mounted on a Dobsonian stand

The MSL is mounted on a Dobsonian stand (fig.36.) which is an alt-azimuth mount. It is a mount supporting and pivoting the MSL about vertical and horizontal axes. Pivoting about the vertical axis adjusts the azimuth of the laser and telescope pointing direction and pivoting about the horizontal axis adjusts the angle of elevation. The stand provides a stable configuration which enables safe repositioning of the equipment and makes it easy to point in the direction of interest.

3.2.2 MarSpray LiDAR (MSL) Overlap Calculation

Reliable knowledge about the range at which complete overlap is first reached is important for close range measurements; to establish a minimum range from which to implement signal inversion.

Several researchers have proposed analytical methods (Comeron et al., 2011; Halldórsson and Langerholc, 1978; Kumar and Rocadenbosch, 2013; Stelmaszczyk et al., 2005) or empirical methods (Hey, 2015; Wandinger and Ansmann, 2002) for modifying the overlap function. For our design, we applied Stelmaszczyk et al. (2005) analytical model for finding the distance after which there is complete overlap.

Geometric calculation

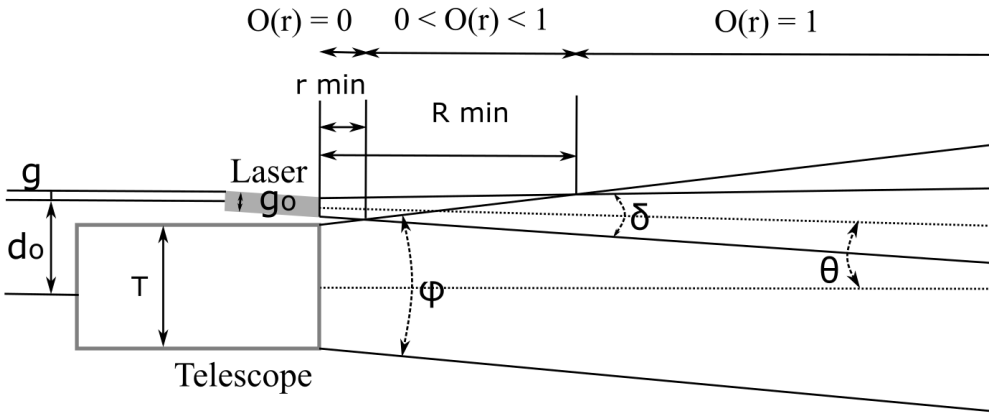

Fig. 37. MSL Transmitter Receiver geomtery

In fig.37. d_o is the distance separating the laser transmitter and receiver centres; g_0 is the laser beam diameter at output; T is the telescope primary mirror diameter; φ is the receiver FOV; δ is the laser divergence, θ is the angle between receiver and transmitter axes (it can be adjusted in the MSL, hence the overlap function depends on this allignment). R_{min} and r_{min} is defined as the limits of the range interval of incomplete overlap between the laser beam and the receiver FOV.

$$R_{min} = \left(\frac{T}{2} + d_o + g\right)\frac{\cos\left(\frac{\varphi}{2}\right)}{\sin\left(\theta + \frac{\varphi}{2} - \frac{\delta}{2}\right)} \sin\left(\frac{\pi}{2} - \theta + \frac{\delta}{2}\right) \qquad \text{Equation 17}$$

Stelmaszczyk et al. (2005) applied geometrical approach for calculating the full-overlap distance(equation 17).

An evaluation of the range (R_{min}) beyond which the overlap function value is free from geometrical compression is carried using equation 17, inputting the MSL's component parameters.

MSL Parameters:

$d_o \approx (96/2 + 10) = 58$ mm = 0.058 m

$g \approx g_o/2 \approx 110\ \mu m = 110 \times 10^{-6}$ m

T ≈ 76 mm = 0.076 m

$\theta \approx 3° = 52.36$ mrad

$\varphi \approx 3.75° = 65.45$ mrad (from section 3.2)

$\delta \approx 1.5° = 26.18$ mrad (from section 3.3)

from equation 17, $R_{min} \approx 1.34$ m

Validation

The overlap function is very susceptible to all of the above parameters and presumptions and to the exactness of the associated angles and seldom known precisely; hence experimental validation is required to verify the accuracy (Kovalev and Eichinger, 2004). A Lambertian surface of calibrated reflectance (MicaSense, RP04-1814005-SC, fig.38.) was used to carry out lidar measurements, starting from close to the equipment then gradually increasing the distance(fig.39.). The range corrected measurement change is recorded over different distances.

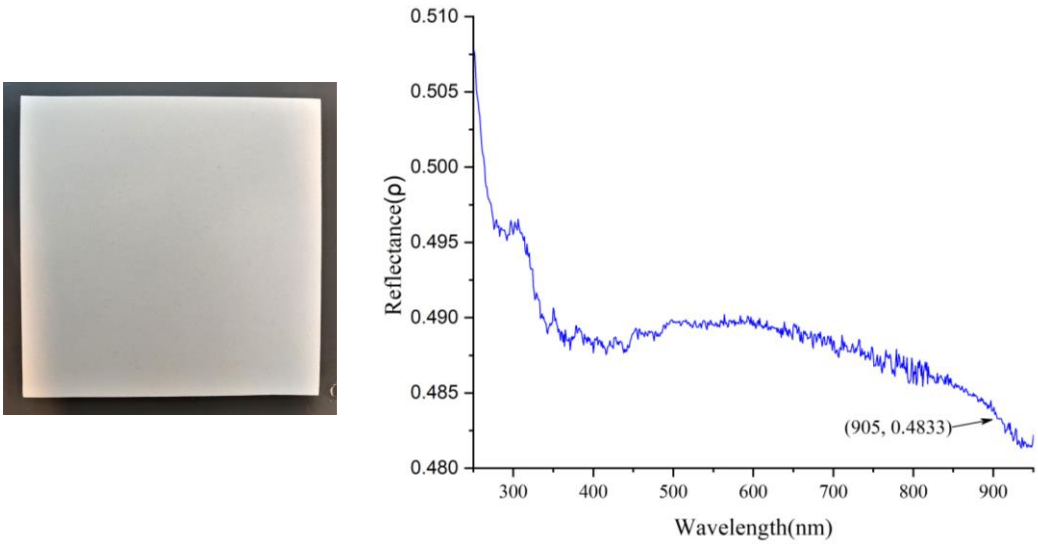

Fig. 38. The Calibrated Reflectance Panel(MicaSense, RP04-1814005-SC) and its reflectance values across the light spectrum(graph plotted from the data provided by MicaSense)

Fig. 39. Diffused reflection of the laser beam on the Lambertian surface, checking the measurement values at various distances (pictured with the infrared cam)

After a distance of 1.4 m, no significant difference in the range corrected reading (r^{-2}) was witnessed; that is when the full-overlap (R_{min}) between the laser beam and receiver FOV occurs. It reasonably matches the value obtained from the analytical method.

This method for validation was adopted from Ceolato et al., 2020, Colibri micro-lidar. This method's advantage based on known reflectance surfaces is that it does not depend on the typical approach of using assumed homogeneous atmosphere at a far distance used for evaluating the overlap function.

The overlap function value is taken as 1 for measurements being carried out beyond 1.4 m (possible to adjust this value by changing the axis). This small value of incomplete overlap zone satisfies our intention for near range analysis suited for being used in medium-sized to bigger vessels.

4 Result and Analysis

4.1 MSL Specifications

The relation between the pulse width and the distance resolution is that the shorter the pulse width, the smaller or better is the distance resolution by which a spray can be profiled. The pulse repetition rate determines the time resolution, the interval at which the spray can be measured. Hence the efficiency of the MSL depends on the pulse width and its repetition rate. Generating and measuring the shortest possible pulse width was probably the most challenging part of this project. The claimed 1 ns pulse driver had sequential obstacles due to impedance mismatching leading to ringing from the diode output, which had to be adjusted before getting a suitable output. Another barrier for carrying out analysis was the associated PMT's electrical noise. Also, due to the lower sampling rate of our oscilloscope added some uncertainty in the measurement, unable to represent the definite shape of the output.

For graphing, data analysis and post signal processing, we used Origin® and MATLAB® software. At times the PMT reading attenuates due to the noise and interferences, such as background noise, dark current, and electronics readout noise. We applied the adjacent-averaging technique for denoising the lidar signal to improve the SNR. In the future, the signal processing method can be enhanced further by introducing a deep-learning-based algorithm to eliminate repetitive noise for obtaining better results.

1. Pulse Width

For a pulsed laser emitting bursts of light spaced in time, the pulse width is the optical pulse duration, and the time is measured across a pulse between its beginning and end, usually at its full width half maximum (FWHM).

Setup and input settings to generate the shortest laser pulses possible with our present arrangement:

(i) SPL UL90AT08 Laser diode
(ii) TIDA-01573 Laser driver with an input voltage (VBUS) 10 V, bias voltage 5.5 V and 85

ns pulse width trigger @ 1kHz (PRF) from the waveform generator.

(iii) R5108 Photomultiplier tube

(iv) DSO1022A Oscilloscope

Typically, a Pulse width (FWHM) ~ 3 ns (fig.40.) was detected. A Gaussian fit was made because the Gaussian decomposition approach considers that the Gaussian function can model a LiDAR pulse (Hofton et al., 2000).

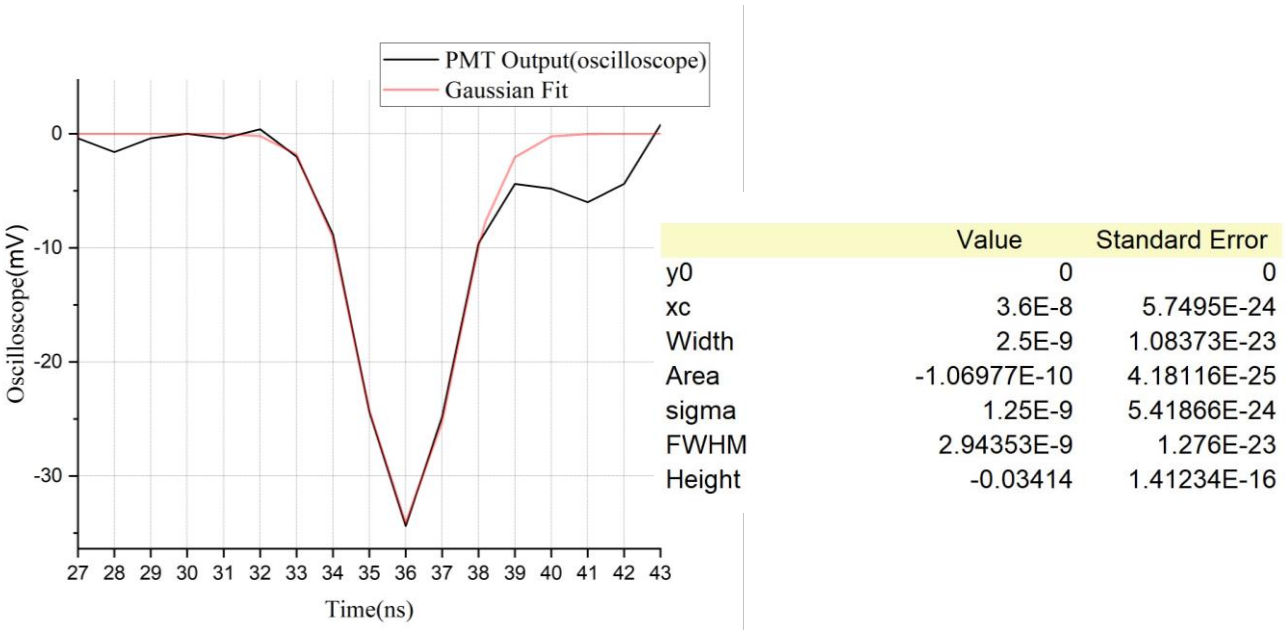

	Value	Standard Error
y0	0	0
xc	3.6E-8	5.7495E-24
Width	2.5E-9	1.08373E-23
Area	-1.06977E-10	4.18116E-25
sigma	1.25E-9	5.41866E-24
FWHM	2.94353E-9	1.276E-23
Height	-0.03414	1.41234E-16

Fig. 40. Representing a typical pulse return from a solid target

For practical purposes, giving room for an error of 1ns, which may arise from an error in the calculation due uncertainties and noise in the measurement data, we considered the pulse width as 4ns.

$$\text{Dectected Pulse width } (\tau_P) = \tau_L + \tau_N + \tau_w = 2 + 2 + 0 \text{ ns} = 4 \text{ ns}$$

τ_L is the emitted laser pulse duration dependent on the laser diode, the laser driver and the waveform generator input, τ_N is the time constant of the detecting electronics (accounting for the PMT response rise and fall time + signal transmission time through the cables + oscilloscope response time), and τ_w the reaction time of the interaction of laser light with particles, which is almost negligible.

* The laser diode stability with time, ambient temperature, among other uncertainties, contribute to the fluctuation in τ_L and τ_N, further adding to the variation in pulse width and subsequent measurements. Hence, calibration is recommended each time prior to using the MSL for analyses.

2. Distance Resolution

Distance or range resolution (ΔR) of a pulsed system is the time (distance) required for backscattered light from the beginning of the pulse to reach the forward-propagating light from the end of the pulse (Hey, 2015).

Theoretically for a 4ns pulse we should have a distance resolution (ΔR) of:

$$\Delta R = \frac{\tau_P \times c}{2} = \frac{4\ \text{ns} \times 30\ \text{cm/ns}}{2} = 60\ \text{cm}$$

Where, (τ_P) is the pulse width and speed of light(c) ~ 30 cm/ns

Experimental setup for affirming the distance resolution:

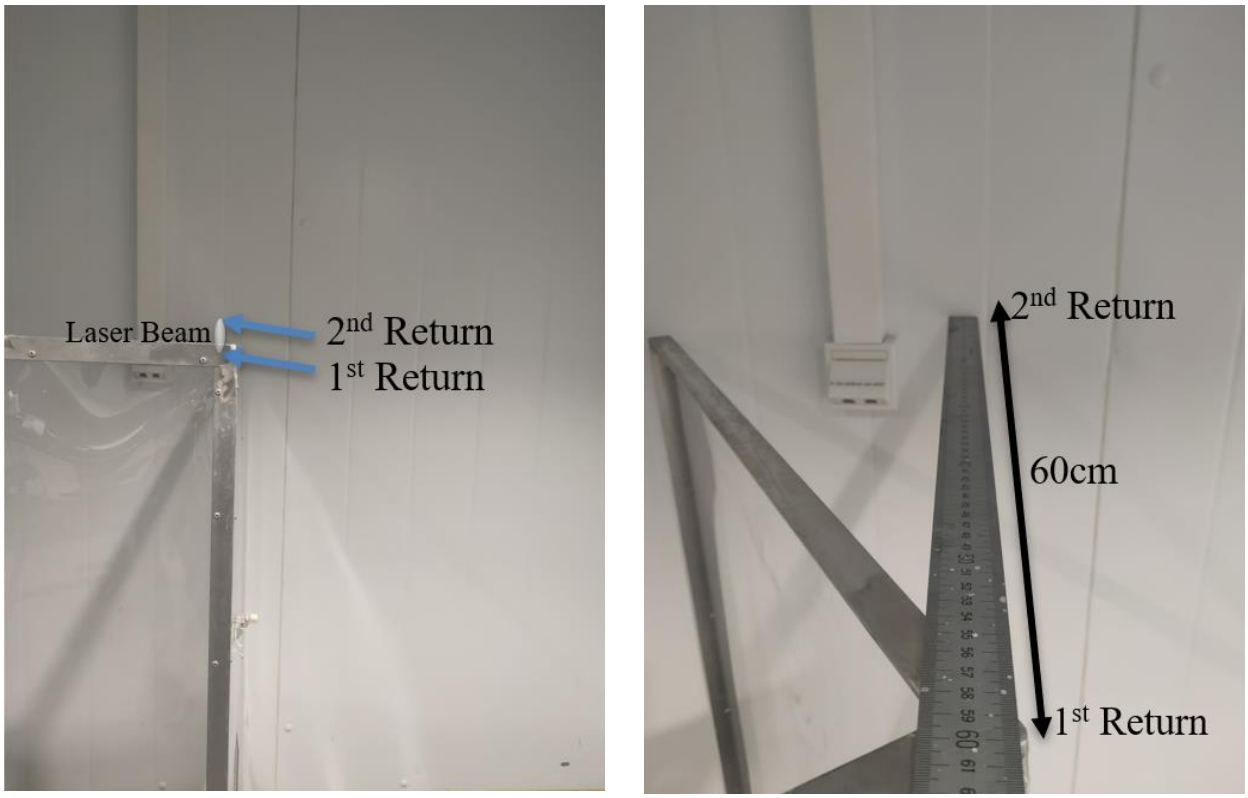

Fig. 41. Arrangement for measuring the distance resolution

A solid obstruction was placed 60 cm in front of the wall. The laser beam from the MSL was directed such that a part of the beam falls on the obstruction, and the rest falls on the wall (Fig.41). This arrangement was to ensure that the first return should be from the obstruction and then the second return from the wall.

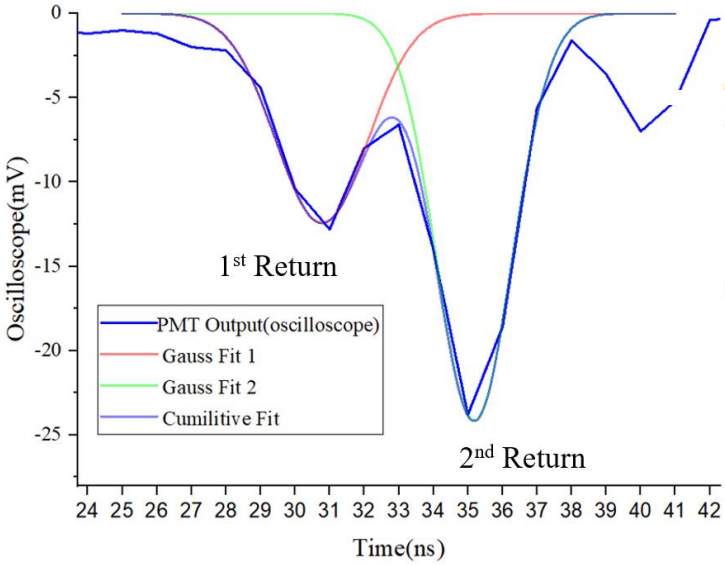

		Value	Standard Error
1st Return	y0*	0	0
	Xc(1st)	31	3.24754E-10
	width	2.66306E-9	7.05308E-10
	Area	-4.14949E-11	9.08946E-12
	sigma	1.33153E-9	3.52654E-10
	FWHM	3.13551E-9	8.30436E-10
	Height*	-0.01243	0.00242
2nd Return	y0	0	0
	Xc(2nd)	35	1.53621E-10
	width	2.19302E-9	3.21702E-10
	Area	-6.63234E-11	8.36022E-12
	sigma	1.09651E-9	1.60851E-10
	FWHM	2.58209E-9	3.78776E-10
	Height*	-0.02413	0.00262

Fig. 42. Distance resolution measurement

By analyzing the LiDAR reading we can see the presence of two maxima after 31 ns and 35 ns (fig. 42.). Difference between the return peaks, Xc(2^{nd} return) - Xc(1^{st} return) = 4 ns

Hence, we can see with a pulse width or duration of 4 ns makes it possible to identify targets separated by 60cm.

3. Time Resolution

The time resolution depends on the frequency with which the laser is pulsed. The frequency can be controlled by varying the trigger input from the function generator to the laser driver. Our laser driver is rated for a switching frequency of a maximum 1MHz, and the laser diode has a maximum duty cycle of 0.1%. We used 1 kHz laser pulse frequency for our measurements, giving a time resolution of 1ms, which is in the safe region of our laser diode duty cycle.

4. Time of Flight (TOF)

The "Time-of-flight" technique applied to resolve the distance between the LiDAR equipment and the scattering particle by timing the round-trip time of the pulsed laser.

Initially, we utilized this technique for back-calculation to obtain the system time delay to find the delay between the trigger generated by the function generator and when the pulsed is actually fired from the laser diode. Then can use this value to find the distance of the target.

Back calculation:

When we have trigger input of 85 ns from the function generator to the laser driver, we generate ~4 ns pulses (section 4.1.1). The same trigger (by using a BNC splitter cable) was also entered in the Oscilloscope CH1. The Oscilloscope CH2 had another input from the PMT output.

Then the MSL was placed in front of a target of known (measured with a measuring tape) distance d = 375 cm

From, fig. 43. The actual Time delay after the function generator triggers and the Oscilloscope reads the PMT output = 139 ns

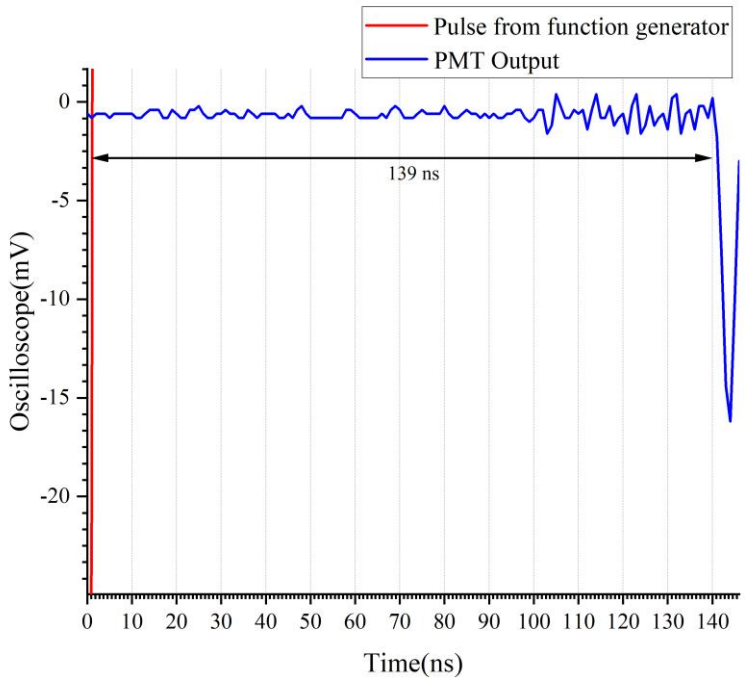

Fig. 43. Pulse return from a known distance of 3.75 m

Theoretical TOF required for a 375cm distance (without any delay) = $\frac{2\times d}{c} \approx \frac{2\times 375}{30} \approx 25$ ns

Therefore, the time delay between the time when a pulse is triggered by the function generator and the laser is fired = 139 ns – 25ns = **114 ns**. This value includes delay after which the pulse

is fired + time constant of the detecting electronics (PMT response time + Transmission time through the cables + Oscilloscope response time).

For the following measurements, subtracting this value from the PMT response time of a pulse return from a target, we get the actual TOF and subsequently obtain the target distance.

*There are various methods recommended to find the "time of flight" technique to find the delay when the pulse is fired and when detected. Most of this technique requires adding extra hardware, such as adding a beam splitter, which will reduce the emitted pulse's energy or adding an additional connection from the laser driver gate output to the oscilloscope, not only will make our circuit complicated but will add to the impedance mismatching problem. Hence our technique was advantageous as it didn't require adding any extra hardware. It also incorporates the delays such as PMT response time, transmission time through the cables and oscilloscope response time, thus making TOF calculation simpler.

4.2 Spray Measurement

Initial spray measurement was conducted to evaluate the performance of the MSL as proof of our concept for profiling spray. Measurements were carried out in the cold room (fig.44.) in the UiT Technology building. This room was chosen as it had a good drainage system required for removing the water from the generated sprays. Also, the lighting and the temperature conditions inside the room could be maintained appropriately and had adequate power connections. The drawback was the room's small dimension restricting us from checking MSL's performance at a more extended range.

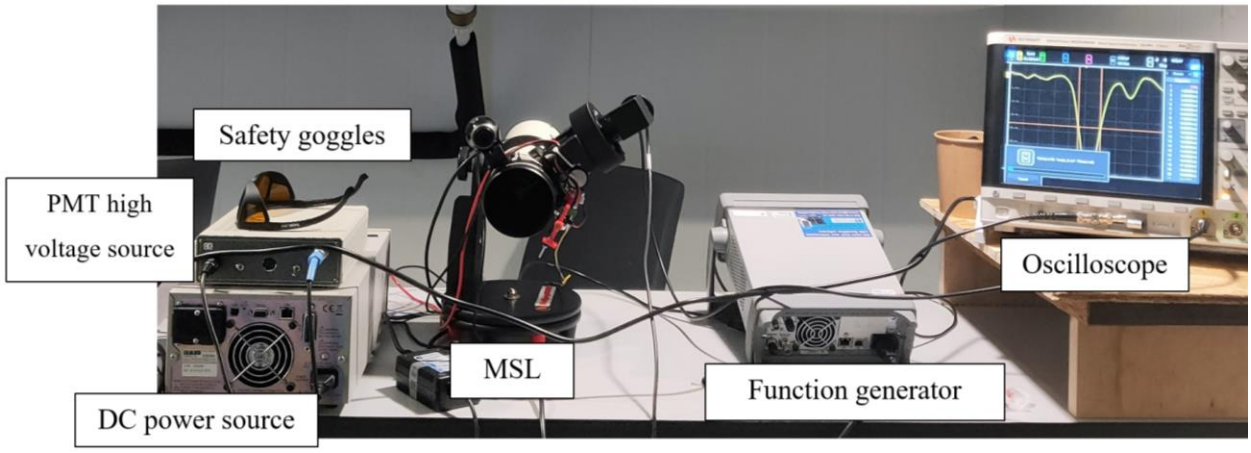

Fig. 44. MSL setup in the cold room

The MSL spray measurement was performed horizontally, as illustrated in Fig.46. A water sprayer nozzle was used to generate spray droplets and was placed in front of a surface reference target (SRT) (Fig. 45). The spray measurement is performed in the full-overlap region of the MSL i.e. beyond 1.4 m. This arrangement of using the SRT for performing lidar inversion is appropriate for short range LiDARs described by Gaudfrin et al. 2020 (appendix), which we intend to use in our future work. MicaSense RP04-1814005-SC, a Lambertian Zenithal Surface with known reflectance fr=0.48, was used as the SRT. The mean orientation of the laser beam was kept parallel to the normal of the SRT, and its pulsing frequency was set to 1KHz.

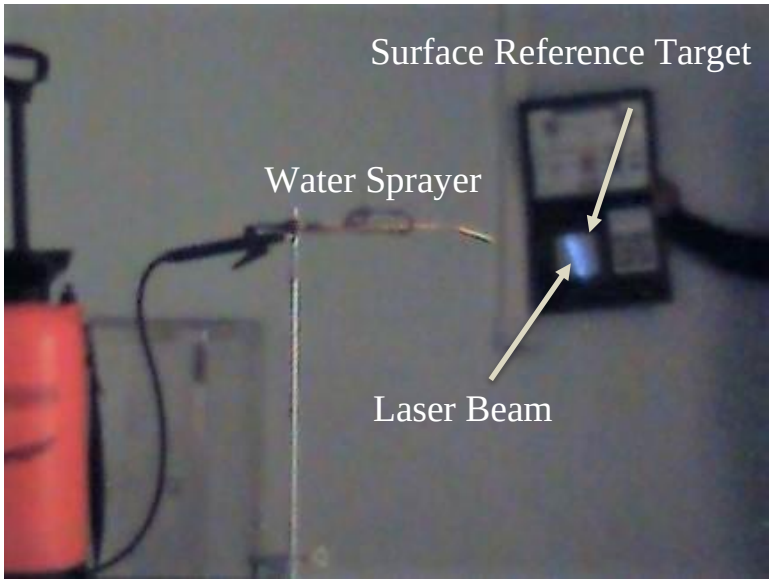

Fig. 45. Spray measurement setup (pictured with the infrared cam)

Steps:

1. **The first measurement** is made by occulting the emitting laser beam to estimate the contribution of background illumination.

2. **The second measurement** is made by occulting the telescope to evaluate the dark noise of the PMT.

3. **The third measurement** is performed twice without any occultation with the SRT in the background, once in the presence of spray and once in the absence.

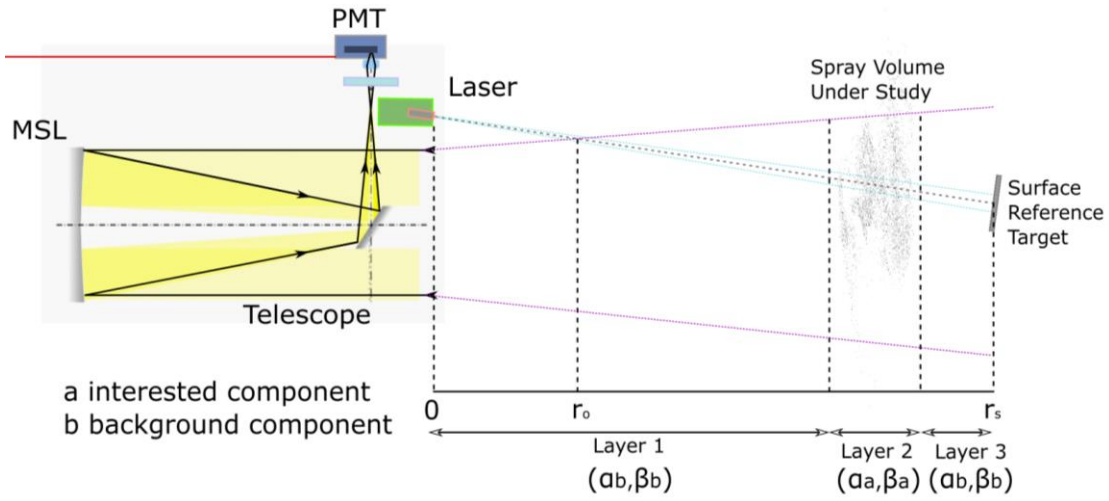

Fig. 46. Illustration of the MSL Spray measurement setup

With 1 kHz pulse repetition frequency, the spray could be sampled for every millisecond. Our data acquisition arrangement allowed us to acquire data for a total period of 1 sec = 1000 ms (1000 samples every measurement). The lidar signal was averaged for these 1000 samples, and then signals of the background radiation and the dark noise from the first and second measurement are deducted from the third measurement and presented in the graph (Fig.47.). The distances were calculated using the TOF method described in Section 4.1.4.

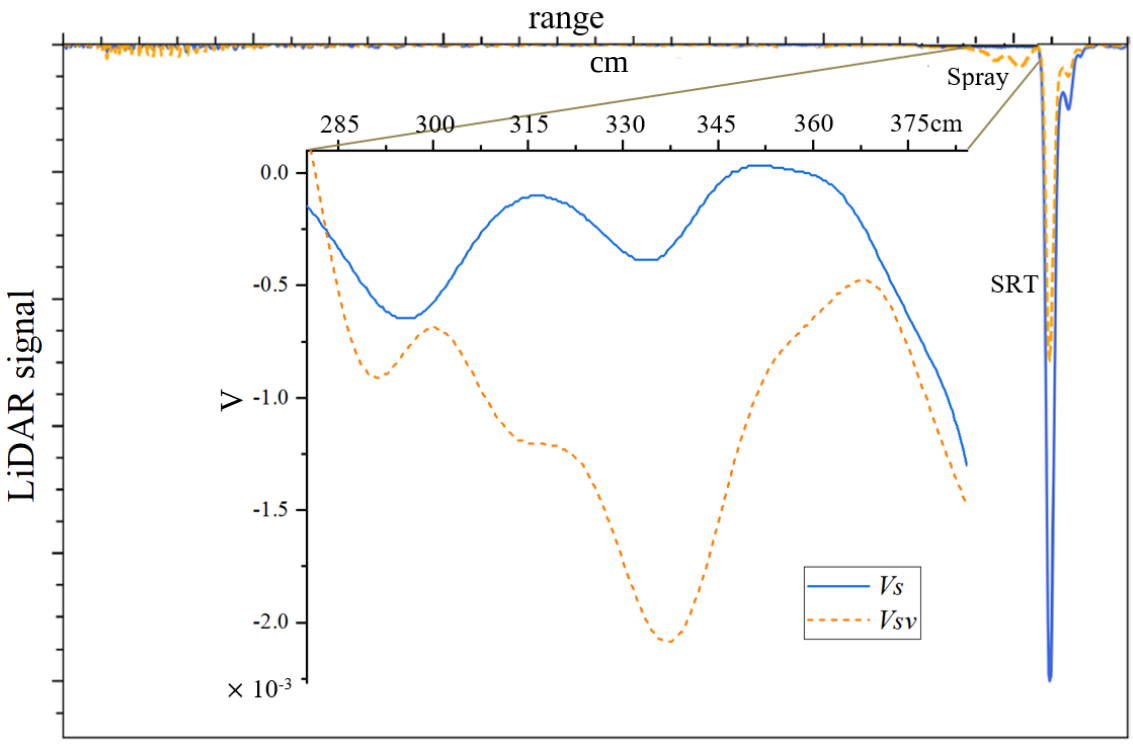

Fig. 47. MSL spray measurement curves. In blue, lidar signal in the absence of spray and orange the lidar signal in the presence of spray.

Analysis

The nozzle distance was evaluated at ~340 cm, spraying water in a conical volume, and the SRT was at ~370 cm. The graphs V_s and V_{sv} are the measurements in the absence and presence of spray with SRT in the background. The LiDAR signal value corresponding to the backscatter from the SRT is lower for V_{sv} than for V_s due to the presence of the spray. The spray backscatter signal begins to be visible nearby 285 cm and reaches a maximum of around 335 cm from the MSL. With a pulse width of the emitted laser (~3 – 4 ns), it is possible to highlight local variation concentrations in the order of 45 to 60cm inside the spray.

*The data of the zoomed part of the spray is only presented due to the limitation of our data acquisition system, which allows us to save data a maximum of 640 points per frame. Due to the data acquisition limitation, we couldn't record the spray and the SRT data simultaneously, barring us from the further calculation and applying the inversion technique for retrieving spray properties.

5 Conclusion

Marine icing is a very complicated phenomenon and involves many uncertainties; even with the present technological advancements and attempts by many researchers, we do not have all the answers. A substantial amount of study is present on sea spray ice accretion about modelling and numerical simulations with certain assumptions about the sea spray and not based on comprehensive real-time data. Also, the past techniques used to measure sea spray could not provide information about the impinging spray cloud, such as its complete droplets distribution, velocity, and concentration. For the modelling to be accurate, there is an acute need for experimental and real-time field data.

From the reviews of past studies carried out in the agricultural domain on pesticide spray drift, we identified LiDAR's temporal and spatial resolution capabilities to monitor the entire spray cloud's real-time behaviour. Moreover, the LiDAR system enables evaluation of the spray drift speed, its concentration, geometry, and evolution with time, which the past sea spray studies failed to provide. Due to its similar properties to sea spray, we proposed to use this remote measurement technique well-established in other disciplines in a field new to Lidars.

We developed a novel prototype LiDAR MSL to realize this potential of analyzing sea spray and carried out initial spray measurements in the lab. Though, further improvement and challenges required to be resolved prior to its field deployment. Nonetheless, the initial spray measurement result exhibits the potential of the MSL as a proof of concept for profiling spray with a high temporal and spatial resolution at a short range. With a better data acquisition system, the MSL can provide spray cloud time-resolved information, thus quantifying droplet concentration in a sea spray cloud and total incoming water flux over time.

Our research shows LiDAR has the potential to answer some essential questions in the marine icing phenomenon by providing an approach to analyze the sea spray flux from a comprehensive perspective. We propose using this technique to gather real-time sea spray data in different sea states and different vessel types, which can ultimately aid in developing more accurate correlations and improving or validating the present or developing more precise sea spray icing models.

6 Future Work

Due to the data acquisition limitation, we couldn't apply the inversion technique and analyze longer interval of data; this is the primary improvement required for continuing the project. Apart from a better data acquisition system (DAQ), some other modifications are required before field deployment of MSL, which we realized during our design phase:

1. A weather-proof design to protect the equipment from water damage.
2. A resistive heating box for the emitter to maintain the pulsed wavelength.
3. Replacing the PMT with current photodetectors such as APD, Si PIN photodiode, etc., will make the equipment much more compact and efficient by making shorter pulses hence better distance resolution.
4. A two-lens collimation lens for the laser will improve the beam quality.

Getting access to a better DAQ, we intend to apply the Gaudfrin et al. 2020 method for lidar inversion (Appendix). After which, we can retrieve spray properties such as distribution of the spray layer and its evolution with time, radiative properties (backscatter profiles), and microphysical properties (number concentration profiles). Subsequently, we can evaluate the relationship between the concentration profile and the liquid water content (LWC) to calculate the icing rate.

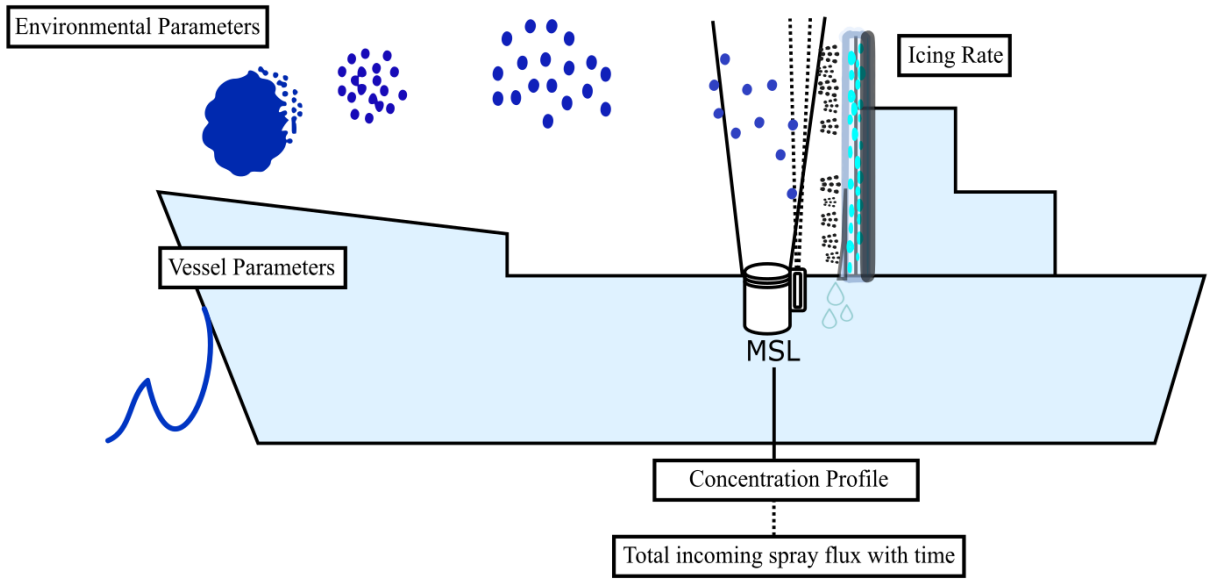

Fig 48. Parameters for LiDAR spray icing model

- Further improving the MSL with pan and tilt scanning arrangement with an IMU can enable surface 2-D or volume 3-D range-resolved imaging of the sea spray cloud. In contrast, past methods used to study sea spray only could display data from specific parts of a spray cloud.

- This technique is also suitable for carrying out observations to validate present theoretical and analytical models (e.g. CFD) of sea spray propagation.

- A shipborne LiDAR suited for analyzing incoming sea spray is possible to set up for carrying out autonomous measurements, thus can be deployed in multiple vessels, increasing the number of observations and data collection. Field measurements with the LiDAR system will allow us to produce more realistic data under several conditions for building a precise icing model.

In addition, short-range measurement can open the possibility to carry out other studies such as measurement of spray generated from wave impact in different parts of the ship other than bow like during beam winds and waves, the contribution of flux from ship's propeller wash, the variation of spray flux during synoptic-scale weather phenomena, the contribution of atmospheric icing and also can be utilized in the offshore and coastal facilities.

Works cited

1. Achtert, P., Brooks, I.M., Brooks, B.J., Moat, B.I., Prytherch, J., Persson, P.O.G., Tjernstr¨om, M., 2015. Measurement of wind profiles by motion-stabilised ship-borne Doppler lidar. Atmos. Meas. Tech. 8 (11), 4993–5007. https://doi.org/10.5194/amt- 8-4993-2015.
2. Adam, M., 2006. Development of lidar techniques to estimate atmospheric optical properties. Doctoral Dissertations, Johns Hopkins University. http://jhir.library.jhu.edu/handle/1774.2/851
3. Aksyutin, L.R., 1979. Icing of Ships (in _Russian). Sudostroeyne Publishing House, Leningrad, p. 126.
4. Allard, M., Cayer, F., Champagne, Y., Babin, F., Cantin, D., 2007. Novel applications of an affordable short-range digital lidar. In: Lidar Remote Sensing for Environmental Monitoring VIII. Presented at the Optical Engineering + Applications, 2007. International Society for Optics and Photonics, San Diego, California, US, p. 66810L. https://doi.org/10.1117/12.733883.
5. Ansmann, A., Mattis, I., Wandinger, U., Wagner, F., Reichardt, J., Deshler, T., 1997. Evolution of the Pinatubo aerosol: Raman Lidar observations of particle optical depth, effective radius, mass and surface area over Central Europe at 53.4◦N. J. Atmos. Sci. 54, 2630–2641. https://doi.org/10.1175/1520-0469(1997) 054<2630:EOTPAR>2.0.CO;2.
6. Barrett, E.W., Ben-Dov, O., 1967. Application of the Lidar to Air Pollution Measurements. J. Appl. Meteorol. 6, 500–515.https://doi.org/10.1175/15200450(1967)006<0500:AOTLTA>2.0.CO;2
7. Bøckmann, A., Shipilova, O., Ekeberg, O.-C., 2019. Model assumptions in rig icing and their implications. In: Proceedings of the International Conference on Port and Ocean Engineering under Arctic Conditions. Presented at the 25th International Conference on Port and Ocean Engineering under Arctic Conditions (POAC 2019), Delft, Netherlands.
8. Bodaghkhani, A., Dehghani, S.R., Muzychka, Y.S., Colbourne, B., 2016. Understanding spray cloud formation by wave impact on marine objects. Cold Reg. Sci. Technol. 129, 114–136.
9. Borisenkov, Y.P., Panov, V.V., 1972. Basic results and prospects of research on hydrometeorological conditions of shipboard icing. Issledovaniye fizicheskoy prirody obledeneniya sudov (Leningrad). Cold Region. Res. Eng. Lab. 1–30. Draft Translation TL411, 1974.
10. Borisenkov, Y.P., Zablockiy, G.A., Makshtas, A.P., Migulin, A.I., Panov, V.V., 1975. On the approximation of the spray cloud dimensions (in Russian). In: Arkticheskii I Antarkticheskii Nauchno-Issledovatelskii Institut. Gidrometeoizdat Leningrad, pp. 121–126.
11. Briese, C., Pfennigbauer, M., Ullrich, A., Doneus, M., 2013. Multi-wavelength airborne laser scanning for archaeological prospection. ISPRS - Int. Arch. Photogramm. Remote Sens. Spat. Inf. Sci. XL-5/W2, 119–124. https://doi.org/10.5194/isprsarchives-XL-5-W2-119-2013
12. Brown, R.D., Roebber, P., 1985. The ice accretion problem in Canadian waters related to offshore energy and transportation. In: Candian Climate Centre, Atmospheric Environment Service. Rep 85-13, p. 295.
13. Bufton, J.L., 1989. Laser altimetry measurements from aircraft and spacecraft. IEEE Proc. 77, 463–477.
14. Cammaert, G., 2013. Impact of marine icing on Arctic offshore operations. In: Arctic Marine Operations Challenges & Recommendations, vol. 5 (Pilot Project).
15. Cantin, D., Babin, F., Levesque, M., 2007. Real-time Measuring of the Spatial Distribution of Sprayed Aerosol Particles. United States Patent No. US20070076202A1. https://patents.google.com/patent/US20070076202A1/en.
16. Ceolato, R., Bedoya-Velásquez, A.E., Mouysset, V., 2020. Short-Range Elastic Backscatter Micro-Lidar for Quantitative Aerosol Profiling with High Range and Temporal Resolution. Remote Sens. 12, 3286. https://doi.org/10.3390/rs12203286
17. Chung, V.K.K., 1995. Ship Icing and Stability. Doctoral thesis. University of Alberta, Canada.
18. Collis, R.T.H., 1966. Lidar: A new atmospheric probe. Q. J. R. Meteorol. Soc. 92, 220–230. https://doi.org/10.1002/qj.49709239205
19. Collis, R.T.H., 1968. Lidar observations of atmospheric motion in forest valleys. Bull. Am. Meteorol. Soc. 49, 918–923. https://doi.org/10.1175/1520-0477-49.9.918.
20. Collis, R.T.H., Russell, P.B., 1976. Lidar measurement of particles and gases by elastic backscattering and differential absorption. In: Hinkley, E.D. (Ed.), Laser Monitoring of the Atmosphere, E. D. Hinkley. Springer, Berlin/Heidelberg, pp. 71–151. https:// doi.org/10.1007/3-540-07743-X_18.
21. Comiskey, A.L., Leslie, L.D., Wise, J.L., 1984. Superstructure Icing and Forecasting in Alaskan Waters. University of Alaska Arctic Environmental Information and Data Center, p. 30 (Unpublished).
22. Comeron, A., Sicard, M., Kumar, D., Rocadenbosch, F., 2011. Use of a field lens for improving the overlap function of a lidar system employing an optical fiber in the receiver assembly. Appl. Opt. 50, 5538–5544. https://doi.org/10.1364/AO.50.005538

23. Davis, E.J., Schweiger, G., 2002. Elastic Light Scattering, in: Davis, E.J., Schweiger, G. (Eds.), The Airborne Microparticle: Its Physics, Chemistry, Optics, and Transport Phenomena. Springer, Berlin, Heidelberg, pp. 143–219. https://doi.org/10.1007/978-3-642-56152-8_3
24. Dehghani, S.R., Muzychka, Y.S., Naterer, G.F., 2016a. Droplet trajectories of waveimpact sea spray on a marine vessel. Cold Reg. Sci. Technol. 127, 1–9. https://doi. org/10.1016/j.coldregions.2016.03.010.
25. Dehghani, S.R., Naterer, G.F., Muzychka, Y.S., 2016b. Droplet size and velocity distributions of wave-impact sea spray over a marine vessel. Cold Reg. Sci. Technol. 132, 60–67. https://doi.org/10.1016/j.coldregions.2016.09.013.
26. Dehghani-Sanij, A.R., Muzychka, Y.S., Naterer, G.F., 2015. Analysis of ice accretion on vertical surfaces of marine vessels and structures in arctic conditions. In: Proceedings of the ASME 2015 34th International Conference on Ocean, Offshoreand Arctic Engineering May 31–June 5, 2015 Newfoundland,Canada. ASME, OMAE2015-41306, p. 7. https://doi.org/10.1115/OMAE2015-41306.
27. Dehghani-Sanij, A.R., Dehghani, S.R., Naterer, G.F., Muzychka, Y.S., 2017a. Sea spray icing phenomena on marine vessels and offshore structures: review and formulation. Ocean Eng. 132, 25–39. https://doi.org/10.1016/j.oceaneng.2017.01.016.
28. Dehghani-Sanij, A.R., Dehghani, S.R., Naterer, G.F., Muzychka, Y.S., 2017b. Marine icing phenomena on vessels and offshore structures: prediction and analysis. Ocean Eng. 143, 1–23. https://doi.org/10.1016/j.oceaneng.2017.07.049.
29. DNVGL, 2019. DNVGL-OS-A201 Edition July 2019 Winterization for Cold Climate Operations. Rules and Standard. Copyright © DNV GL. Retrieved from. https://rules. dnvgl.com/docs/pdf/DNVGL/OS/2019-07/DNVGL-OS-A201.pdf.
30. Edner, H., Ragnarson, P., Wallinder, E., 1995. Industrial emission control using lidar techniques. Environ. Sci. Technol. 29, 330–337.
31. Ewing, G.C., 1965. Oceanography from Space: Proceedings. Woods Hole Oceanographic Institution. Fiocco, G., Smullin, L.D., 1963. Detection of scattering layers in the upper atmosphere (60–140 km) by optical radar. Nature 199, 1275–1276. https://doi.org/10.1038/1991275a0.
32. Fernald, F.G., 1984. Analysis of atmospheric lidar observations: some comments. Appl. Opt. 23, 652–653. https://doi.org/10.1364/AO.23.000652
33. Forest, T.W., Lozowski, E.P., Gagnon, R., 2005. Estimating marine icing on offshore structures using RIGICE04. In: Proceedings of the 11th International Workshop on Atmospheric Icing on Structures (IWAIS) 12-16 Jun 2005, Montreal, Quebec, Canada, pp. 45–52.
34. Fuentes, E., Coe, H., Green, D., de Leeuw, G., McFiggans, G., 2010. Laboratory-generated primary marine aerosol via bubble bursting and atomization. Atmos. Meas. Tech. 3, 141–162.
35. Fukuchi, T., Shiina, T., 2012. Industrial Applications of Laser Remote Sensing. Bentham Science Publishers, p. 194.
36. Fujii, T., Fukuchi, T., 2005. Laser Remote Sensing, Optical Science and Engineering 97. Taylor & Francis Ltd.
37. Gaudfrin, F., Pujol, O., Ceolato, R., Huss, G., Riviere, N., 2020. A new lidar inversion method using a surface reference target applied to the backscattering coefficient and lidar ratio retrievals of a fog-oil plume at short range. Atmospheric Meas. Tech. 13, 1921–1935. https://doi.org/10.5194/amt-13-1921-2020
38. Gregorio, E., Rosell-Polo, J.R., Sanz, R., Rocadenbosch, F., Solanelles, F., Garcer´a, C., Chueca, P., Arn´o, J., del Moral, I., Masip, J., Camp, F., Viana, R., Escol`a, A., Gr`acia, F., Planas, S., Molt´o, E., 2014. LIDAR as an alternative to passive collectors to measure pesticide spray drift. Atmos. Environ. 82, 83–93. https://doi.org/10.1016/j. atmosenv.2013.09.028.
39. Gregorio, E., Rocadenbosch, F., Sanz, R., Rosell-Polo, J.R., 2015. Eye-safe lidar system for pesticide spray drift measurement. Sensors 15, 3650–3670. https://doi.org/ 10.3390/s150203650.
40. Gregorio, E., Torrent, X., Planas de Martí, S., Solanelles, F., Sanz, R., Rocadenbosch, F., Masip, J., Ribes-Dasi, M., Rosell-Polo, J.R., 2016a. Measurement of spray drift with a specifically designed lidar system. Sensors 16, 499. https://doi.org/10.3390/ s16040499.
41. Gregorio, E., Torrent, X., Solanelles, F., Sanz, R., Rocadenbosch Burillo, F., Masip, J., Ribes Dasi, M., Planas, S., Rosell Polo, J.R., 2016b. Lidar: towards a new methodology for field measurement of spray drift. Asp. Biol. 201–206.
42. Gregorio L´opez, E., 2012. Lidar Remote Sensing of Pesticide Spray Drift. Ph.D. Thesis. Universitat de Lleida, Spain, p. 126.
43. Guest, P., Luke, R., 2005. Vessel icing. Mar. weather Log. 49, 9.
44. Hall, F.F., Ageno, H.Y., 1970. Absolute Calibration of a Laser System for Atmospheric Probing. Appl. Opt. 9, 1820–1824. https://doi.org/10.1364/AO.9.001820
45. Halldórsson, T., Langerholc, J., 1978. Geometrical form factors for the lidar function. Appl. Opt. 17, 240–244. https://doi.org/10.1364/AO.17.000240

46. Hamamatsu, 2003. Photomultiplier tube R5108 Datasheet. https://www.hamamatsu.com/resources/pdf/etd/R5108_TPMS1012E.pdf; accessed 16.05.2021
47. Hamamatsu, P.K.K., 2007. Photomultiplier tubes - Basics and Applications, 3rd Edition. https://www.hamamatsu.com/resources/pdf/etd/PMT_handbook_v3aE.pdf; accessed 16.05.2021
48. Hansen, E.S., 2012. Numerical Modelling of Marine Icing on Offshore Structures and Vessels. Master's thesis. NTNU - Norwegian University of Science and Technology.
49. Haner, D.A., McGuckin, B.T., Menzies, R.T., Bruegge, C.J., Duval, V., 1998. Directional–hemispherical reflectance for Spectralon by integration of its bidirectional reflectance. Appl. Opt. 37, 3996–3999. https://doi.org/10.1364/AO.37.003996
50. Yasser Hassebo (June 13th, 2012). Active Remote Sensing: Lidar SNR Improvements, Remote Sensing - Advanced Techniques and Platforms, Boris Escalante-Ramirez, IntechOpen, DOI: 10.5772/37139.
51. Hay, R.F.M., 1956. Meteorological aspects of the loss of Lorella and Roderigo. Mar. Observ. 26, 89–94.
52. Hey, J.D.V., 2015. A Novel Lidar Ceilometer: Design, Implementation and Characterisation, Springer Theses. Springer International Publishing. https://doi.org/10.1007/978-3-319-12613-5
53. Hiscox, A.L., Miller, D.R., Nappo, C.J., Ross, J., 2006. Dispersion of fine spray from aerial applications in stable Atmospheric conditions. Trans. ASABE St Joseph Mich. 49 (5), 1513–1520. https://doi.org/10.13031/2013.22043.
54. Hoff, R.M., Mickle, R.E., Froude, F.A., 1989. A rapid acquisition lidar system for aerial spray diagnostics. Trans. ASAE 32, 1523–1528. https://doi.org/10.13031/ 2013.31183.
55. Hofton, M.A., Minster, J.B. and Blair, J.B., "Decomposition of laser altimeter waveforms," in IEEE Transactions on Geoscience and Remote Sensing, vol. 38, no. 4, pp. 1989-1996, July 2000, doi: 10.1109/36.851780.
56. Horjen, I., 1990. Numerical Modeling of Time-dependent Marine Icing, Anti-icing and De-icing. Ph.D. Thesis. Trondheim Univ., Norway, p. 159.
57. Horjen, I., 2015. Offshore drilling rig ice accretion modeling including a surficial brine film. Cold Reg. Sci. Technol. 119, 84–110. https://doi.org/10.1016/j. coldregions.2015.07.006.
58. Horjen, I., Vefsnmo, S., 1984. Mobile Platform Stability (MOPS) Subproject 02 – Icing, vol. 283021. Norwegian Hydrodynamic Laboratories, River and Harbour Laboratory, p. 121.
59. Horjen, I., Loeset, S., Vefsnmo, S., 1986. ICING HAZARDS ON SUPPLY VESSELS AND STAND-BY BOATS (No. STF60 A 86073). Norwegian Hydrotechnical Laboratory, Norway, Trondheim.
60. Hulburt, E.O., 1937. Observations of a searchlight beam to an altitude of 28 kilometers. J. Opt. Soc. Am. 27, 377–382. https://doi.org/10.1364/JOSA.27.000377.
61. IMO, 2014. International Convention for Safety of Life at Sea, 2014 edition. International Maritime Organization, London.
62. IMO, 2016. International Code of Safety for Ships Operating in Polar Waters (Polar Code), 2016 edition. International Maritime Organization, London.
63. IMO, 2020. International Code on Intact Stability, 2020 edition. International Maritime Organization, London. 2008.
64. Itagaki, K., 1977. Icing on ships and stationary structures under marine conditions. A preliminary literature survey of Japanese sources. Special Report SR 77-27. US Army Cold Regions Research and Engineering Laboratory, Hanover, NH.
65. Itagaki, K. 1984. Icing rate on stationary structures under marine conditions. CRREL Report 84-12. Hanover, NH: US Army Cold Regions Research and Engineering Laboratory.
66. Johansen, J., Edvardsen, K., Sharma, P., Khawaja, H., 2015. Measuring the sea spray flux using high-speed camera. In: Poster Presentation at the the International Conference of Multiphysics, December 2015. London, United Kingdom. https://doi.org/10.13140/RG.2.2.34044.74884.
67. Jones, K.F., Andreas, E.L., 2013. Winter measurements of sea spray at Mt. Desert Rock. In: Proceedings of the 16th International Workshop on the Atmospheric Icing of Structures, St. John's Newfoundland, September 2013.
68. Jørgensen, T.S., Vefsnmo, S., Horjen, I., 1986. Offshore Icing – Phase II Final Report (No. STF60 F 86084). Norwegian Hydrotechnical Laboratory, Norway, Trondheim.
69. Kachurin, L., Gashin, L., Smirnov, I., 1974. Icing rate of small displacement fishing vessels under various hydrometeorological conditions. Meteorol. Gidrol. 3, 50–60.
70. Kato, R., 2012. Modelling of Ship Superstructure Icing. Master Thesis. Norwegian University of Science and Technology, Trondheim, Norway.
71. Khot, L., Miller, D., Hiscox, A., Salyani, M., Walker, T., Farooq, M., 2011. Extrapolation of droplet catch measurements in aerosol application treatments. At. Sprays 21, 149–158. https://doi.org/10.1615/AtomizSpr.2011002846.

72. Klett, J.D., 1985. Lidar inversion with variable backscatter/extinction ratios. Appl. Opt. 24, 1638–1643. https://doi.org/10.1364/AO.24.001638
73. Klett, J.D., 1981. Stable analytical inversion solution for processing lidar returns. Appl. Opt. 20, 211–220. https://doi.org/10.1364/AO.20.000211
74. Kong, Z., Liu, Z., Zhang, L., Guan, P., Li, L., Mei, L., 2018. Atmospheric pollution monitoring in urban area by employing a 450-nm lidar system. Sensors 18, 1880. https://doi.org/10.3390/s18061880.
75. Kovalev, V., Eichinger, W., 2004. Elastic Lidar: Theory, Practice, and Analysis Methods. John Wiley and Sons Inc, Hoboken.
76. Koyama, M., Shiina, T., 2011. Development of LED mini-lidar. In: 2011 International Quantum Electronics Conference (IQEC) and Conference on Lasers and Electro- Optics (CLEO) Pacific Rim Incorporating the Australasian Conference on Optics, Lasers and Spectroscopy and the Australian Conference on Optical Fibre Technology 28 Aug - 1 Sep,2011. IEEE, Sydney, NSW, Australia, pp. 544–545. https://doi.org/ 10.1109/IQEC-CLEO.2011.6193859.
77. Kulyakhtin, A., Tsarau, A., 2014. A time-dependent model of marine icing with application of computational fluid dynamics. Cold Reg. Sci. Technol. 104–105, 33–44. https://doi.org/10.1016/j.coldregions.2014.05.001.
78. Kumar, D., Rocadenbosch, F., 2013. Determination of the overlap factor and its enhancement for medium-size tropospheric lidar systems: a ray-tracing approach. J. Appl. Remote Sens. 7, 073591. https://doi.org/10.1117/1.JRS.7.073591
79. Kuzniecov, V.P., Kultashev, Y.N., Panov, V.V., Tiurin, A.P., Sharapov, A.V., 1971. Field investigations of ship icing in the Japan Sea in 1969. In: Theoretical and Experimental Investigations of the Conditions of the Icing. Gidrometeoizdat Leningrad, pp. 57–69.
80. Leosphere, 2009. Cloud & Aerosol Lidar for Atmospheric Monitoring (ALS 300/450 Product Information. Orsay, France).
81. Lenz, E., 1834. Ueber die Bestimmung der Richtung der durch elektrodynamische Vertheilung erregten galvanischen Ströme. Ann. Phys. 107, 483–494. https://doi.org/10.1002/andp.18341073103
82. Lolli, Simone, Sauvage, L., Loaec, S., Lardier, M., 2011. EZ LidarTM: a new compact autonomous eye-safe scanning aerosol Lidar for extinction measurements and PBL height detection. Validation of the performances against other instruments and intercomparison campaigns. ´Optica Pura Apl. 44, 33–41.
83. Lozowski, E.P., Szilder, K., Makkonen, L., 2000. Computer simulation of marine ice accretion. Philos. Trans. R. Soc. Math. Phys. Eng. Sci. 358, 2811–2845. https://doi. org/10.1098/rsta.2000.0687.
84. Lundquist, J.E., Udin, I., 1977. Ice accretion on ships with special emphasis on Baltic conditions, 23. Winter Navigation Research Board, p. 34.
85. Madonna, F., Amato, F., Vande Hey, J., Pappalardo, G., 2014. Ceilometer aerosol profiling vs. Raman lidar in the frame of INTERACT campaign of ACTRIS. Atmos. Meas. Tech. Disc. 7, 12407–12447. https://doi.org/10.5194/amtd-7-12407-2014.
86. Makkonen, L., 1984. Atmospheric Icing on Sea Structures. U.S. Army Cold Regions Researchand Engineering Laboratory: CRREL Monograph, 84-2.
87. Makkonen, L., 1987. Salinity and growth rate of ice formed by sea spray. Cold Reg. Sci. Technol. 14, 163–171. https://doi.org/10.1016/0165-232X(87)90032-2.
88. Makkonen, L., 2000. Models for the growth of rime, glaze, icicles and wet snow on structures. Philos. Trans. R. Soc. Math. Phys. Eng. Sci. 358, 2913–2939. https://doi. org/10.1098/rsta.2000.0690.
89. McManamon, P.F., 2019. Significant applications of LiDAR Ch-11. In: LiDAR Technologies and Systems. SPIE. https://doi.org/10.1117/3.2518254.ch11.
90. Measures, R., 1992. Laser Remote Sensing: Fundamentals and Applications. Krieger Publishing Company, Malabar, FL.
91. Mertins, H.O., 1968. Icing of fishing vessels due to spray. Mar. Obs. 38 (221), 128–130.
92. Mickle, R.E., 1994. Utilizing vortex behavior to minimize drift. J. Environ. Sci. Health., B 29, 621–645. https://doi.org/10.1080/03601239409372897.
93. Mickle, R.E., 1996. Influence of aircraft vortices on spray cloud behavior. J. Am. Mosq. Contr. Assoc. 12 (2), 372–379.
94. Mickle, R.E., 1999. Analysis of Lidar Studies Conducted during Aerial Spray Drift Trials. REMPSpC Report, Ayr, Ontario, Canada.
95. Mie, G., 1908. Beiträge zur Optik trüber Medien, speziell kolloidaler Metallösungen. Ann. Phys. https://doi.org/10.1002/andp.19083300302
96. Miller, D., Stoughton, T., 2000. Response of spray drift from aerial applications at forest edge to atmospheric stability. Agric. For. Meteorol. 100, 49–58. https://doi.org/10.1016/S0168-1923(99)00084-2.

97. Miller, D., Salyani, M., Hiscox, A., 2003. Remote measurement of spray drift from orchard sprayer using LIDAR. In: Proceedings of the 2003 ASAE Annual Meeting. American Society of Agricultural and Biological Engineers. Paper No. 031093.
98. Miller, D.R., Khot, L.R., Hiscox, A.L., Salyani, M., Walker, T.W., Farooq, M., 2012. Effect of atmospheric conditions on coverage of fogger applications in a desert surface boundary layer. Trans. ASABE (Am. Soc. Agric. Biol. Eng.) 55, 351–361. https://doi.org/10.13031/2013.41373.
99. Mintu, S., Molyneux, D., Oldford, D., 2016. State-of-the-art review of research on ice accretion measurements and modelling. In: Arctic Technology Conference. Offshore Technology Conference,24-26 October.St. John's, Newfoundland and Labrador, Canada.OTC. https://doi.org/10.4043/27422-MS.
100. Miya, H., Shiina, T., Kato, T., Noguchi, K., Fukuchi, T., Asahi, I., Sugimoto, S., Ninomiya, H., Shimamoto, Y., 2009. Compact Raman lidar for hydrogen gas leak detection. In: Conference on Lasers and Electro-Optics/Pacific Rim 30 August–3 September 2009. Optical Society of America, Shanghai China, p. ME1_3.
101. Muenkel, C., Emeis, S., Mueller, W.J., Schaefer, K.P., 2004. Aerosol concentration measurements with a lidar ceilometer: results of a one year measuring campaign. In: Remote Sensing of Clouds and the Atmosphere VIII. International Society for Optics and Photonics, pp. 486–496.
102. Muzik, I., Kirby, A., 1992. Spray overtopping rates for Tarsiut Island: model and field study results. Can. J. Civ. Eng. 19 https://doi.org/10.1139/l92-057.
103. NTSB, 2018. Capsizing and Sinking of Fishing Vessel Destination Due to Heavy Freezing Spray Conditions. National Transportation Safety Board. February 11, 2017 Accident Report, DCA17FM006. Retrieved rom. https://www.ntsb.gov/investigations/Accide ntReports/Reports/MAB1814.pdf.
104. Ong, P., Shiina, T., Manago, N., Kuze, H., Senshu, H., Otobe, N., Hashimoto, G., Kawabata, Y., 2018. A compact led lidar system fitted for a mars rover - design and ground experiment. EPJ Web Conf. 176, 02013, 2018.
105. Ono, N., 1964. Studies on the Ice Accumulation on Ships. 2. On the Conditions for the Formation of Ice and the Rate of Icing. Low Temperature Sci, pp. 171–181. A22 (in Japanese with English summary).
106. Orimolade, A.P., Gudmestad, O.T., Wold, L.E., 2017. Vessel stability in polar low situations. Ships Offshore Struct. 12, S82–S87. https://doi.org/10.1080/ 17445302.2016.1259954.
107. OSRAM, 2019. Metal Can® TO56, SPL UL90AT08 | OSRAM Opto Semiconductors. https://www.osram.com/ecat/Metal%20Can%C2%AE%20TO56%20SPL%20UL90AT08/com/en/class_pim_web_catalog_103489/prd_pim_device_2220021/; Accessed 16.05.2021
108. Overland, J.E., 1990. Prediction of vessel icing for near-freezing sea temperatures. Weather Forecast. 5, 62–77. https://doi.org/10.1175/1520-0434(1990)005<0062: POVIFN>2.0.CO;2.
109. Overland, J.E., Pease, C.H., Preisendorfer, R.W., Comiskey, A.L., 1986. Prediction of vessel icing. J. Clim. Appl. Meteorol. 25 (12), 1793–1806. https://doi.org/10.1175/ 1520-0450(1986)025<1793:POVI>2.0.CO;2.
110. Ozeki, T., Sagawa, G., 2013. Field observation of seawater spray droplets impinging on the upper deck of an icebreaker. In: Proceedings of the International Conference on Port and Ocean Engineering under Arctic Conditions. Port and Ocean Engineering under Arctic Conditions (POAC)2013-6-9 to 2013-6-13.Espoo, Finland, p. 7.
111. Ozeki, T., Shiga, T., Sawamura, J., Yashiro, Y., Adachi, S., Yamaguchi, H., 2016. Development of sea spray meters and an analysis of sea spray characteristics in large vessels. In: Presented at the the 26th International Ocean and Polar Engineering Conference. International Society of Offshore and Polar Engineers 26 June-2 July, Rhodes, Greece, p. 1335.
112. PAME, 2020. The Increase in Arctic Shipping 2013-2019. Arctic Ship Status Report (ASSR) Project, PAME - Arctic Shipping Status Report #1. The Protection of the Arctic Marine Environment. © 2020 PAME. Retrieved From. https://www.pame.is /document-library/shipping-documents/arctic-ship-traffic-data-documents/reports /arctic-shipping-status-reports-jpg-version/arctic-shipping-report-1-the-inc rease-in-arctic-shipping-2013-2019-jpgs.
113. Panov, V.V., 1976. Icing of Ships. Arkticheskii I Antarkti- Cheskii Nauchno- Issledovatelskii Institut. In: Trudy 334. Gidrometeoizdat, Leningrad, p. 263 (in Russian).
114. Paschotta, R., 2008. Field Guide to Laser Pulse Generation. SPIE.
115. Rashid, T., Khawaja, H.A., Edvardsen, K., 2016. Review of marine icing and anti-/deicing systems. J. Mar. Eng. Technol. 15 (2), 79–87. https://doi.org/10.1080/ 20464177.2016.1216734.
116. Rencz, A.N., Ryerson, R.A., 1999. Manual of Remote Sensing, Remote Sensing for the Earth Sciences. John Wiley & Sons, New York.
117. Richardson, B., Strand, T., Thistle, H.W., Hiscox, A., Kimberley, M.O., Schou, W.C., 2017. Influence of a young pinus radiata canopy on aerial spray drift. Trans. ASABE (Am. Soc. Agric. Biol. Eng.) 60 (6), 1851–1861. https://doi.org/10.13031/trans.12497.

118. Roebber, P., Mitten, P., Canadian Climate Centre., & Canada, 1987. Modelling and measurement of icing in Canadian waters. Report number: 87-15. Atmospheric Environment Service, Downsview, Ont. https://www.worldcat.org/title/modelling-and-measurement-of-icing-in-canadian-waters/oclc/456567088.
119. Ryerson, C.C., 1995. Superstructure spray and ice accretion on a large U.S. Coast Guard cutter. Atmospheric Res., Atmospheric icings of structures 36, 321–337. https://doi. org/10.1016/0169-8095(94)00045-F.
120. Ryerson, C.C., 2013. Icing Management for Coast Guard Assets. Cold Regions Research and Engineering Laboratory, US Army Engineer Research and Development Centre, Hanover (NH), p. 529. ERDC/CRREL TR-13-7.
121. Saha, D., Dehghani, S.R., Pope, K., Muzychka, Y., 2016. Temperature distribution during solidification of saline and freshwater droplets after striking a super-Cooled surface. In: Presented at the Arctic Technology Conference, 24-26 October, St. John's, Newfoundland and Labrador, Canada. https://doi.org/10.4043/27421-MS.
122. Samuelsen, E.M., Graversen, R.G., 2019. Weather situation during observed ship-icing events off the coast of Northern Norway and the Svalbard archipelago. Weather Clim. Extrem. 24, 100200. https://doi.org/10.1016/j.wace.2019.100200.
123. Samuelsen, E.M., Løset, S., Edvardsen, K., 2015. Marine icing observed on KV Nordkapp during a cold air outbreak with a developing polar low in the Barents Sea. In: Proceedings of the 23rd International Conference on Port and Ocean Engineering under Arctic Conditions; 2015 Jun 14–18; Trondheim, Norway.
124. Samuelsen, E.M., Edvardsen, K., Graversen, R.G., 2017. Modelled and observed sea-spray icing in Arctic–Norwegian waters. Cold Reg. Sci. Technol. 134, 54–81. https://doi. org/10.1016/j.coldregions.2016.11.002.
125. Sassen, K., 1975. Laser depolarisation 'bright band' from melting snowflakes. Nature 255, 316–318. https://doi.org/10.1038/255316a0.
126. Sawada, T., 1962. Icing on Ships and the Forecasting Method. (In Japanese). Snow and Ice, pp. 12–14, 24.
127. Sharapov, A.V., 1971. On the intensity of superstructure icing of small vessels (MFV type). Theoretical and experimental investigations of the conditions of ship icing. Gidrometeoizdat Leningr 95–97.
128. Shekhtman, A.N., 1968. The probability and intensity of the icing-up of ocean-going vessels. In: Moskow Nauk-Issled Inst. Aeroklim, T. Vyp 50, pp. 55–65.
129. Shellard, H.C., 1974. The Meteorological Aspects of Ice Accretion on Ships. Marine Science Affairs Report Technical Report 10. World Meteorological Organization, Geneva, Switzerland.
130. Shiina, T., 2010. Optical design for near range lidar. In: Proc. SPIE 7860, Lidar Remote Sensing for Environmental Monitoring XI, 78600B. Presented at the SPIE Asia-Pacific
131. Remote Sensing 11 Nov 2010, SPIE, Incheon, S. Korea. https://doi.org/10.1117/ 12.869568.
132. Shiina, T., 2013. LED mini-lidar for air and dust monitoring. In: Proc. SPIE 8905, International Symposium on Photoelectronic Detection and Imaging 19 Sep 2013. Laser Sensing and Imaging and Applications. SPIE, Beijing, China, p. 890533. https://doi.org/10.1117/12.2042370.
133. Shiina, T., 2019a. LED mini lidar for atmospheric application. Sensors 19, 569. https:// doi.org/10.3390/s19030569.
134. Shiina, T., 2019b. Sea wave dynamics visualization and its interaction with the surface atmosphere by LED mini-lidar. In: Presented at the Proc. SPIE 11150, Remote
135. Sensing of the Ocean, Sea Ice, Coastal Waters, and Large Water Regions 14th Oct 2019. SPIE, Strasbourg, France. https://doi.org/10.1117/12.2533406.
136. Shiina, Tatsuo, 2020. Atmosphere activity measurement by LED Raman mini lidar. EPJ Web Conf. 237, 07002 https://doi.org/10.1051/epjconf/202023707002.
137. Shiina, T., Koyama, M., 2010. M. LED Lidar System. Japanese Patent Application No. 2010-275798, 10 October 2010.
138. Shiina, T., Noguchi, K., Tsuji, K., 2015. Compact and mini Raman lidars for hydrogen gas detection. In: Presented at the Proceedings of the 23th International Conference on Nuclear Engineering (ICONE-23), Chiba, Japan, p. 3737.
139. Shiina, T., Yamada, S., Senshu, H., Otobe, N., Hashimoto, G., Kawabata, Y., 2016. LED minilidar for Mars rover. In: Proc. SPIE 10006, Lidar Technologies, Techniques, and Measurements for Atmospheric Remote Sensing XII, 100060F. Presented at the SPIE Remote Sensing 24 Oct 2016. SPIE, Edinburgh, United Kingdom. https://doi.org/ 10.1117/12.2241976.
140. Shipilova, O., Kulyakhtin, A., Tsarau, A., Libby, B., Moslet, P.O., Loset, S., 2012. Mechanism and dynamics of marine ice accretion on vessel archetypes. In: Offshore Technology Conference OTC-23762-MS; 3-5 December.Houston, TX, United States. https://doi.org/10.4043/23762-MS.

141. Song, X., Zhai, X., Liu, L., Wu, S., 2017. Lidar and ceilometer observations and comparisons of atmospheric cloud structure at Nagqu of Tibetan Plateau in 2014 summer. Atmosphere 8, 9. https://doi.org/10.3390/atmos8010009.
142. Song, Z., Zhang, B., Feng, H., Zhu, S., Hu, L., Brydegaard, M., Li, Y., Jansson, S., Malmqvist, E., Svanberg, K., Zhao, G., Bood, J., Svanberg, S., Li, D., 2020. Application of lidar remote sensing of insects in agricultural entomology on the Chinese scene. J. Appl. Entomol. 144, 161–169. https://doi.org/10.1111/jen.12714.
143. Spinhirne, J.D., 1993. Micro-pulse lidar. IEEE Trans. Geosci. Rem. Sens. 31, 48–55. https://doi.org/10.1109/36.210443.
144. Spinhirne, J.D., 1994. Micro pulse lidar systems and applications. In: Proceedings of 17th International Laser Radar Conference 25–29 July 1994.Chiba, Japan, pp. 162–165.
145. Stallabrass, J.R., 1980. Trawler Icing - A Compilation of Work Done at the National Research Council. Mechanical Engineering Report MD-56. National Research Council Canada, Ottawa, Ontario, Canada.
146. Steinbrecht, W., 1994. Lidar measurements of ozone, aerosol and temperature in the stratosphere (Doctor of Philosophy). York University, Ontario, Canada.
147. Stelmaszczyk, K., Dell'Aglio, M., Chudzyński, S., Stacewicz, T., Wöste, L., 2005. Analytical function for lidar geometrical compression form-factor calculations. Appl. Opt. 44, 1323–1331. https://doi.org/10.1364/AO.44.001323
148. Stoughton, T.E., Miller, D.R., Yang, X., Ducharme, K.M., 1997. A comparison of spray drift predictions to lidar data. Agric. For. Meteorol. 88, 15–26. https://doi.org/ 10.1016/S0168-1923(97)00056-7.
149. Sultana, K.R., Dehghani, S.R., Pope, K., Muzychka, Y.S., 2018. A review of numerical modelling techniques for marine icing applications. Cold Reg. Sci. Technol. 145, 40–51. https://doi.org/10.1016/j.coldregions.2017.08.007.
150. Swinehart, D.F., 1962. The Beer-Lambert Law. J. Chem. Educ. 39, 333. https://doi.org/10.1021/ed039p333 Texas Instrument, 2018. TIDA-01573 Nanosecond Laser Driver Reference Design for LiDAR.
151. Tabata, T., 1969. Studies on the ice accumulation on ships III. Low Temp. Sci. Ser. Phys. Sci. 27, 339–349.
152. Tabata, T., Iwata, S., Ono, N., 1963. Studies on the ice accumulation on ships I. Low Temp. Sci. Ser. A 21, 173–221.
153. Teigen, S.H., Ekeberg, O.-C., Myhre, B., Rustad, H., Petersen, S., Schrøder-Bråtane, E., Carlsen, S., 2019. Autonomous real-time sea spray measurement system for offshore structures. In: Proc. 25th Int. Conf. Port Ocean Eng. Arct. Cond. June 9-13 2019 Delft Neth., vol. 10.
154. Thorlabs, 2012. Thorlabs - FL905-25 Ø1" Laser Line Filter, CWL = 905 ± 5 nm, FWHM = 25 ± 5 nm. https://www.thorlabs.com/thorproduct.cfm?partnumber=FL905-25; accessed 21.05.2021
155. Tiana Alsina, J., Guti´errez Antu˜nano, M.´A., Würth, I., Puigdef`abregas Sagrist`a, J., Rocadenbosch Burillo, F., 2015. Motion compensation study for a floating Doppler wind lidar. In: Presented at the 2015 IEEE International Geoscience & Remote Sensing Symposium: Proceedings: July 26–31, 2015. Institute of Electrical and Electronics Engineers (IEEE), Milan, Italy, pp. 5379–5382. https://doi.org/10.1109/ IGARSS.2015.7327051.
156. Torrent, X., Gregorio, E., Rosell-Polo, J.R., Arn´o, J., Peris, M., van de Zande, J.C., Planas, S., 2020. Determination of spray drift and buffer zones in 3D crops using the ISO standard and new LiDAR methodologies. Sci. Total Environ. 714, 136666. https://doi.org/10.1016/j.scitotenv.2020.136666.
157. Tsai, M.Y., 2007. The Washington Spray Drift Studies: Understanding the Broader Mechanisms of Pesticide Spray Drift (PhD Thesis). Ph. D Thesis, University of Washington, Seattle, WA, USA.
158. Wandinger, U., 2005. Introduction to Lidar, in: Weitkamp, C. (Ed.), Lidar: Range-Resolved Optical Remote Sensing of the Atmosphere, Springer Series in Optical Sciences. Springer, New York, NY, pp. 1–18. https://doi.org/10.1007/0-387-25101-4_1
159. Wandinger, U., Ansmann, A., 2002. Experimental determination of the lidar overlap profile with Raman lidar. Appl. Opt. 41, 511–514. https://doi.org/10.1364/AO.41.000511
160. Weinman, J.A., 1988. Derivation of atmospheric extinction profiles and wind speed over the ocean from a satellite-borne lidar. Appl. Opt. 27, 3994–4001. https://doi.org/10.1364/AO.27.003994
161. Wise, J.L., Comiskey, A.L., 1980. Superstructure Icing in Alaskan Waters. US Department of Commerce, National Oceanic and Atmospheric Administration, Environmental Res. Laboratories.
162. WMO, 1994. Guide to the Applications of Marine Climatology. Secretariat of the World Metrological Organization, Geneva.
163. Wold, L.E., 2014. A Study of the Changes in Freeboard, Stability and Motion Response of Ships and Semi-submersible Platforms Due to Vessel Icing (Master Thesis). University of Stavanger, Norway.

164. Wolfe, W.L., Zissis, G.J., Michigan, E.R.I. of, 1978. The Infrared Handbook, 2nd edition. ed. Environmental Research Insti, United States.
165. Zakrzewski, W.P., 1986. Icing of Ships, Part 1, Splashing a Ship with Spray. Technical Report NOAA Technical Memorandum ERL PMEL 66. National Oceanic and Atmospheric Administration. Seattle, Washington, USA.
166. Zakrzewski, W.P., 1987. Splashing a ship with collision-generated spray. Cold Reg. Sci. Technol. 14, 65–83.
167. Zakrzewski, W.P., Lozowski, E.P., Muggeridge, D., 1988. Estimating the extent of the spraying zone on a sea-going ship. Ocean Eng. 15, 413–429. https://doi.org/ 10.1016/0029-8018(88)90008-X.

Appendix

LiDAR inversion technique utilizing surface reference target

Gaudfrin et al., (2020) proposed a method for lidar measurement inversion in circumstances where a volumetric layer of the high troposphere is not possible, appropriate for short-range measurements. It is based on a new expression of the lidar equation, enabling using a surface reference target (SRT) of a known bidirectional reflectance distribution function (BRDF) $f_{r,\lambda}$ (sr^{-1}) rather than a volumetric one. Also, a new algorithm is defined to ascertain the lidar ratio and the backscattering coefficient of an aerosol plume without a priori assumptions regarding the plume. Besides, the algorithm enables determining the instrumental constant. Also, a new algorithm is defined to ascertain the backscattering coefficient (β_a) and LiDAR ratio (LR_a) of an aerosol plume between the LiDAR and the surface target reference without prior assumptions regarding the medium to be characterized. Which was utilized for spray measurement using the MSL in our application.

Combined LiDAR equation for both surface and volumetric scattering media

From the single-scattering lidar Equation 8 (section 2.2.3), the measured backscattered power, at range r, by regarding both a surface target (Bufton, 1989; Hall and Ageno, 1970) and a volumetric target(Collis and Russell, 1976), was expressed as

$$P_\lambda(r, \theta_i) = P_{p,\lambda}\frac{c\,\tau_\lambda}{2}\frac{A_{ef}}{r^2}\left\{\beta_\lambda(r) + \frac{2}{c\,\tau_\lambda} f_{r,\lambda}(r_s, \theta i) F_{cor}\right\} T_\lambda^2(r)\,\xi_\lambda(r)\eta_\lambda \qquad \text{equation 1}$$

Where, $P_{p,\lambda}$ is the peak power of the emitted laser pulse(W), τ_λ is the pulse width(s), A_{ef} is effective telescope area(m^2), θ_i is the angle between incident laser beam and the normal eigenvector to the SRT. In our case of a Lambertian surface $f_{r,\lambda}(r_s, \theta i)$ can be expressed by spectral bidirectional reflectance factor ρ_λ from $\rho_\lambda \cos\theta_i/\pi$(Haner et al., 1998). r_s is the distance of the SRT, ξ_λ is the overlap function, and η_λ is the receiver efficiency.

In the volumetric lidar equation (Measures, 1992), P is considered a rectangular-shaped pulse, which is the ratio between pulse energy and τ_λ. The backscattered peak power is not proportional to $P_{p,\lambda}$ in the case of a SRT, hence the corrective factor F is introduced depending on the real shape of the pulse. The backscattered peak power is not proportional to $P_{p\lambda}$ in the case of a SRT, hence the corrective factor F_{cor} is included depending on the actual shape of the pulse. In our case the peak power is Gaussian shaped $P^G_{p\lambda}$ which is equal to square-shaped (P^s

p,λ) multiplied by $F_{cor,}$ and from conservation of pulse energy between the Gaussian and square pulses $F_{cor} = 2\ln(2/\pi)^{1/2}$ (Paschotta, 2008). T_λ^2 is the 2-way transmission through the atmosphere between the equipment and range r (Swinehart, 1962).

$$T_\lambda(r) = \exp\left[-\int_0^r \alpha_\lambda(x)dx\right] \quad \text{equation 2}$$

Where, α_λ(m^{-1})is the total extinction coefficient at wavelength λ and at a range r which is the sum of the contribution of the background ($\alpha_{b,\lambda}$) and to the contribution of the aerosol volumetric target($\alpha_{a,\lambda}$) under investigation expressed as $\alpha_\lambda = \alpha_{b,\lambda} + \alpha_{a,\lambda}$. Also, β ($m^{-1}sr^{-1}$) is the total backscattering coefficient expressed as $\beta = \beta_{b,\lambda} + \beta_{a,\lambda}$. The LiDAR ratios(LR) are expressed as $LR_{b,\lambda}(r) = \frac{\alpha_{b,\lambda}}{\beta_{b,\lambda}}$ and $LR_{a,\lambda}(r) = \alpha_{a,\lambda}/\beta_{a,\lambda}$.

The fundamental output measured by the MSL is in voltage (V) by the Oscilloscope, which is proportional to the backscattered power as follows: $V_\lambda(r) = R_{v,\lambda}P_\lambda(r)$. Where, $R_{v,\lambda}$ is the detection constant (VW^{-1}) deciding light to voltage conversion, expressed using the instrumental constant $C_{ins} = R_{v,\lambda}K_s$ (Vm^3), and $K_s = P_{p,\lambda}\, c\, \tau_\lambda A_{ef}\, \eta/2$.

The range-corrected LiDAR signal $V_\lambda(r)r^2$ (subscripts λ and θ_i ignored henceforth for better readability)

$$S(r) = C_{ins}(\beta_a(r) + \beta_b(r) + f_r \frac{2}{c\tau} Fcor \exp\left\{-2\int_0^r [\alpha_a(x) + \alpha_b(x)]dx\right\} \quad \text{equation 3}$$

Introducing LR to remove α dependency, the final lidar equation for surface and volumetric scatterers

$$S(r)LR_a(r)\exp\left\{-2\int_0^r \beta_b(x)[LR_a(x) - LR_b(x)]dx\right\} = C_{ins}\left[Y(r) + LR_a(r)\, f_r \frac{2}{c\tau} Fcor\right]\exp\left[-2\int_0^r Y(x)dx\right] \quad \text{equation4}$$

with $Y(r) = LR_a(r)[\beta_b(r) + \beta_a(r)]$

After that, it is useful to establish background-corrected transmission factor to emphasize the expression to solve:

$$D(0,r) = \exp\left\{-2\int_0^r \beta_b(x)[LR_a(x) - LR_b(x)]dx\right\}, \quad \text{equation5}$$

and $W(r) = S(r)LR_a(r)D(r)$

Ultimately, equation 4 becomes

$$W(r) = C_{ins}\left[Y(r) + LR_a(r) f_r \frac{2}{c\tau} Fcor\right] \exp\left[-2\int_0^r Y(x)dx\right] \quad \text{equation 6}$$

Inversion technique using surface reference target

Radiative parameters identification

The instrumental constant C_{ins} determined utilizing a SRT at a range r_s

$$C_{ins} = \frac{c\,\tau}{2 f_r\, Fcor} W(r_s) \frac{1}{LRa(r_s)} \exp\left[2\int_0^{r_s} Y(x)dx\right] \quad \text{equation 7}$$

The term $LR_a(r_s)$ is LiDAR ratio just before the SRT, $Y(r_s)=0$ at the SRT, and $f_r = 0$, for $r < r_s$.

$$W(r) = \frac{c\,\tau}{2 f_r\, Fcor} \frac{W(r_s)}{LRa(r_s)} \exp\left[2\int_r^{r_s} Y(x)dx\right] \quad \text{equation 8}$$

This applies only before the SRT.

$$\text{Also, } \exp\left[2\int_r^{r_s} Y(x)dx\right] = 1 + \frac{4 f_r\, Fcor\, LRa(r_s)}{c\,\tau\, W(r_s)} \int_r^{r_s} W(x)dx \quad \text{equation 9}$$

From equation 8 and equation 9 and using the definitions of $Y(r)$ and $W(r)$, $\beta_a(r)$ is finally expressed as

$$\beta_a(r) = S(r)D(r_s,r)\left[\frac{c\,\tau\, S(r_s)}{2 f_r Fcor} + 2\int_r^{r_s} S(x) LRa(x)dx\, D(r_s, x)dx\right]^{-1} - \beta_b(r) \quad \text{equation 10}$$

And from the LiDAR Ratio we can deduce $\alpha_a(r) = LR_a(r)\,\beta_a(r)$. The characteristics of the SRT are known from the manufacturer; the most significant parameter is LR_a. Providing a value for LR_a needs a priori understanding of the volumetric target under investigation, which can be a source of uncertainty leading to more or less severe errors in lidar measurements (Gaudfrin et al., 2020).